SLAC–PUB–4833
February 1989
(I/E)

THE MAC DETECTOR*

J. V. Allaby [a], W. W. Ash, H. R. Band, L. A. Baksay [b], H. T. Blume [c], M. Bosman [d], T. Camporesi [e], G. B. Chadwick, S. H. Clearwater [f], R. W. Coombes [g], M. C. Delfino [h], R. De Sangro, W. L. Faissler, E. Fernández [h], W. T. Ford, M. W. Gettner, G. P. Goderre [i], Y. Goldschmidt-Clermont [j], B. Gottschalk [k], D. E. Groom [g], B. K. Heltsley [l], R. B. Hurst [m], J. R. Johnson, H. S. Kaye [n], K. H. Lau, T. L. Lavine, H. Y. Lee [o], R. E. Leedy [g], S. P. Leung [p], I. Lippi [q], E. C. Loh, H. L. Lynch, A. Marini, S. Marcos [r], J. S. Marsh [s], T. Maruyama, R. L. Messner, O. A. Meyer [t], S. J. Michalowski [u], J. H. Moromisato, R. M. Morse, L. J. Moss, F. Muller [a], H. N. Nelson [e], I. Peruzzi [v], M. Piccolo, R. Prepost, J. Pyrlik, N. Qi [w], A. L. Read, Jr. [x], K. Rich [y], D. M. Ritson, F. Ronga, L. J. Rosenberg [z], W. D. Shambroom [aa], J. C. Sleeman [ab], J. G. Smith, J. P. Venuti [ac], P. G. Verdini [ad], E. von Goeler, H. B. Wald [ae], R. Weinstein, D. E. Wiser [af], and R. W. Zdarko

Department of Physics, University of Colorado, Boulder CO 80309
I. N. F. N., Laboratori Nazionali di Frascati, Frascati, Italy
Department of Physics, University of Houston, Houston TX 77004
Department of Physics, Northeastern University, Boston MA 02115
Stanford Linear Accelerator Center, Stanford University, Stanford CA 94309
Department of Physics, Stanford University, Stanford CA 94305
Department of Physics, University of Utah, Salt Lake City UT 84112
Department of Physics, University of Wisconsin, Madison WI 53706

Submitted to *Nuclear Instruments and Methods*

---

* This work was supported in part by the Department of Energy under contract numbers DE–AC02–86ER40253 (CU), DE–AC03–76SF00515 (SLAC), and DE–AC02–76ER00881 (UW); by the National Science Foundation under grant numbers NSF–PHY82–15133 (UH), NSF–PHY82–15413 and NSF–PHY82–15414 (NU), and NSF–PHY83–08135 (UU); by the Istituto Nazionale di Fisica Nucleare, and by the U.S./Japan Cooperative Program in High Energy Physics (agreement signed 12 November 1979).

Abstract

The MAC detector at PEP recorded data for an integrated luminosity of 335 pb^{-1} between 1980 and 1986. The design of this low-cost MAgnetic Calorimeter was optimized for electron and muon identification, as well as for the measurement of hadronic energy flow. Muon identification is available over 96% of the solid angle, and MAC was the first detector to make large-scale use of gas-sampling calorimetry. Electromagnetic calorimetry in the central section employs alternating layers of lead and proportional wire chambers (PWCs), and hadron and the remaining electromagnetic calorimetry is accomplished with iron plate and PWC layers. A relatively small central drift chamber in an axial magnetic field provides pattern recognition and modest momentum determination. An outer blanket of drift tubes completes the muon identification system. During the latter two years of operation an innovative "soda straw" vertex chamber made more precise lifetime measurements possible. With an evolving trigger system and highly automated data acquisition system, this modest detector has exceeded most of its designers' expectations and has produced a gratifying spectrum of physics results.

Contents

1. Introduction

The MAC (MAgnetic Calorimeter) detector was proposed as an innovative 4π "hermetic" calorimeter which would be built and commissioned on a very low budget by a relatively small collaboration. This was made possible by the first large-scale use of gas-sampling calorimetry. Commissioning with cosmic rays began before useful luminosity was first obtained in 1980 at PEP, the 29 GeV electron-positron collider at the Stanford Linear Accelerator Center (SLAC). Data were logged until operation ceased at the end of the PEP cycle in early 1986, for a total integrated luminosity of 335 pb^{-1}. The expectations of its builders have been more than fulfilled [1–30, 31–43]: MAC's chief strength is lepton identification, with good electron identification over central angles and excellent muon identification over about 96% of the total solid angle. Accordingly, electroweak interference in $\mu^+\mu^-$ production has been measured with half the statistical error obtained with other PEP and PETRA detectors [13], and comparable precision has been obtained for the asymmetry in $\tau^+\tau^-$ production [10]. The ratio of the hadronic to the QED $\mu^+\mu^-$ production cross sections has been measured to a precision of 2.8% [15]. Muon tagging of heavy quark flavors made possible a study of the b-quark fragmentation function [3], and the selection of muon and electron tagged events led to the first published lifetime of the B meson [5]. The τ lifetime was measured [1], and precision branching ratios for leptonic decays of the τ were obtained [14]. The addition of an innovative pressurized "soda-straw" vertex chamber in 1984 [24] led to more precise lifetime measurements [11, 22]. The search for supersymmetric particle production [7, 9, 17, 20] was improved by the addition of a small-angle veto system, parts of which were replaced by bismuth germanate arrays at the time the vertex chamber was installed. Measurements of two-photon $\mu^+\mu^-$ production [6], the strong coupling constant [15, 30], electroweak interference in hadron production [23], and other processes of current interest have also been published.

In this paper we describe the MAC detector [44]. After an overview we de-

scribe the calorimetry. The magnetic field configuration is then discussed, followed by discussions of tracking with its ancillary electronics. The combined use of these systems for muon detection is described. We then discuss the small-angle veto system, the trigger system, the data acquisition and analysis, and finally the luminosity monitor and the monitor system.

2. Overview of the detector

The MAC detector consists of a vertex chamber and cylindrical drift chamber inside a conventional solenoid coil, surrounded by an ensemble of finely-segmented total-absorption calorimeters, scintillation counters, and outer drift chambers. Components outside the inner tracking system and solenoid are arranged as a hexagonal prism with endcaps. The calorimetry provides complete coverage to within about 10° of the beams, and electromagnetic veto capability extends the coverage to within 5° of the beams. Figure 1 shows an isometric view of the detector with the outer muon system partially cut away. Transverse and longitudinal plan views are shown in Figs. 2(a) and (b), respectively.

The vertex chamber (VC) is of the "soda straw" design, with 324 aluminized mylar drift tubes, each 7 mm in diameter, arranged in three double layers. It occupies the space between the 3.8-cm outer radius of the beryllium beam pipe and the 9.7-cm inner radius of the central drift chamber. With an argon-CO_2 gas mixture at 4 atm, the average single-wire spatial resolution is 45 μm.

The 1.9 m long central drift chamber (CD) consists of 833 double sense wire cells arranged in 10 layers coaxial with the beams. The inner layer is 11.9 cm from the beam, and the outer layer at 45.5 cm. The wires in two-thirds of the layers are tilted 3° with respect to the beam axis to allow stereo measurement of the polar angle. The 180 μm point resolution of the CD results in typical angular resolutions of 0.2° in azimuth (ϕ) and 0.7° in polar angle, which in the 0.57 T axial magnetic field results in an inverse momentum resolution ($\sigma_{1/p}$) of about

$0.052 \sin\theta$ (GeV/c)$^{-1}$. Particles originating from the interaction point traverse at least nine layers of the CD for polar angles with $|\cos\theta| < 0.9$.

The electromagnetic and hadron calorimeters in the 2.4-m-long central section (CSC and CHC) are constructed of alternating layers of proportional wire chambers (PWCs) with 0.25-cm-thick lead-alloy plates and 2.5-cm-thick iron plates, respectively. In the endcaps only iron plates are used. The energy resolutions for electromagnetic showers are $\sigma_E/E = 20\%/\sqrt{E\,(\mathrm{GeV})}$ in the central section and $45\%/\sqrt{E\,(\mathrm{GeV})}$ in the endcaps, while for hadron showers the energy resolution is about $75\%/\sqrt{E\,(\mathrm{GeV})}$. The central section PWCs are strung with stainless steel wires parallel to the beams (the z axis), permitting the use of current division to measure the z position of tracks. The endcap PWCs are constructed of azimuthally segmented aluminum cathode strips and anode wire groups with segmentation in polar angle. Readout of both cathodes and anodes allows the measurement of both ϕ and θ for struck endcap calorimeter channels.

The outer drift system (OD) is used to identify muons and measure their momenta. For the central section it consists of large cylindrical drift tubes arranged outside the calorimeters in a hexagonal barrel four layers thick, except for the plane under the detector which, for geometrical reasons, consists of three layers of planar drift chambers. The ends of the detector are covered with six planes of drift tubes, covering the angular range $0.80 < |\cos\theta| < 0.97$. The iron calorimeters are magnetized with a toroidal field strength of 1.7 T. The OD measures the polar bend angle θ of a charged particle emerging from the iron. The average inverse momentum resolution is $\sigma_{1/p}/(1/p) = 0.36$, dominated by multiple scattering.

The fast trigger and time-of-flight (TOF) system covers 97% of the solid angle with 144 plastic scintillation counters read out by photomultiplier tubes. The 72 central section counters form a hexagonal barrel enclosing the CSC. Thirty-six counters are placed after the sixth iron plate of each endcap calorimeter (the region in which electromagnetic showers deposit most of their energy). With the

counters typically 2 to 4 meters from the interaction point, cosmic ray induced TOF hits on opposite sides of the detector have a time difference of about 10 ns, while hits produced by tracks from e^+e^- annihilation occur at roughly the same time. The TOF resolution is about 1 ns.

Triggers are formed using combinations of information from the scintillators, vertex and central drift chambers, and all calorimeters. Triggers initiate data acquisition by a VAX 780 [45], where an event must also satisfy a simple software filter to be accepted, usually at 4 to 6 Hz. A typical event occupies 1500 bytes, while a complicated hadron event might be about ten times larger. Runs consisting of about 10 000 events are recorded over roughly an hour, then transferred over a fast data link to the IBM 3081 [46] system at the SLAC computer center. A loose first-pass analysis rejects about 90% of the events, after which the raw data are archived onto magnetic tape. The filtered data are retained on disk for an extensive period to facilitate further analysis.

The acquisition and monitoring systems have become increasingly automated, and only one shift person is normally in attendance.

The display of an event as reconstructed by the software further illustrates the system. In Figs. 3(a) and (b) are shown side and end views of a 29 GeV $B\overline{B}$-candidate hadron event containing a muon. Figures 3(c) and (d) show hits and reconstructed tracks. The VC hits in Fig. 3(d) are shown as circles with radii obtained from the timing, so a track should be tangent to the hit circles. Finally, an enlargement of the vertex region is shown in Fig. 3(e).

The mass of the central section is 273 metric tons, and the mass of each endcap is 136 metric tons.

3. Calorimetry

The MAC calorimeters consist of metal plates interleaved with gas-filled proportional wire chambers (PWCs). There are three kinds. The electromagnetic calorimeter is made of lead-alloy plates and is assembled as a hexagonal prism just outside the solenoid magnet coil. The surrounding central hadron calorimeter is a welded iron structure of 2.5 cm plates into which PWC assemblies are inserted. The endcaps also consist of 2.5 cm iron plates, but with a different PWC design and readout. The endcap layers nearest the interaction point also act as small-angle electromagnetic calorimeters. A toroidal field in all of the calorimeter iron facilitates muon momentum analysis.

A common gas system controls the flow of a mixture of 85%/15% argon-methane at atmospheric pressure through the entire calorimeter system (23 m^3) and through the outer muon drift system (85 m^3). The recirculating gas system is discussed in sec. 3.6.

The sensitivity of the gain of the chambers (G) to temperature, pressure, high voltage, and gas composition (methane fraction) is as follows:

$$\Delta G/\Delta T \approx +2.4\%/1^\circ\ \mathrm{C}$$
$$\Delta G/\Delta P \approx -0.9\%/\mathrm{torr}$$
$$\Delta G/\Delta V \approx +1\%/\mathrm{volt}$$
$$\Delta G/\Delta(\mathrm{CH_4}) \approx +30\%/1\%\ .$$

These coefficients were measured with several prototypes, and are also routinely obtained from files of Bhabha events. The normal excursions of these variables are such that time-dependent corrections must be made as part of the data analysis.

Temperatures, pressures, and high voltages are recorded every eight minutes by the monitor system discussed in sec. 11. Electronic gains are measured at the beginning of every run. The gas composition is indirectly measured every two hours by the gas monitor system discussed in sec. 3.7. Maintenance procedures have been developed to deal with the few but inevitable broken wires.

3.1 Central electromagnetic calorimetry

The MAC central electromagnetic calorimeter consists of six independent trapezoidal prisms surrounding the solenoid coil, as shown in Figs. 1 and 2. A more detailed cross section of one of these sextants is shown in Fig. 4. The array provides electromagnetic calorimetry over the central polar angle range $45° \leq \theta \leq 135°$ and over the full azimuth. Each of the identical modules is a 13-radiation-length thick laminate of lead-alloy sheets and proportional tubes. The signal sum from the tubes is proportional to the number of track crossings of the shower, and hence to the energy. The location of the tubes measures the azimuthal angle ϕ, and charge division of the signal between the two ends of the tubes measures the polar angle θ. The dynamic range extends from the energy deposited by minimum-ionizing muons to that of 14.5 GeV electrons (the maximum available at PEP). Resolutions are $\Delta E/E \approx 20\%/\sqrt{E\ (\mathrm{GeV})}$, $\Delta\theta/\theta \approx 1.4°$, and $\Delta\phi/\phi \approx 0.7°$. Electromagnetic calorimetry is completed in the forward and backward regions by the endcap calorimeters discussed in sec. 3.3.

Each sextant has 32 flat layers of proportional chambers alternating with 2.54 mm thick typemetal plates (83% lead, 12% antimony, 5% tin; 1 radiation length = 6.56 mm). The 40 μm diameter stainless-steel anode wires run parallel to the beam line inside individual aluminum channels, which are open-topped to decrease the average critical energy and to simplify construction. An eight-cell extrusion forms the basic construction unit. Each extrusion, 218 cm long by 15.2 cm wide by 1.02 cm high, has inner cell dimensions of 18.0 mm wide by 8.64 mm high. Plastic bars with eight metal pins mounted at the ends of the extrusion provide support and electrical connection points for the wires. Two thin plastic bridges placed at equally spaced intervals along the chamber length keep the wires centered even if the extrusion bends under mechanical stresses. The number of cells per layer increases from 33 in the inner layer to 58 in the outer, for a total of 1450 wires per sextant. A thin aluminum skin encloses the entire sextant stack to form a single gas-tight volume. Further details, including

information about suppliers and costs, are given in Ref. 47.

The extrusions are grounded. High voltage is applied to the wires, and the signals are removed through decoupling transformers as discussed in sec. 3.5. A six-meter-long twisted pair connects each ganged group of wires to the decoupling transformer, which is located outside the magnetic field. During prototype development an attempt was made to float the entire extrusion/metal plate sandwich inside its aluminum container at negative high voltage. This introduced problems with cross-talk and insulation, and was dropped in favor of the present scheme.

The high voltage on this and the other calorimeters is lowered to 65% of its operating value during injection of beam into the storage ring to avoid large currents which could cause deterioration of the proportional chambers. This resting value was chosen to reduce chamber gain without fully removing the voltage and producing further electrostatic stresses. The chambers ran at 1710 volts for about 90% of the data taking, with shorter running periods at 1650 and 1750 volts during studies of noise, resolution, and gas composition.

Cooling coils attached to the aluminum skin nearest the solenoid coil intercepted the heat produced by this coil and helped maintain a stable temperature with a minimal gradient across the chambers. This system failed after three years due to corrosion, and the high voltage was decreased by 15 volts to help correct the gain for the higher operating temperature.

The individual cells are wired together into 32 azimuthal sectors per sextant, and each sector is wired into three longitudinal regions of 7, 13, and 12 layers each, thus providing azimuth and shower development information. This segmentation is shown in Fig. 5. In a typical inner radial group eight individual wire cells are ganged together, and in a typical outer radial group 20 cells are ganged. Because shower energy is shared between several nearby azimuthal groups, the azimuthal position resolution for an isolated shower is about one-third of the $\approx 2^\circ$ segmentation.

The signal size from each of the 32×3 groups per sextant is recorded for

each event. Sums over the groups in each sextant are also formed, primarily for use in the trigger. The noise on a sextant sum is about 10 kHz, consistent with that expected from radioactivity in the very large area of commercial typemetal sheets facing the proportional chamber gas. Its effect was reduced by requiring hardware coincidences between groups at the same azimuth but different radii.

After initial debugging, the number of malfunctioning wires was about 1%. Most of the problems were due to subtle misconnections or to intermittent shorts in the close-packed region underneath the gas cover. Continuing maintenance is limited to disconnecting the occasional broken wire, following the steps discussed in sec. 3.5. The impossibility of restringing the wire in a dead channel has not presented a problem because of the very low failure rate. Approximately 63 wires of the 8700-wire system have broken during six years of operation.

Charge division is used to obtain polar angle information. The decoupled signals from both ends of the wire groups are fed into preamplifiers having low input impedance. Since the stainless-steel wire has a high resistivity ($0.6\ \Omega\ \mathrm{mm}^{-1}$), the wire resistance is large compared with the preamplifier input impedance and the circuit acts as a resistive divider. Because of finite preamplifier input impedance, cable impedance mismatches, and other effects, the system must be calibrated. This was done with a large sample of Bhabha scattering events (e^+e^- final states) with the requirement that the shower positions measured by charge division agree with the position projected from the tracks measured in the central drift chamber. The attainable polar angle resolution is better for high-energy showers than for minimum ionizing muons because of the difference in signal size.

In order to optimize energy resolution, a time-dependent channel-by-channel calibration is necessary to account for:

(a) variations in gas gain,

(b) individual preamplifier and digitizing electronics gains,

(c) inherent gain variations in the calorimeter, due to geometry, mechanical supports, variations in wire diameters, etc., and

(d) signal loss due to component failure.

For example, the normal tolerance on methane concentration for commercial gas in this quantity is $\pm 0.2\%$; which introduces 5% variations in gas gain—about equal to the energy resolution for 14.5 GeV electrons. The variables which can affect chamber gain are all monitored and recorded as part of the data, as discussed in secs. 3.7 and 11. In addition, online programs filter out clean central-section Bhabha scattering events ($e^+e^- \rightarrow e^+e^-$) and sort them to provide energy distributions as a function of polar and azimuthal angles. These distributions are analyzed each time about 500 such events are accumulated, and provide a daily check of the performance and localized gain drifts due to changes in the gas, voltages, or electronics.

The result is a two-stage correction procedure. The first takes into account gas-gain variations, hit position along the wire, electronic gain variations, and any gain loss due to dead wires, as derived from the online monitoring. It is applied during the first offline event filtering in order not to lose events due to such variations, and is accurate within $\pm 1.5\%$. A final correction is derived from actual Bhabha events in each run. Further details about the procedure are given elsewhere [37].

Figure 6 shows an example of the uncorrected and corrected pulse height distributions for Bhabha electrons at $\sqrt{s} = 29$ GeV incident on the CSC away from dead channels and sextant boundaries. The resolution of the corrected pulse height is about $23\%/\sqrt{E\ (\mathrm{GeV})}$. This is consistent with the $17\%/\sqrt{E\ (\mathrm{GeV})}$ obtained in the test beam when extra material in front of the actual shower counter and differences in geometry are taken into account. Approximately one year of operation was required to develop the eventual calibration procedures and constants leading to the final resolution.

Two avoidable difficulties are both related to the use of open-topped extrusions: the noise assumed due to radioactivity, and the gain variations. The radiation is understood to be mainly low-energy alpha particles and could be

eliminated by a thin plating on the lead. It produces large signals at rates of 1 kHz to 10 kHz per sextant; an electronic coincidence between two out of the three wire groups in an azimuthal sector is required to reduce the trigger rate. The gain variations result from small gaps between the lead surface and the extrusions. While in principle these could be eliminated by tightly squeezing the stack, it was not possible in practice.

In spite of this, the central shower chamber has performed well with reasonable maintenance. It has been a good match to the overall requirements for an inexpensive and easily constructed detector and operation by a small collaboration. It has figured prominently in virtually all phases of the MAC physics program and was particularly important in the search for supersymmetric particles, in which sensitivity to low-energy photons was required.

3.2 Central hadron calorimetry

Each sextant of the central hadron calorimeter (CHC) is made up of 24 layers of 2.5-cm-thick iron plates followed by three layers of 10 cm iron plates, oriented parallel to the beam axis and interleaved with closed-cell extruded aluminum proportional tubes. The iron plates begin at a radial distance of 114 cm from the beam axis and end at 257 cm, with an overall length along the beam of 230 cm. The proportional tubes are parallel to the beam axis, have an inside cross-section of approximately 1.2×2.4 cm^2, and are strung with 40-μm-diameter stainless steel wire. As shown in Fig. 5, the wires are connected together in groups to form 192 equal segments in azimuth (as in the CSC), each divided in depth into three equal segments of eight layers each plus two individual layers (between the 10-cm-thick plates) to be used for muon identification. As in the CSC, the axial coordinate is measured using charge division between charge-sensitive amplifiers. These amplifiers have very low input impedance and are located at opposite ends of each segment in the first two groups of eight layers and the last individual layer. The charge division position measurement was calibrated with a large

sample of muon pair events by requiring agreement with the projection of the corresponding tracks measured in the central drift chamber.

3.3 Endcap calorimetry

An endcap consists of 28 iron layers, each 2.5 cm thick, followed by two 10-cm-thick plates, oriented perpendicular to the beam axis and interspersed with multiwire proportional chambers. In the closed position, the iron layers begin 128 cm along the beam axis from the interaction point and extend more than 2 m in the transverse dimension to cover the ends of the central section. As in the CHC, the last gap between thicker plates acts as a muon tagging layer. Each of the large hexagonal gaps in the iron structure contains 12 PWC sectors, each covering 30° in azimuth. Construction details of one of the 696 chambers are shown in Fig. 7. The 50-μm beryllium-copper wires are suspended across an acrylic frame at 1.9-cm intervals halfway between two parallel cathode planes 1.3 cm apart. Wedge-shaped aluminum cathode strips run in radial segments perpendicular to the wires. They are epoxied to insulating fiberglass sheets to form the chamber covers. Eight stiffening bars placed parallel to the wires keep the chamber rigid and have holes at alternating ends to encourage gas flow throughout the entire volume.

The anode wires are connected together in nine separate groups to provide radial segmentation, as shown in Fig. 5. Minor variations in structure with depth are indicated in the figure; these are to accommodate the geometry shown in Fig. 2 and to provide greater segmentation in the front parts of the endcap, which must double as an electromagnetic calorimeter. The cathode strips and anode groups are ganged in segments consisting of 3, 6, 11, and 8 layers in increasing depth from the interaction point, plus a single layer between the 10-cm-thick iron plates.

Neither of two operational problems with the endcap chambers is attributable to this design. The gas interconnections between chambers were not made tightly,

resulting in an annoying leak rate. The endcap chambers also experienced the highest wire breakage rate of any of the systems, about 0.1% per year. The breakage problem is thought to be due to a bad choice of wire for the construction. During summer maintenance periods those chambers which had lost two radial segments were replaced with chambers containing stainless steel rather than copper-beryllium wire. The new chambers have experienced no wire breakage.

3.4 Performance of the hadron calorimetry

Energy and position resolutions have been determined both from test beam and e^+e^- colliding beam measurements. Single-particle energy resolutions were determined from tests with momentum-analyzed pions and electrons with energies from 1 to 16 GeV[48]. The energy dependence of the measured hadron resolution is described well by $\sigma_E/E \approx 0.75/\sqrt{E}$, while for electrons $\sigma_E/E \approx 0.45/\sqrt{E}$. The electron energy resolution has also been verified with Bhabha scattering events in the endcaps. Angular resolutions are measured in the full detector by comparison of positions determined from calorimeter hits with those projected from tracks in the central drift chamber, for clean low-multiplicity events such as muon pairs. The polar angle resolution is found to be approximately $\sigma_\theta \approx 25$ mr, while in azimuth $\sigma_\phi \approx 17$ mr in the barrel and 35 mr in the endcaps.

The calorimeter energy calibration for hadrons was initially determined by combining several pieces of information: (a) test beam measurements with pions and electrons of known energy into electromagnetic and hadron calorimeter modules, operated both separately and together; (b) measurements with cosmic ray muons penetrating these same modules; (c) Bhabha scattering events at PEP, which give electrons and positrons of known energy into the central electromagnetic and endcap calorimeters; and (d) measurements with cosmic ray muons penetrating all parts of the calorimeter. Hadronic energy calibration constants were determined separately for the central electromagnetic, central hadron, and endcap calorimeters. After enough multihadron events had been collected, these

constants were checked and improved slightly by performing a minimization of the resolution of the combined calorimeter energy measured on a large sample of events selected for full containment (no energy deposition near the holes in the endcaps). Different calibration constants are required for events with electrons or pions in the final state, as the signal collected from an electron shower is substantially larger than that from a pion of the same energy. (The ratio measured in beam tests varied from 1.4 at 15 GeV up to 2.0 at 2 GeV).

The most important function of the calorimeter system is determining the magnitude and direction of energy flow in the "jets" of particles observed in multihadron final states. The result is approximate reconstruction of the parent quarks or gluons. This determination is limited not only by the single-particle resolutions described above, but also by the intrinsic fluctuations in the fragmentation processes. Such effects have been studied with the MAC detector simulation Monte Carlo program, described in sec. 9.3. Figure 8 shows histograms of the difference between parent quark directions and energy-flow thrust axes for Monte Carlo events having a thrust direction at least 60° from the beam axis and a thrust value of at least 0.8 (to minimize effects of the loss of detector acceptance near the beam). The solid histogram is for thrust directions calculated with the exact energies and directions of the final hadrons produced by the Monte Carlo event generator. The dashed histogram describes the same events, but with the thrust axes determined from the full MAC simulated calorimeter response. It is clear that the performance of MAC in this regard is not dramatically worse than a hypothetical "perfect" detector. Figure 9 shows the total calorimeter energy from MAC for a selection of real multihadron events, again requiring a large thrust value and a direction at least 60° from the beam axis. The FWHM corresponds to a gaussian with $\sigma = 0.85/\sqrt{E}$ at E = 29 GeV. The Monte Carlo simulation reproduces this result rather closely. The energy resolution is somewhat degraded from the single-hadron result quoted above, due to the fact that different jets contain different numbers of neutral pions. These decay to photons and deposit energy as purely electromagnetic showers, while the charged hadrons

deposit energy with a substantially lower average response per GeV.

The performance of the calorimeters in filtering and momentum-analyzing muons is discussed separately in sec. 6, since muon detection involves many subsystems of the detector.

3.5 Proportional wire chamber electronics

Figures 10(a) and (b) show the proportional chamber circuitry from anode wire to preamplifier for the central and endcap calorimeters, respectively. Figure 10(b) also pertains to the third layer of the CHC, since it has no charge division. There are minor differences between systems.

The cathode is grounded and the anode wire is connected to positive high voltage (HV) in all MAC chambers. For each of the three subsystems this HV is provided by three Bertan Model 1755P dual supplies [49]. Each supply is set to trip off and/or sound an alarm if the average current exceeds a preset limit (0.1 mA to 1.0 mA). Trips can occur from PEP beam loss causing excessive ionization on some wires. More frequently, a short-lived discharge between an anode wire and ground develops and causes a temporary surge of current. This kind of fast trip occurs several times per day, and is reset automatically.

Occasionally a proportional chamber wire breaks, shorting the anode to the cathode and removing high voltage from a large subsystem. Isolation or removal of the wire requires extended access to the detector. Since this may not be possible for weeks, the offending wire is progressively isolated. The details depend on which of the schemes shown in Fig. 10 is relevant.

In the CSC where there is no fuse in series with a wire group, a 10 MΩ series resistor limits current to about 0.2 mA. With the Bertan current limit set to 1 mA, voltage remains on the chamber when a wire breaks. In the first available access to the detector, the short is removed by breaking the connections to the shorted wire group in the box containing decoupling transformers (to be described

below). Finally, during a longer shutdown, the shower chamber is opened and the shorted individual channel removed.

In the remaining chambers there is a 5 mA or 10 mA fuse in series with each wire group. An entire endcap chamber (1/12 of a layer) is fused, while in the central section each wire group is fused. When a break occurs, the cable to the shorted section is removed from the HV fanout and temporarily connected to a high current "killer" HV supply, which blows the fuse after a few seconds. During a sufficiently long access, the problem is further isolated to a wire (in the CHC) or wire group (in an endcap chamber) and the fuse replaced.

The potential applied to each system is chosen so that the dynamic range of the readout system is a reasonably good match to the signal range encountered in a wire group. The extreme cases range from just a few minimum-ionizing track crossings for a muon passing through a given layer to as many as a thousand such crossings in the core of a high-energy electromagnetic shower. In the former case, the output signal must be significantly above the noise, and, in the latter, the output signal must not saturate the preamplifier. The voltages in the CSC, CHC, and EC accomplishing these ends are 1710 V, 1900 V, and 1950 V, respectively.

The signals from the anode wires of the EC and third layer of the CHC reach the preamplifier through 0.005 μF and 0.01 μF blocking capacitors, respectively. The EC cathodes are grounded through 10 kΩ, which not only acts as a load resistor, but also prevents the large area cathode strips from slowly charging over time. This would otherwise occur because the preamplifier input stage is transformer-coupled.

Coupling to the low input impedance preamplifier with transformers improves the accuracy of charge division in the CSC and CHC both by avoiding the need for blocking capacitors and by reducing the effective input impedance of the readout circuit. Capacitors provide the necessary AC path to ground. The 0.01 μF capacitance represents a compromise between a larger value that would have a lower impedance and a smaller one that would reduce the wire breakage

probability by minimizing the charge available for discharge. The connection between the transformer returns is essential for proper charge division, but for different reasons in the CSC and CHC. In the CSC this connection provides a path for the equalization of charge on the two capacitors that does not involve further current flow through the transformers. In the CHC, where a capacitor is present only at one end for wiring simplicity, the connection guarantees an AC ground for signals traveling to both ends. Space limitations in the CSC forced the removal of the transformers to the ends of 6-m-long, individually-shielded twisted pairs which have an effective impedance of 30 Ω. The 100 Ω back-terminating resistors in the CSC minimize excessive ringing over the long cable due to the impedance mismatch. The faces of the 2.54-cm-thick steel plates in the CHC provided a location for locally mounted transformers, rendering such terminating resistors unnecessary.

Two back-to-back diodes in parallel connect the two sides of each twisted pair signal cable on the preamplifier side of the transformer. They protect the preamplifier from unusually large pulses which could otherwise cause damage. Such pulses are occasionally produced by breakdown in the chamber. The protection diodes do not conduct in the presence of normal pulses.

The charge-sensitive preamplifier [50] has excellent linearity up to its full scale charge of 50 pC, which corresponds to 5 V across its 10-pF integrating capacitor. It also features a low nominal input impedance (28 Ω) and a low noise level ($<$ 25 fC). Transformer coupling at the input stage minimizes inductive pickup and ground return problems as well as assuring differential sensitivity. On each 32-channel board there are four summing amplifiers which send partial sums to the energy trigger. On-board calibration circuitry allows periodic monitoring of the actual gains and noise of individual channels, and the readings are used for offline corrections.

The outputs of each 32-channel preamplifier board travel 40 m over shielded twisted pair cables to a 32-input SHAM (Sample and Hold Multiplex) [51] unit

in a CAMAC [52] crate. Up to 20 single-width SHAMs occupy each crate and are controlled by a triple-width BADC (Brilliant Analog to Digital Converter) [53]. The entire SHAM-BADC calorimeter readout system of 3144 channels fills most of six CAMAC crates.

The preamplifier integrates the 50 ns rise time chamber pulse and produces a signal with a 2 μs decay. The trailing edge of an appropriately timed sample gate (triggered by a delayed PEP beam cross signal) signals the SHAM to hold the voltage level present at that instant. When a MAC hardware trigger fires, the sample gate is inhibited and a START pulse is sent to the BADC. The BADC then interrogates each 32-channel SHAM unit in its crate. The inhibit on the sample gate is released when the online computer finishes reading the event information from the BADCs and other data acquisition components. A 12-bit ADC digitizes the voltage levels held by each SHAM, with 5 volts corresponding to a full scale of 4095 counts. A built-in microprocessor subtracts pedestals measured at the start of the data run, and reports through CAMAC the addresses and pulse heights of only those channels with contents in excess of a pre-programmed threshold.

3.6 Proportional chamber and muon drift tube gas system

The proportional chambers for all of the calorimeters, as well as the muon drift tubes, are filled with gas consisting of 85% argon and 15% methane. Pre-mixed argon/methane is available commercially with the concentration of argon guaranteed to be 85% to within $\pm 0.2\%$. The basic idea was to use the commercial mixture in a closed-loop gas recirculation system, with in-line gas purification and automatic replacement of lost gas. The variations in gain due to small differences in the mixture obtained from the vendor are measured with an online gas gain monitoring system and corrected in the offline event records.

The gas recirculation rate is set by the requirement for an acceptably low level of contamination from air and outgassing compounds in the chambers. Different flow rates are required for the various subsystems, but are typically several

volumes per day. The system was designed for recirculation rather than venting because of the large gas volume of the chambers. The volumes are 3.4 m^3 in the CSC, 8.5 m^3 in the CHC, 11.4 m^3 in the EC, and 85 m^3 in the muon drift chamber system. The muon drift chamber system is not in the recirculation loop but receives fresh gas (about half of its volume per day) from the supply tube trailer with the exhaust gas going directly to the return manifold of the recirculation system.

An unacceptable buildup of contaminants would occur unless some provision were made for purification. Of these contaminants, only oxygen and water are important. The replacement rate (about 20% of the total flow) holds more innocuous contaminant concentrations at acceptable levels. Oxygen removal is accomplished by an in-line palladium catalytic converter [54]. In the presence of the catalyst, injected H_2 combines very efficiently with the approximately 150 ppm O_2 in the exhaust gas. The oxygen level is monitored with a Teledyne Model 315 Trace Oxygen Analyzer [55], capable of measuring O_2 levels from 10 ppm up to 250 000 ppm. Hydrogen is injected at a rate that ensures removal of O_2 to at least 10 ppm. (The hydrogen flow rate is occasionally adjusted manually to obtain a positive O_2 indication at about this level.) After oxygen removal, the gas flows through 45 kg of Linde 3A molecular sieve material [56], a synthetic crystalline anhydrous aluminum silicate which absorbs essentially all the water passing through it until the absorbed water totals about 25% of the dry weight.

The gas system is operated at close to atmospheric pressure with a small overpressure. The pressure is regulated by locating a gas ballast volume between the chamber exhaust and the recirculation pump. The ballast volume is in a servo loop which maintains a constant back pressure of 0.2 torr above atmospheric pressure. The actual overpressure at the chambers depends on flow rates and component impedances, but is typically about 2.0 torr.

Figure 11 shows a block diagram of the gas system. The recirculation pump maintains a constant flow of 10 m^3 hr^{-1} around the loop. Hydrogen flows into

the stream just before the palladium catalytic converter at a rate that keeps the oxygen level after the sieve to around 10 ppm. Approximately 2.2 m^3 hr^{-1} of makeup gas is required, primarily to compensate for leaks in the endcap system. In addition to the 150 ppm O_2, the unpurified return gas contains about 1500 ppm N_2. Nitrogen is not removed but only dilutes the mix at a harmless level. Under normal conditions the system operates automatically and has required only routine maintenance over six years of operation. Visual checks of flow rates and other quantities are made as part of a daily walk-through inspection of the experiment.

Different gas mixtures are used for the central drift chamber and the vertex chamber, as described in the respective sections. The gas volumes are sufficiently small that recirculation is not necessary.

3.7 *Gas gain monitor*

The gain of a proportional wire chamber is very sensitive to the gas composition and density. The gas gain is measured directly by the MAC gas gain monitor, providing the appropriate correction factors to remove the dependence of the calorimeter pulse heights on gas parameters.

The monitor is designed to simulate the characteristics of the real MAC calorimeters as closely as possible. It consists of six PWC channels, built from the same aluminum extrusions used in the central hadron calorimeter. Each PWC has a thin window over part of the wire, formed by drilling a small hole in the extrusion body and covering it with aluminized mylar. Mounted over each window is a 100-μC ^{55}Fe radioactive source, which provides a source of x-rays. These cause photoionization of the argon and the ejected electrons undergo energy loss in the gas, producing a signal approximately equivalent to two minimum-ionizing particles traversing the chamber. Gas to the six channels comes from the following sources:

2 channels: Standard reference gas (laboratory grade 85% argon, 15% CH_4, mixed to 0.1% accuracy);

1 channel: Main gas output of the gas recirculator;

3 channels: Gas outputs of the endcap, central shower and central hadron calorimeters.

Signals from the wire are decoupled through standard electronics, amplified, and then integrated with a time constant which is large (4.5 s) compared with the mean time between pulses. The output DC level is therefore proportional to the radioactive source rate times the gas gain. The former is removed by normalizing to one of the reference gas levels.

The accuracy of the system is dominated by the statistical fluctuations in the number of pulses integrated. The sources are adjusted annually to compensate partly for the decay of the sources ($\tau_{1/2} = 2.6$ yr), so that the statistical error is maintained at about 1%. Figure 12 shows the results of a week-long calibration run, where the standard gas was fed in as an unknown. The readings are distributed as a gaussian with mean $\sim$1.0 and width $\sim$1%, as expected from the above discussion.

4. Magnetic fields

The steel of the central and endcap calorimeters is magnetized by sets of six toroid coils, so that the momentum of muons penetrating the iron can be measured. A solenoid coil provides an axial magnetic field for the central tracking chambers, with several inner steel layers of the calorimeter serving as flux return.

4.1 *Toroidal fields*

Current in the coils circling each of the sextants drive a toroidal field of 1.7 T in the calorimeter iron. The arrangement of the coils can be seen in Figs. 1 and 2. Each coil has four turns of 2.44 cm square aluminum winding with a 0.76 cm hole extruded in its center for water cooling. A current of 2500 A flows through the windings in series, for a total of 60 000 ampere-turns.

A toroidal field is maintained in each endcap by means of current in six coils, as is indicated in Figs. 1 and 2. These coils are built and operated just as those in the central section.

The inner three layers of the central hadron calorimeter and the front five layers of the endcap calorimeter iron act as a flux return for the central solenoid. These layers have stainless steel inserts to prevent excitation of toroidal fields.

The magnitude of the toroidal magnetic flux density in the iron was determined to an accuracy of better than 5% by means of an induction measurement [57]. The magnet current was varied while an integrating digital voltmeter measured the voltage induced in several closed wire loops threaded through the steel in planes perpendicular to the toroidal field lines. This technique measures an average of the values of flux density present at all cylindrical radii enclosed by a measurement loop. The measured averages were analyzed to verify self-consistency and compatibility with magnetostatic theory, and to fit $B(\rho)$ for all cylindrical radii ρ in the toroid. The result of the fit is

$$B(\rho) = 1.715\ \rho^{-0.08285}\ ,$$

with B in tesla and ρ in meters, for $0.305\ \mathrm{m} < \rho < 2.572\ \mathrm{m}$.

Further improvement of the toroid field calibration was possible after a large amount of data had been collected. A sample of events was selected with pairs of muons having momenta between 2 and 10 GeV/c and reconstructed in both the central drift chamber and the outer muon system, as described in sec. 6.

An effective magnetic field was then calculated as a function of polar angle by requiring that the momentum measured by the outer muon system agree with that determined from the central drift chamber [58].

4.2 Solenoid

The solenoid coil is 229 cm long with an inner diameter of 99.5 cm. It consists of 16 separate helices in each of its two layers. Each helix consists of $5\frac{17}{32}$ turns, with opposite helicities in the inner and outer layers. The aluminum coil windings are 3.75 cm high and 2.45 cm wide and have an extruded 1.1 cm center hole for water cooling. Each layer thus forms a closely-wound coil with 16 separate circuits. In normal operation a current of 6000 A flows through the 32 circuits in series, alternating between inner and outer layers, making a total of 177 turns in 16 round trips up and back along the coil.* This total of 1.06×10^6 ampere-turns produces a nearly uniform axial field of 0.57 T. The voltage drop at 6000 A is 138 V, for a total power consumption of 828 kW. The total thickness of the windings and their fiberglass-epoxy insulation is 0.9 radiation lengths at normal incidence.

The axial magnetic field was mapped and calibrated *in situ* with a nuclear magnetic resonance probe. The magnetic field variations over the volume were sufficiently small so that a single constant value can be used for track reconstruction. The uncertainty in the magnetic field is dominated by the small variations in repositioning the detector iron endcaps after an access to the central section and the reproducibility of the solenoid current, and is less than 1%. This uncertainty is small compared to the uncertainty in the momentum as determined from the tracking reconstruction.

* The cooling water, however, flows in 32 separate parallel circuits, from one end of the inner windings and from the other end of the outer windings.

5. Tracking

Three separate drift systems provide precision tracking for the MAC detector. The innermost and most precise of these systems, the vertex chamber (VC) was added in 1984 to improve MAC measurements of the B and τ lifetimes. The central drift chamber (CD) provided the pattern recognition essential for most MAC analyses, as well as sufficient resolution for the earliest τ and B lifetime measurements. The outer muon drift system (OD) is used in combination with the magnetized iron calorimeters and central drift chamber to provide the muon momentum determination essential to the precision lepton pair asymmetry measurements and beauty tagging. The vertex and central drift chambers are coaxial with the beam, with longitudinal wires. The outer muon drift system wires are oriented normal to the beam direction and along planes defined by the hexagonal MAC geometry.

5.1 Central drift chamber

The central drift chamber is shown in Fig. 13. The 833 drift cells are arranged in ten cylindrical layers, inside a common gas volume filled with a 90% argon–10% methane gas mixture at atmospheric pressure. The original aluminum vacuum pipe (17.8 cm in diameter and 1.78 mm thick) together with the inner CD wall and its guard electrode with insulation presented a total of 0.036 radiation lengths to particles emerging at 90° from the collision point.* Stainless steel main endplates 1.9 cm thick support the 189-cm-long wires of layers 5–10. Stainless rings 1.0 cm thick are placed at smaller axial distances for the inner four layers, to permit adequate stereo angles without excessive radial distortion at smaller radii. The ten layers are located at equally spaced radii from the innermost at 11.9 cm to the outermost at 45.5 cm. Layers 2, 5, and 8 are skewed at +50 mrad to the beam line, and layers 3, 6, and 9 at −50 mrad to obtain the z position of the track crossing.

* After this pipe was replaced by the 3.68 cm outer radius beryllium pipe and the vertex chamber, the total was 0.038 radiation lengths.

The cell structure, electron drift paths, and isochrones are shown in Fig. 14. The cells in a layer are bounded by rows of five 200-μm-diameter cathode wires, maintained at -3.4 kV (-3.0 kV for the smaller cells of layers 1–3). A pair of field-shaping wires, also 200 μm in diameter and set at 1/3 of the cathode potential, help confine the electron drift paths to a compact region parallel to the cell's midplane. Each cell has two 20-μm-diameter sense wires at zero potential with a spacing of 375 μm, maintained against electrostatic repulsion by small epoxy beads at 15 cm intervals along their length. As Fig. 14 shows, each sense wire terminates the electron drift trajectories from its half of the cell, so that the sense of the drift distance is registered by the polarity of the pulse detected in the differential readout electronics connected to each wire pair. Thus the usual right/left ambiguity does not occur for this device. The Lorentz angle is modest in the 0.57 T magnetic field because of the relatively large electric field (≥ 1.5 kV cm^{-1}) and small drift velocity (25 μm ns^{-1}).

On average, each cell detects single charged particles crossing its volume with 96% efficiency. In the 0.57 T axial magnetic field produced by the solenoid coil surrounding the CD, the 180 μm point measurement error for each cell results in a momentum resolution of $\sigma_p/p = 0.052\,p\,(\mathrm{GeV/c})\sin\theta$ for θ between 23° and 157°, the angular range over which all ten layers are traversed by a charged particle originating near the interaction point. Somewhat worse resolution is obtained from 17° to 23° and from 157° to 163°, where only five to nine layers are traversed.

The inverse momentum distribution for nearly 17,000 dimuon events [13] is shown in Fig. 15. Gaussian fits to the $1/p$ distribution yield $\sigma = 64\%$ at 14.5 GeV, averaged over $\sin\theta$ for the sample. The charge assignment is improved for these events by the fitting constraint that both tracks come from a common vertex. In 11.6% of the events the total muon charge was ± 2, so the inferred one-track misassignment probability is about 6%. For beam-energy muons the additional information from the outer muon drift system provides unambiguous sign determination, while for lower-momentum particles sign assignment from the CD

alone is essentially unambiguous.

CD track reconstruction of a hadron event is shown in Figs. 3(a), (b), and (c). A staggered pattern of points in the stereo layers is evident for tracks that are out of the equatorial plane. Typically, a few extra hits appear in cells of the same layer near valid hits, because of electronic crosstalk in addition to δ-rays and other particle interactions.

During nearly continuous operation between 1980 and 1986 the CD has experienced six broken sense wires, all in the latter half of the period. All were successfully removed.

5.2 Vertex chamber

The original MAC design was constrained by the accelerator physics requirement that the beam vacuum pipe in the interaction region have 18 cm diameter. The central drift chamber was designed to have its first layer as close as possible to the beam. After some years' experience it was determined that both accelerator and background requirements would not be compromised by a much narrower beam pipe if suitable shielding were used, thereby creating space for a high-precision vertex chamber.

Since this chamber is the subject of a separate paper [24], the chamber design and operation are discussed only briefly here.

The technology chosen is a high-pressure drift chamber with cylindrical drift tubes. The chamber consists of three axial double layers of 7 mm diameter aluminized mylar "straws," with 30 μm gold plated tungsten wires along the axes. The 40 cm long tubes are held under tension between two aluminum endplates separated by a 0.5 mm beryllium spool piece, as shown in Fig. 16.

Electrical connections to the tubes are made in end sections which are part of the pressurized gas volume. A 2.5-mm-thick aluminum outer cylinder completes the gas volume, so that the ensemble can be evacuated or brought to its operating

pressure of four atmospheres. The chamber assembly was slid over the narrowed 0.76-mm-thick beryllium beam pipe which was then welded to tapering sections to mate with the existing sections of the PEP beam pipe.

Local tungsten and tantalum masking can also be seen in Fig. 16. collimators provide geometric shadowing from overfocused electrons and synchrotron radiation originating in the final focus quadrupoles. The tungsten and bismuth germanate (BGO) outside the vacuum absorb showers produced in the collimators.

The sense wires operate at high voltage. At one end they are terminated to ground through capacitors, and at the other they are connected to individual high voltage cables which run to the outside of the detector. Signals are there decoupled through capacitors. The avalanche pulses are amplified by LABEN 5254 amplifiers[59] and then processed by a two-level discriminator of in-house design. The lower level signal is gated by the higher, in order to avoid noise pulses while triggering at the single electron level.

A mixture containing equal parts argon and carbon dioxide plus 1% methane is used in the chambers. The methane is added to preserve the aluminum cathodes. In prototype tests[60] this mixture showed charge collection lifetimes in excess of 0.5 C cm^{-1}. The tubes are usually run at 3900 volts, just below the limited streamer regime, and have a gas gain of about 5×10^5. The drift velocity is proportional to the electric field, being ~ 7 μm ns^{-1} at the midpoint of the maximum drift distance, and shows an approximate time-to-distance relationship of $d \propto \sqrt{t}$. The precise dependence is determined by a more detailed parameterization, fitting to an ensemble of particle tracks and minimizing the apparent resolution. The steep dependence of distance upon time near the wire is undesirable, but since there was no experience for chamber operation so close to the beams at an e^+e^- collider, lifetime considerations dominated the choice of gas.

The spatial resolution of a single tube is dependent on the radius at which the ionizing particle makes its closest approach to the wire, as well as on other

complicated but well-known factors. After an extensive surveying procedure with electron pairs from Bhabha events established the wire positions in space, it was found that the resolution of a single wire could be represented by a constant value of 43 μm for drift distances in excess of 1.4 mm and rising linearly to 130 μm at the wire, for an average resolution of 50 μm. For particles over a few GeV/c momentum, the projected error at the event vertex is $\sim$80 μm for tracks reconstructed with few missing hits.

The figure of merit for lifetime measurements, however, is the error in the impact parameter at the origin. One measure of this quantity is provided by the "miss distance" for electron and positron tracks from Bhabha scattering events, as shown in Fig. 17. In the absence of a momentum constraint [Fig. 17(a)] the distribution is very close to gaussian with $\sigma = 124$ μm, so for a single electron the impact parameter uncertainty is $\sigma_V = 124/\sqrt{2}$ μm $= 88$ μm. Together with a momentum constraint, this results in a standard deviation at the vertex of $\sigma_V = 52$ μm [Fig. 17(b)]. For multihadron events the impact parameter resolution degrades to about 70 μm because of fewer useful hits and misassociation of hits in the dense environment.

The track-finding and reconstruction programs use separate procedures for the CD and VC hits, mainly for backward compatibility of the data. The tracks found are then matched and subjected to a final fit including hits in both sections. A graphic display of the hits and fitted tracks for a "typical event" is shown in Fig. 3(d) in which the isochronous circles derived from the individual straw timing information should be tangent to the fitted tracks. Hits not used in the fit are shown by the dotted circles. One interesting feature of the straw geometry is evident from the figure, for example in comparing tracks 6 and 7: the geometry in combination with the single-hit "earliest arrival" electronic logic results in far better near-track separation than the straw diameter would indicate, since the track nearest the straw center wins the hit. A further enlargement of the vertex region for this B-candidate event is shown in Fig. 3(e), where the $\sim$1 mm wide ellipse shows the rms profile for the beam spot.

5.3 *Outer muon drift system*

Particles which penetrate the calorimeters encounter an average of 6.5 nuclear interaction lengths of material, predominantly the iron in the central hadron calorimeter and the endcap calorimeters. With high probability, an isolated particle emerging from the detector is thus a muon. Extrapolation of a track segment measured outside the iron back to the interaction point or to a matching track in the CD determines the curvature of the muon in the toroidal field, and hence its momentum. Tracking on the outside of the detector is accomplished by the outer muon drift system, consisting of 3064 drift cells with a total area of about 1500 m^2 This system covers about 92% of the total solid angle, and is composed of three subsystems: the hex, bottom, and endplug systems. These can be seen in Figs. 1 (partially cut away) and 2.

The hex chambers cover five sides of the hexagonal cylinder defined by the central section and endcaps, and are the largest part of the system. Because the toroidal field bends particles in the θ direction, the tubes are oriented normal to the beam line and to radial directions. They are located at radial distances ranging from 280 cm to 390 cm from the beam line, and at -448 cm $< z <$ 448 cm from the interaction point. Each chamber is constructed from a cylindrical 10-cm-diameter aluminum tube whose 1.5-mm wall is grounded. An axial 50-μm-diameter gold-plated tungsten anode wire is maintained at high voltage. A total of 1720 tubes are equally divided into four layers 30 cm apart.

For structural reasons the bottom face of the detector could not be covered with chambers of this design. The "bottom system" is made up of planar chambers each containing ten 2.5-cm-thick $\times$ 10-cm-wide drift cells. The cells are separated by aluminum I-beams which are held at positive high voltage for field shaping. The tops and bottoms are closed by grounded aluminum cathodes which are 0.8 mm thick. Each cell contains a pair of 50 μm gold-plated tungsten sense wires, separated by 0.5 mm and at positive high voltage. Thirty-six such chambers are arranged in three layers separated by 35 cm, as can be seen in Fig. 2. As

in the case of the hex chambers, the sense wires are perpendicular to the beam direction.

The endplug chambers cover $7° < \theta < 33°$ on the north end and a symmetric range on the south end. Each is a 10 cm diameter cylindrical tube with the same construction as the hex system chambers. They are arranged in six hexagonal layers of 58 tubes each. The layers are perpendicular to the beam direction ($\hat{z}$) with 18 cm between layers. Their orientation is horizontal and $\pm 60°$ from horizontal in succeeding layers. Hits in a minimum of five layers are required for track reconstruction.

The hex and endplug chambers vary in length from 2 m to over 5 m. While not massive, the subassemblies containing them are very large and difficult to handle, particularly in the case of the endplug chambers. Moreover, it is necessary to remove hex chamber subassemblies for access to the endcap chambers and scintillators; a new position survey is necessary when the chambers are reinstalled. These problems are probably intrinsic to such large area coverage.

Because of its large area and lack of shielding, the OD system is sensitive to soft radiation from a variety of sources. Occupancy was nearly unity when it was first turned on. Almost all of the radiation (presumably soft x-rays) came from the nearby PEP radiofrequency accelerating cavities, and was eliminated by adding 5 cm of lead to the north and south PEP ring access doors in the experimental hall. The system remains very sensitive to background at the beginning of fills, but there is no serious occupancy problem during data acquisition.

An example of a reconstructed muon track is shown in Fig. 3(b). The muon is identified with track 2 in the other views.

The inverse momentum distribution in the OD system is shown in Fig. 18, based upon the same dimuon sample as was used for the central detector in Fig. 15. The smooth curve is the sum of two gaussians, centered at ± 0.07 $(\mathrm{GeV/c})^{-1}$ and with standard deviations of 0.025 $(\mathrm{GeV/c})^{-1}$, corresponding to 36% at 14.5 GeV/c. This resolution is consistent with the expected multiple scat-

tering in the iron, which corresponds to a ± 6 mm scatter when the particles leave the iron. (For this reason, tube placement and survey requirements were modest; wire positions were specified within 2 mm.) In general, we may summarize the OD inverse momentum resolution as

$$\sigma_{1/p}^2 = \left(\frac{0.25}{p}\right)^2 + \sigma_{\text{subs}}^2 ,$$

where p is measured in GeV/c and the constant subsystem contribution σ_{subs} ranges from 0.012 $(\text{GeV/c})^{-1}$ to 0.022 $(\text{GeV/c})^{-1}$ for the different subsystems. The first term arises from multiple scattering in the iron, and dominates over most of the range.

Substantial tails on the distributions are evident. These produce a single muon charge misassignment about 6% of the time for beam-energy muons. A study of δ-ray production yields a predicted charge misassignment of 4%, accounting for the tails. Since the CD and OD provide independent charge assignment information, the joint misassignment probability for a beam particle is 0.36%. For double misassignment (which is relevant for an asymmetry measurement) the probability is 0.002%.

A comparison between inverse momenta as fitted in the CD and OD (based upon muons from τ decay) is shown in Fig. 19. The slopes and miss distance at the origin for the two halves of the curve provide a measure of the correctness of the magnetic field calibration and muon energy loss in the iron.

5.4 Drift chamber electronics

The vertex chamber maximum drift time is 300 ns, while the OD drift times reach 3 μs. The central drift chamber and bottom OD chambers have two sense wires per cell. All systems use the same time digitization electronics. With the exception of the vertex chamber preamplifiers, the drift electronics are of in-house design and construction. A typical channel consists of a chamber-mounted

preamplifier driving a twisted-pair cable to a discriminator which is located close to the detector shielding wall. The discriminator output is sent to an analog time-to-voltage convertor (TVC) which is digitized by a 14-bit scanning ADC controlled via CAMAC. Unusual features of this system are the ability to combine left-right wire and time information from dual sense wire drift cells into a single electronics channel. Double hit capability is easily achieved by connecting a discriminator output in parallel to two TVC channels. A valid discriminator pulse into the first TVC channel enables the second TVC channel, which can record a second hit arriving at least 100 ns after the first. The use of common ramps and gates minimizes channel-to-channel variations and allows simple variation of running parameters.

Preamplifiers with differential input and output are mounted at the ends of each of the central and muon drift cells. One input is grounded in the case of a hex or endcap muon chamber, which has a single sense wire. The dual sense wires of the bottom muon and the central drift cells are connected to the dual-input preamplifiers, so that hits on one member of the pair produce positive output pulses and the other negative pulses. A discriminator produces standard output pulses with the same polarity as its input, thus preserving left-right information. Afterpulses are rejected because of a built-in 100 ns deadtime; this is important for multi-hit recording. A "look-through" diagnostic feature permits the discriminator to be disabled and the linear discriminator input signal to be fed out through the discriminator's output cables for observation in the counting house.

The TVC converts the arrival time of the discriminator output pulse to a voltage, which is held until it is digitized and recorded. A common voltage ramp initiated by a PEP timing reference signal is applied to two memory capacitors for each channel. Depending upon the polarity of the discriminator pulse, one or the other of the capacitors is "unlatched" from the ramp when the discriminator pulse arrives. The second capacitor unlatches at the common stop time. The difference in stored voltage on these capacitors is the channel output. For inputs

of opposite polarity the voltages on the memory capacitors are reversed. The result is an output voltage which ranges from 0 to 5 V for positive discriminator pulses and from 5 to 10 V for negative pulses. If no discriminator pulse is received both capacitors are unlatched at the common stop time, giving a pedestal value of 5 volts for that channel. Together with the polarity-preserving discriminator, these features retain the left-right information without additional subsystems or cabling. By cascading two TVC channels for each central drift wire a double-hit capability is achieved. TVC cards have 16 channels on a single-layer board and are implemented primarily with CMOS electronics. Low packing density and low power consumption have resulted in an extremely reliable system, with a failure rate of about five channels per year.

From 16 to 22 TVC cards and a scanner card are located in a single crate. The scanner sequentially connects each channel on each card to a common bus line. After the scanner has determined that switching transients on the line have died away, it tests the input voltage. If the input is close to five volts (no hit) the next channel is selected. Otherwise, the channel content is digitized by a fast 14-bit ADC. The channel number and content are then stored in the scanner memory. After the last channel has been processed, a standard voltage reference is digitized by the scanner for monitoring purposes, and the total word count for the crate is calculated. Skipping an unhit channel takes about 0.5 μs. Digitizing and storing information from a hit channel takes about 10 μs. All scanners examine the contents of their respective crates at the same time, minimizing the processing deadtime. All the struck channels within a crate are typically digitized in less than a millisecond. All scanners from a particular chamber are connected to a digital data bus which ends in a CAMAC interface module. A bus signal informs the module when the last scanner has finished digitization and the data are ready for transfer. A single variable length data block is later read into the VAX.

The electronics are calibrated with pulses generated by a crystal-controlled calibration circuit at any desired delay relative to the gate and ramp signals. The test pulse is delivered to each central drift preamplifier via a calibration

capacitor, while the high voltage cables are pulsed for the vertex and muon chamber channels. Altering the delay of the calibration pulse establishes both the start time and slope for the TVC output for each channel. Individual start times and a system-wide slope are sufficient to obtain the desired 1 ns resolution for the central drift and outer muon systems, but individual quadratic fits to the delay curves are necessary to achieve the required resolution of 500 ps for the vertex chamber channels. Dedicated calibration channels in each system are pulsed at fixed delays relative to the PEP beam crossing during data collection to monitor and correct for the short- and long-term jitter of the ramps and gates.

6. Muon detection

Muon identification and measurement over a large solid angle was one of the MAC design goals, and a large fraction of its major physics results have exploited this strength. It is based upon using the outer muon drift system (OD) in conjunction with most other parts of the detector.

To reach the OD, a particle must penetrate an average of 67 radiation lengths or 6.5 nuclear interaction lengths of material, mostly the iron of the calorimeters. A muon with sufficient energy to survive ionization losses (1.6 to 2 GeV) is almost certain to penetrate the detector. The probability that a photon or electron reaches the OD is vanishingly small, and the probability that an energetic hadron survives is about 0.15%. Satisfactory identification of muons in low-multiplicity events such as $e^+e^- \rightarrow \mu^+\mu^-$ or $\tau^- \rightarrow \mu^-\nu_\tau\overline{\nu}_\mu$ requires little more than the presence of a track in the muon drift chambers. In $e^+e^- \rightarrow q\overline{q}$ events, however, non-interacting hadrons and the hadronic cascade debris from late-interacting hadrons (collectively known as "punch-through") are an important source of background. There are an average of 2.4 hadrons per multihadron event with momentum greater than 1.8 GeV/c, or about 340 000 in our 144 000 event multihadron sample, so we expect about 500 non-interacting hadrons plus 5000 or 6000 late-developing cascades which spill over into the OD. In addition, muons are

produced by $\pi^{\pm}$ and $K^{\pm}$ decay in flight. While the small inner radius of MAC's calorimeters helps suppress the π and K decay muon flux, about 2000 muons from this source should reach the OD. In comparison with these backgrounds, the multihadron sample contains about 1400 muons from beauty decay and 2100 from charm decay which should reach the OD.

Assuming that a prompt muon (from heavy flavor decay or from an electroweak process) originates very near to the e^+e^- interaction point, a track in the OD defines a trajectory through the detector. A multihadron event containing such a muon is shown in Fig. 3. Activity in the detector along this trajectory is required which is consistent with the passage of a muon.

Selection criteria are obviously related to the process being studied. For precision work on the electroweak asymmetry in dimuon production [13], the problem is to achieve high and well-known efficiency in selecting simple events with beam-energy muons. A major background comes from cosmic rays passing through the fiducial volume around the interaction point; these are removed by time-of-flight measurements in the scintillator trigger system, as discussed in sec. 8.1. The collinear CD tracks are required to project to segments of the electromagnetic and hadron calorimeters which show minimum ionizing signals.

The detection efficiency for muon pairs in the analysis of Ref. 13 is shown in Fig. 20. It is calculated with the detector Monte Carlo simulation discussed in sec. 9.3, and includes efficiencies for the triggers, software filters, and the entire set of cuts used in the analysis. As can be seen, it exceeds 85% over 0.95 of the total solid angle. An additional correction for scintillator counter efficiency is not included, since its effect depends upon the way the scintillator requirement is imposed.

It is unnecessary to require OD tracks for the dimuon analysis because of the simplicity of the events. It is also undesirable, since some of the polar-angle dependent detection efficiencies would introduce systematic errors. In any case, OD tracks were reconstructed for 73% of the muons in the dimuon sample. There are

two major sources of inefficiency: the bottom OD chambers are only about 50% efficient, in part because of the awkward geometry, and reconstruction software has never been written for the polar-angle region in which a muon penetrates both the hex and endplug OD arrays.

The criteria used for selecting multihadron events with prompt muons were determined empirically by studying the signature of muons produced in $e^+e^- \rightarrow (e^+e^-)\mu^+\mu^-$ events and by scanning multihadron events. First, tracks in the hadron parts of the calorimeters are examined for likely matches to an OD track. The calorimeters are not tracking detectors, but they are of sufficiently fine segmentation that rough tracking is possible. These calorimeter tracks are constrained to pass through the e^+e^- interaction point, so tracks involving a single calorimeter segment are possible. Calorimeter tracks which contain hits in segments the muon would be expected to traverse, and at most one segment which it would be expected not to traverse, are considered further. Calorimeter tracks are required to match the OD track in polar angle θ within ± 0.2 radians. Linking OD tracks to calorimeter tracks determines the azimuthal angle ϕ for those parts of the muon system (hex and bottom chambers) which measure only the projection of tracks onto the mid-sextant plane and allows the calculation of total momentum. The azimuthal angle is measured, however, for muons going through the endplug outer muon drift chambers, and for such an event the azimuthal angles measured in the endcap and OD are required to agree within ± 0.4 radians; a weighted average ϕ is assigned to the track. Linked tracks in the muon chambers and calorimeters which pass these requirements are referred to as OD–CHC tracks in the following discussion.

Cascading hadrons typically produce multiple hits and tracks in both the calorimeters and muon chambers and deposit a large amount of energy in the calorimeters. In contrast, the minimum-ionizing passage of a muon is quite clean. OD–CHC tracks which have a large amount of activity which is characteristically hadronic are eliminated by a collection of "punch cuts" on calorimeter pulse heights and numbers of adjacent hits and tracks in the calorimeters and muon

chambers.

Next, a match is required between the OD–CHC (or OD–EC) track and a central drift chamber (CD) track. The OD–CHC and CD measurements of the momentum p and angles θ and ϕ are completely independent. The disagreement between the OD–CHC and CD measurements has been studied with $e^+e^- \to (e^+e^-)\mu^+\mu^-$ events and the widths of the difference distributions have been found to be

$$\sigma^2_{1/p} = \left(\frac{0.22}{p}\right)^2 + \left(0.034\,(\mathrm{GeV/c})^{-1}\right)^2 ,$$

$$\sigma^2_{\theta} = \left(\frac{0.065\,\mathrm{GeV/c}}{p}\right)^2 + (0.013)^2 ,$$

σ_ϕ = typically 0.014 radians in the central section and 0.060 radians in the endplugs, depending upon calorimeter segmentation,

where p is in GeV/c. For a match the two sets of measurements must agree with $\chi^2 < 25$, where the χ^2 is calculated with these σ's. The charge of the particle as determined by the OD and the CD is also checked for agreement. For data taken with the vertex chamber in place, the CD track is also required to have at least three associated vertex chamber hits. If these criteria are met, then the match between the OD–CHC and CD tracks is accepted. The assigned momentum is an average of the OD–CHC and CD measurements weighted by the resolutions of the respective systems. The momentum is signed to indicate the muon's charge.

Final cuts have varied with the goals of the analysis, and are somewhat different, e.g. for the B lifetime measurement [22] and for $B^0\overline{B^0}$ mixing studies [28]. Momentum cuts enrich the content of a given flavor (bottom in the case of all the MAC analyses) and suppress electroweak and τ decay contamination, and a $p_\perp$ cut with respect to a jet direction helps avoid heavily contaminated regions near the cores of jets.

Table 6–1 shows the number of identified muons in the data in each stage of

the identification procedure used in Ref. 28. A comparison with predictions from the detector Monte Carlo simulation is given in the last column.

As can be seen in Fig. 2, the detector presents fewer interaction lengths to particles produced near $\theta = 40°$ and $\theta = 140°$, where there are gaps between the material in the central section and endcaps. Most of this gap was an unavoidable part of the design, since it was necessary to leave space for wiring on the ends of the CSC and CHC proportional wire chambers, for light guides and photomultipliers for the central section trigger counters ("TOF" in Fig. 2), for solenoid magnet power and cooling, and for cable bundles from the central drift chamber and calorimeters. During assembly it was found that the cable bundles did not nest as neatly as planned, and a few additional centimeters were added to the gap, somewhat exacerbating punchthrough problems in the region. The main effect was an efficiency loss in this region when the punchthrough cuts were applied.

The system was designed to provide a great deal of redundancy for muon detection. In practice it worked well, but all of the redundancy was needed.

7. Small-angle veto system

Proportional wire chambers and scintillation counters were added to the detector after three years of operation to extend the angular coverage. The coverage of the new components was designed to overlap the main detector and is used primarily as a small-angle veto for electrons and photons. The system extends the angular coverage of the detector hermetically down to 3.8° from the beam line, with additional partial coverage to 2.5°. This modification was motivated by a search for final states containing stable weakly-interacting particles accompanied by a single radiative photon [9, 17]. Examples of such processes are pair production of stable photinos and neutrino pair production. The small angle veto system increases the sensitivity of the single photon search by reducing the $E_{\perp\gamma}$ range of single photons associated with QED background processes. The

QED processes tend to produce additional electrons and photons at small angles. Consequently, the proportional chambers and scintillators were positioned behind lead converters to increase the veto efficiency.

The vertex chamber which was added to the detector during the summer of 1984 partly occluded the small-angle scintillators and the small-angle proportional chambers below 6.8°. To recover the small-angle veto coverage, two annular detectors made from bismuth germanate ($Bi_4Ge_3O_{12}$, or BGO) crystals were installed surrounding the beam pipe in front of the shielding at each end of the vertex chamber. These annular detectors, each consisting of 24 identical crystals, cover the polar angular region from 4.8° to 7.2° and restore most of the coverage lost to the vertex detector system.

7.1 Small-angle veto calorimeter

The small-angle veto calorimeter (SAV) contains a 3.5-cm-thick lead plate and a 1.3-cm-thick lead plate, each followed by two thin PWC planes, tightly stacked in the 10 cm space at each end of the central detector between the CD and EC. The total thickness of the SAV is 8.5 radiation lengths. A side view is shown in Fig. 21, and the PWC construction details are shown in Fig. 22. Each PWC is constructed from a semiannular acrylic frame, with inner and outer radii 7.6 cm and 38 cm respectively, across which are stretched stainless-steel 50 μm diameter anode wires at 1.3 cm intervals, halfway between two parallel cathode planes held 1.0 cm apart by the frame. The cathodes are copper-clad G-10 sheets etched into three 60° azimuthal wedges on one side of the chamber and three equally spaced radial semiannuli on the other. The cathodes are glued to each side of the frame, making a sealed rigid planar PWC. Gas connections are made through holes in the frames. The frames have no internal structural ribs, which would introduce dead regions, so pressure drops are kept as low as possible by having each chamber receive its own gas flow in parallel with the other chambers. Each plane is composed of a pair of the semiannular PWCs joined to make a complete annulus with the inner 7.6 cm radius closing around

the beam pipe. Because each plane has a thin dead region where the edges of the two chambers in the plane touch each other, the planes are rotated with respect to one another to prevent alignment of the dead regions. The SAVs extend the angular coverage of the detector to within 5° of the beam axis for all azimuths.

The anode wires in each SAV PWC are joined together to provide one signal. This anode, the three 60° azimuthal cathode wedges, and the three radial cathode annuli (seven signals from each PWC) are read out separately. As a result, each SAV is segmented in depth into four layers, with two separate layers in each of the sampling gaps behind lead plates. Separately amplifying each cathode signal gives an effective azimuthal segmentation into 24 segments, each 15° wide, due to the overlap of 60° cathode wedges, and three radial segments.

The energy resolution of the small angle chambers is measured for beam energy electrons from Bhabha scattering events triggered on end-to-end coincidences. The pulse-height distributions for these 14.5 GeV electrons gave an energy resolution $\sigma_E/E = 18\%$, in good agreement with the expected resolution.

7.2 Small-angle taggers

In addition to the small-angle veto chambers, small-angle scintillation counters (SATs) covering approximately 85% of the azimuth between $2.5° < \theta < 6.2°$ were added. Constraints due to the beam pipe geometry required the use of two annular pieces of scintillator, each 2 cm thick, about the beam pipe, the first placed 1.6 m from the interaction point covering $3.5° < \theta < 6.2°$ and the second at 4.4 m, covering $2.3° < \theta < 3.8°$. Each annulus of scintillator is divided into quadrants, and at one end of each quadrant is placed a piece of waveshifter. The use of wave shifters permits the phototubes and bases to fit within the restrictive confines of the MAC endcaps. Because of space limitations, the 1.6 m SAT uses one phototube to view two quadrants, while the 4.4 m SAT uses one phototube to view each quadrant.

The primary purpose of the SATs is to increase the veto capability for photons or electrons associated with an event observed in the main detector. Consequently, the innermost SAT is placed behind an annulus of 4-cm-thick lead which serves to initiate an electromagnetic shower and increases the probability that photons or electrons associated with an event will be detected. Similarly, the outermost SAT is placed behind a 5-cm-thick lead annulus which also serves as a mask to prevent beam-related background from entering the main detector.

As seen from the interaction point, the SATs do not cover the complete azimuthal range. This is a result of the necessity to shape the scintillator to conform with other beam monitoring devices and with the beam pipe strongback.

7.3 Bismuth germanate arrays

As originally proposed, the vertex chamber design included a new beam pipe containing tantalum scrapers located about 75 cm from the interaction point. A tungsten cone outside the vacuum pipe on each side of the interaction point shielded the vertex chamber and central detector from secondary radiation from the scraper, but at the same time it severely compromised the small-angle electromagnetic veto necessary for the supersymmetric particle search. Consequently, it was decided to replace the forward sections of these cones with an "active" shield made of bismuth germanate ($Bi_4Ge_3O_{12}$, or BGO)[61].* Because of the extremely limited space and the substantial magnetic field, photodiode readout was essential. Recent work had shown this to be feasible[62, 63].

Each of the two arrays consists of 24 crystals with plane sides, approximating an annular cone extending from 4.8° to 7.2°. The front half of each crystal is cut so that the arrays conform to the 3.9 cm outer radius of the beam pipe. This geometry is illustrated in Fig. 16. The arrays are packaged as half-cones

* BGO is a clear, hard, chemically benign, nonhygroscopic crystalline material with a specific gravity of 7.13, a radiation length of 1.12 cm, and a hadronic interaction length of 23 cm. Its dominant fluorescence decay time constant at room temperature is 350 ns, and its light output has a temperature coefficient of $-1\%/°C$.

inside "cans" with 0.6 cm stainless steel endplates and inner and side walls made of 130 μm stainless steel foil, which are mounted on the 2-mm-thick beam pipe strongback. Crystals are 12 cm (10.7 radiation lengths) long, and the entire assembly is 15.2 cm long. Attached to the front (small end) of each crystal is a light-emitting diode (LED) for calibration purposes, and two photodiodes are mounted on the long trapezoidal far end. Each pair of crystals is covered by an electronics "mother board" on which two preamplifiers are mounted. This arrangement is illustrated in Fig. 23, which shows a photograph of a partially disassembled half-cone. Power and signal cables are dressed onto the outside of the tungsten shielding and exit the central part of the detector along the beam pipe.

Since the radial width of a BGO annulus is little more than a radiation length, energy resolution is limited by lateral shower leakage. The modest length was chosen for this reason, and the thick endplate on the can helps move the shower maximum forward. Since the system is designed to provide a veto signal in the event of a very energetic shower, the intrinsic resolution limitations were regarded as acceptable.

Over most of their length, the crystals are narrower in the azimuthal direction than in the polar angle direction, with the aspect ratio growing to nearly two at the large (photodiode) end. For a centered shower less than 25% of the energy is deposited in the struck crystal, with much of the balance being deposited in adjacent crystals. This feature ensures that even in the case of a lost channel the veto efficiency is not substantially reduced. Moreover, no inefficiency results when a shower is initiated in the beam pipe strongback, which cannot be occupied by BGO.

The crystals, which were of high quality, were obtained from NKK [64] on very short notice.

In a trapezoidal crystal with the light sensor at the large end, a larger fraction of the light produced at the more distant small end arrives nearly normal to the sensor than does light produced nearer the sensor. As a result, light from the

far end is detected more efficiently. One often "compensates" for this effect by selectively decreasing internal reflection in a crystal in order to obtain a more nearly uniform response. In our case the response was measured by illuminating a crystal with a pencil beam of radiation from a ^{137}Cs source while observing the crystal with a photomultiplier. The position of the 661 keV photopeak was monitored as a function of distance along the crystal to obtain the results shown in Fig. 24. The response increased by a factor of two as the source was moved from the photomultiplier to the far end in the case of a completely polished crystal. For an unpolished (sanded) crystal the effect was reversed. Several intermediate schemes were tried. In the one finally used, the long outer flat face of the crystal was sanded, resulting in the near-uniform response shown by the circles in the figure.

Development work in cooperation with Hamamatsu Photonics [65] had focused on the reduction of the noise intrinsic in a photodiode-preamplifier combination [63]. We obtained the first lot of diodes incorporating the new design, a special-geometry version (10 mm $\times$ 10 mm, with a 64 mm^2 active area) of what has now become available as the Hamamatsu S1723. Along with their desirable properties, these photodiodes exhibited runaway leakage current after being back-biased for an extended period. Given the short time scale for the project, there was little choice but to use them, taking extraordinary assembly precautions because of our ignorance as to the nature of the problem. Assembly was done in a dry room, and only baked photodiodes surviving a several-day trial period were installed. Dry nitrogen flows through the cans. The operating back-bias is 6 V, substantially less than the $\sim$20 V needed for complete depletion. Total current is monitored for each of the four cans, and has increased with time. The current is large enough to worsen the resolution, which is fortunately not critical for this application. The leakage problem has since been diagnosed and fixed by Hamamatsu [66].

LABEN 5254 preamplifiers are used [59]. These are essentially JFET versions of the bipolar input hybrid circuits used for the vertex chamber readout, which

are discussed in Ref. 24. Components are mounted on 18 mm × 25 mm cards, with pins for external connections. Provision is made for an external RC network to cancel the pole introduced by the first stage and replace it with another with a more appropriate time constant. Since this does not work (evidently because of a missing component), shaping is done elsewhere. Pairs of preamplifiers are mounted flat on 25 mm × 113 mm boards which distribute isolated power, signal connections, and photodiode bias potentials. The latter are connected through 100 MΩ resistors to provide isolation and limit excess leakage current. The electronics boards are mounted on the outer surface of the crystal arrays, inside the cans. Although energy dissipation is minimal, the (monitored) temperature is larger than desirable.

The differential preamplifier outputs are connected to external electronics by means of 20-m-long twisted pairs. These consist of calorimeter preamplifiers (described in sec. 3.5 and Ref. 50) which have been modified to handle the pulse shaping and gain requirements of the BGO system. The outputs are connected to SHAM inputs which were unused before the addition of the BGO, and the data are read out along with the calorimeter data.

Occasional calibration samples are obtained by modifying the MAC trigger to record Bhabha scattering events which result in large energy deposition in both BGO cones. Events with cascades relatively centered in polar angle are then selected by requiring a very large summed signal from the other side. A raw pulse-height distribution of the summed signal for these events is shown in Fig. 25(a).

To calculate individual gain correction factors, events are chosen with a large energy deposition on one side and nearly equal signals in the crystals adjacent to a given crystal on the other side, thus providing an event sample with "centered" showers in individual crystals. Individual gain correction factors typically differed from the average by about 12%, in rough accord with the variation expected to result from electronic component variations. Figure 25(b) shows the pulse-height distribution of the summed signal after gain variation correction, once again for

events tagged by a large energy deposition on the other side. As expected, the distribution falls rapidly on the high side (with an equivalent standard deviation of about 15%), while a long tail appears on the low-energy side due to side leakage in showers which are less centered.

All channels remained alive through the single-photon search reported in Ref. 17. One crystal has since been lost, probably through the failure of a preamplifier. In one case the gain factor is nearly twice the average, indicating that only one photodiode on the crystal may be functional.

Run-to-run monitoring is also possible by means of the LEDs attached to each crystal. These are configured so that alternate crystals are pulsed, providing a measure of crosstalk to adjacent channels as well.

In spite of problems which were encountered as a result of applying a new technology on a very short time scale, the BGO veto arrays have performed very well and have met all of their design goals. To the best of our knowledge, Ref. 17 represents the first use of a BGO array with photodiode readout in a high energy physics experiment.

8. Trigger System

The hierarchy of the MAC trigger logic is set by the 2.45 μs interval between PEP beam crossings. In the absence of any of several fast first-level triggers, all systems are reset after each beam crossing and are readied for the next. If a first-level trigger occurs, resets are inhibited for the next beam crossing, which is long enough for the formation of a slower second-level hardware trigger. This involves rough track recognition in the vertex and central drift detectors, as well as energy deposition information from the calorimeters. If a second-level trigger occurs, the event is read in by a DEC VAX 11/780 online computer, taking an additional 16 to 20 ms, depending upon the complexity of the event. A fast software filter then processes the event in about 11 ms, and if the event is found

acceptable it is written onto disk. The trigger has evolved with time, since useful features introduced into the software filter are often later incorporated into the second-level hardware trigger. When first installed, the software filter rejected about 70% of the events, but in later stages of MAC operation the rejection rate had decreased to about 10%.

The first-level trigger rate is several kHz at a typical PEP luminosity of 10^{31} $cm^{-2}s^{-1}$. Most of the first-level rate comes from the scintillation counter trigger system, which also provides a cosmic-ray trigger, functions as a time-of-flight system, and contributes to pattern recognition for several kinds of events.

Positive responses from the second-level trigger occur at about 4 Hz, or one in about 10^5 beam crossings, and produce a 10% dead time. This rate is the primary interrupt rate at the online computer, resulting in a data stream rate of about 6 kbyte s^{-1} to the online VAX.

8.1 Scintillator trigger system

An array of 144 plastic scintillators is embedded in the MAC calorimeters. Six counters per hexagonal face fit into each end of the third gap between the iron plates of the central section, sharing the gap with a PWC plane. The endcap arrangement is more awkward because of geometrical and structural constraints. Here counters are inserted horizontally into the fifth gap in the iron, with groups of nine counters of different lengths making up quadrants in each endcap. The arrangement is shown schematically in Fig. 26. The lateral extent of an endcap plane is chosen so that particles from the interaction point must cross either a central or endcap counter. The arrangement is very nearly hermetic, and covers 97% of the solid angle.

The 1.3-cm-thick NE114 scintillators [67] are viewed by Amperex XP2230 photomultipliers. Central section counters are 24.1 cm wide and 112.4 cm long. Their acrylic light guides bend outward through 90° and are flush with the ends of the central iron structure for about 60 cm, with the phototubes looking radially

inward at the ends. Here there is very little stray field from the solenoid magnet, and there is no significant leakage of the toroidal field from the iron. Endcap counters are 20.3 cm wide and have lengths varying from 107 to 189 cm, depending upon position. Short light guides match the counters to the photomultipliers. Slits cut into one of the iron layers provide space for the tubes. Field leakage does not affect the well-shielded tubes in spite of this arrangement. Two construction details worked well: the epoxy joint between the scintillator and light guide is stepped and is nearly unbreakable; and the edges of the wrapped counters are covered with a tightly fitting stainless steel foil, effectively preventing light leaks as a result of abrasion during handling.

Installation tolerances and the counter wrapping produced gaps of about 2 mm between counters. In addition, the steel structure at the corners of the central hexagonal prism created gaps of about 3 cm in six places. These combined to produce an unavoidable inefficiency of about 4%. In addition, studies of dimuon events with single-counter hits showed that the scintillator efficiency for minimum ionizing events drops by about 5% from the light guide to the far end of a central section counter [35].

Positive high voltage is applied to the phototubes by LeCroy 4032 power supplies [68], each of which provides 32 channels at programmed levels. As with the proportional chambers, these voltages are ramped down during PEP injection.

Each decoupled anode signal is passively split to drive an analog-to-digital convertor (ADC) and a discriminator. One discriminator output goes to a time-to-digital convertor (TDC), and is used to set a bit on the trigger bus. A second discriminator output is combined with other scintillation sections to form a logical OR. The trigger logic and trigger bus are described in detail in the following section on trigger electronics.

The use of scintillator timing for dimuon events is shown in Fig. 27. The sample consists of $e^+e^- \rightarrow \mu^+\mu^-$ candidate events which pass most selection cuts,

such as having two back-to-back tracks in the central detector. Scintillator times have been corrected for the position at which the muons strike the counters. In principle, the corrected arrival times for muons from the interaction point should be the same, while the cosmic-ray times should differ by the time-of-flight across the counter array. This time-of-flight is somewhat smeared because of the various possible geometric path lengths. As can be seen, the dimuon events cluster in a gaussian peak with a standard deviation of 1 ns, while cosmic rays distribute in a broad band which is well separated from the peak.

8.2 Trigger electronics

As outlined above, the MAC trigger consists of two hardware trigger levels with a third trigger level implemented in software on the VAX. Information used by the trigger includes rough track identification in both the vertex and central drift chambers, hits in the scintillation counters, and energy depositions in the shower, hadron, endcap, and veto calorimeters. This information is recorded as pulse heights in trigger sample-and-hold (TSH) channels and as logic bits on a trigger bus (TB) consisting of twenty 24-bit words. In addition to recording trigger information, the TB routes signals to hardwired AND/OR logic arrays which correlate signals from the desired detector elements to form trigger decisions. All of the information available to the trigger, most of the intermediate logic levels, and all of the final trigger decisions are logged with each event. Checks on the performance of each of the trigger components are made by offline programs, run periodically, which use this recorded information and the event data to reconstruct the possible trigger actions and compare them with the record of the hardware trigger decisions. In test modes, the information on the TB can be programmed from CAMAC to further aid debugging or testing of trigger components.

Track recognition in the vertex and drift chambers is based on flags set by each drift channel if a discriminator pulse is received within the time-to-voltage converter (TVC) gate. These flags are available on the TVC crate backplane as 1.5 mA current sources. A logical OR of drift cell combinations is formed by

connecting the desired lines to a summing amplifier. The voltage of this quasi-analog output is proportional to the number of drift cells struck. If the voltage exceeds a discriminator threshold (1–3 cells), a bit on the TB is set. For the vertex chamber, 18 wire groups are used corresponding to 3 superlayers divided into 60° azimuthal sextants. A logic bit corresponding to a vertex chamber track is made if all three superlayer groups within a specific sextant have one or more struck cells. The central drift wire groups are arranged into 18 overlapping azimuthal wedges of ~25° each for layers 1–5 and for layers 6–10. If three or more hits are found in a inner wedge group and not found in the corresponding outer wedge group, a bit for a small polar angle ($\theta < 20°$) track is set. A bit for a large-angle track is set if both inner and outer wedges have three or more cells struck.

The scintillation counters are located at a depth of 18 radiation lengths in the central calorimeter and at a depth of 8 radiation lengths in the endcaps. Scintillators should be struck by penetrating particles (muons and hadrons) at all polar angles within the scintillator acceptance and also by showering particles (photons and electrons) in the endcap region. The phototube output of each scintillator is sent to a discriminator which is gated on for ±20 ns about the beam crossing. The discriminator outputs form fast logic signals and also set a bit on the TB for each scintillator channel. Fast logical ORs are formed in the following geometrical groups: six sextants consisting of 12 counters in each central section sextant, and eight endcap quadrants each consisting of nine endcap counters. Signals are also generated if any south or north endcap or central section scintillation counter is struck.

Both pulse height and timing information from all of the MAC calorimeters are utilized in the trigger. Each of the calorimeter preamplifier cards sends one or more energy sums to the trigger electronics. Some of these sums are recorded immediately in a TSH channel. Other sums are used to form larger sextant sums which are also digitized in the TSH. In all cases, a TSH channel has an associated discriminator whose output bit is part of the trigger bus. The energy sums of interest are: 36 central shower chamber layer sums (6 per sextant); 18 central

and endcap shower chamber sextant sums; 18 central and endcap hadron chamber sextant sums; 4 sums from the veto calorimeter (2 per end); sums for each end of the BGO calorimeters; and 4 detector sums corresponding to the total energy in the central shower and hadron calorimeters, and in the north and south endcap calorimeters. Selected sum signals are sent to timing discriminators (TD) [69] in addition to the TSH channels. Each TD has a threshold separate from that of the corresponding TSH channel. The time of the TD output is related to the time of the calorimeter pulse. Thus a coincidence between a TD output and the beam crossing signal increases the probability that the calorimeter pulse is associated with a beam collision and not with a cosmic-ray event or with chamber noise.

The MAC trigger logic has evolved over the life of the experiment, and the trigger description given here applies to the last two years of data collection. The function of the lowest-level trigger is to generate a temporary system inhibit or pause which saves the event information for 2.4 μs, allowing the slower second-level triggers time to make a decision. Three types of first-level triggers are used:

1. A scintillator pause occurs if any scintillator is hit (typical rate, 800 Hz).
2. A gamma pause occurs if any of the central shower chamber sextants has an energy deposit of more than 1 GeV within 150 ns of the beam crossing (150 Hz).
3. A veto pause occurs if either of the two small angle veto chambers has energy deposit of greater than 2 GeV within 150 ns of the beam crossing (50+ Hz).

If no second-level trigger is formed, the system inhibit is released in time to generate gates and resets for the next beam crossing. The first-level triggers introduce less than a 0.5% system deadtime.

Second-level triggers demand correlations of signals from several detector elements, and if such a trigger is formed the event is read into the VAX. These triggers include:

1. Single photon trigger, consisting of a gamma pause with the further requirement that both the second and either of the first or third shower chamber layers of any half sextant have energy deposits greater than 0.25 GeV. The rate is dominated by radioactivity-induced noise pulses in the CSC and is typically 1.5 Hz.

2. Single muon trigger, a geometric coincidence of a vertex chamber track, a central drift track, a scintillator, and a hadron sextant in which more than 0.25 GeV is deposited (0.7 Hz).

3. Back-to-back endcap scintillator quadrants (1.5 Hz).

4. Back-to-back scintillator central section sextants with at least one central drift chamber track (0.2 Hz).

5. Energy trigger, with two or more of four detector energy sums (central shower, central hadron, and north and south endcaps) above 3 GeV; central hadron and north and south endcap sums must be accompanied by at least one scintillator hit in the corresponding region (0.2 Hz).

6. Test triggers, for example a veto pause with at least one CD track (0.4 Hz). This trigger specifically selects radiative Bhabha scattering events to study the single-photon trigger efficiency. Other test triggers select on Bhabha scattering into both BGO rings or into both veto calorimeters.

7. Random triggers. Beam crossings are selected at random to study backgrounds in the detector (usually set at 0.02 Hz).

The overall trigger rate is typically 3–4 Hz with a system deadtime of 8–10%.

8.3 Software trigger

The triggers described above interrupt the online computer. On the average each event contains about 1.5 kbyte of digital information read from the CAMAC system into the online VAX through a Jorway Model 411 CAMAC-to-UNIBUS interface[70]. The total interrupt rate times event length is about

6 kbyte s^{-1}. The VAX analyzes the incoming data in real time, using software filter requirements to select acceptable events. Due to differences in trigger thresholds, physics interests, and the selectivity of the hardware trigger, the software filter pass rate has varied from 30–90% over the course of the experiment. Typically, 2.6 kbyte s^{-1} are written onto magnetic disk.

The additional requirements made by the software filter include:

1. Events which meet the scintillator requirements (3) and (4) are required to have an azimuthal match between a CD wedge and an individual scintillator position.

2. Events which satisfy the requirements of the energy trigger [requirement (5)] are required to have a CD wedge pointing roughly to the region of energy deposition which caused the trigger, or to have deposited more energy (typically 10% more) than is required to exceed the hardware threshold.

3. Events which satisfy the requirements of the single muon trigger [requirement (2)] are required to be consistent with the full segmentation information available at this level.

9. Data acquisition and software

Data from the VAX online computer are sent to the SLAC IBM system by a disk-to-disk transfer. Once the transfer is complete, the raw data files are written onto high density (6250 bpi) magnetic tapes, which hold 140 Mbytes each, resulting in about one tape per day. At the same time, a batch job to run the MAC PASS1 filter program is queued into the IBM system. PASS1 rejects about 90% of the events (mostly cosmic rays, beam splash, and noise), yielding filtered data files. These filtered files are available, either directly from disk or from archive tape, to physicists for analysis. Members of the collaboration run their own filters to extract candidates for various final states of interest, such as

hadron events, lepton pairs, and two-photon events. A graphic representation of the data management system is shown in Fig. 28.

9.1 Data acquisition system

Data acquisition is controlled by a DEC VAX 780 computer with four Mbytes of memory running the VMS operating system [45]. The VAX communicates with the experiment using a Jorway 411 CAMAC interface [70]. Sixteen terminal ports are available and allow access to the computer even as data is being accumulated. Two 6250 BPI tape drives provide miscellaneous tape reading and writing capability. The system was originally configured with three DEC RP06 disk drives (~172 Mbytes per drive), which have since been replaced by two DEC RA81 drives (~454 Mbytes per drive). High speed monochrome graphics displays with 512 × 512 resolution are situated near each terminal in a counting house near the interaction area. Finally, a long line adapter (LLA)* provides a high speed link (~60 kbytes s^{-1}) between the MAC VAX and the IBM [46] 3081K at the SLAC computer center.

Using the Jorway 411, the VAX addresses two system crates, each equipped with a Jorway type A-2 crate controller. One of the system crates is used for the SLAC-built monitor system, since it generates CAMAC signals that interfere with the normal operation of some of the detector read-out electronics. From the main system crate, SLAC-built branch drivers fan out to five different parts of the experiment:

Branch 1 contains the central and outer drift systems, the muon tagging system, the luminosity monitor, and various hardware trigger logic information (trigger bus, and sample & hold systems);

Branch 2 is used for the scintillator system (ADCs, TDCs, latches, and HV controller);

* The LLA is a high speed serial communication device, formerly manufactured by System Associates, Inc.

Branch 3 is used for the proportional chamber (BADC) system;

Branch 4 is an isolated branch for debugging electronics, and is not normally read;

Branch 5 is devoted to the vertex chamber.

The general software philosophy is to use a modular design that establishes individual jobs or "processes" to handle the different phases of the data acquisition. These processes must still communicate among themselves, but this is done through very controlled and well defined mechanisms. VMS is equipped with a powerful set of tools for implementing and debugging such an architecture.

The CONTROL process is responsible for responding to an interrupt from the detector and controlling CAMAC. Because of its need for reliability and good response while other activities are taking place on the system, CONTROL has been kept relatively simple and small, and runs at elevated priority with crucial buffers locked into real memory to prevent swapping. When the electronics detects an event which satisfies the trigger conditions, a 1 ms prompt inhibit is set to prevent clearing of the data. The trigger system also asserts a long-term inhibit which can be cleared only by the VAX. The interrupt signal indicating the presence of the event passes through a series of CAMAC modules to a SLAC-built board situated in the VAX Unibus. A SLAC-written device driver links the signal on the Unibus with a user written program (in this case, CONTROL) awaiting the interrupt. This interrupt initiates a buffered CAMAC operation to read the entire detector and release the inhibit that latched the event.

The electronics are now free to latch another event while CONTROL runs a quick consistency check on the data, ensuring that check words are present and byte counts are correct. The fast online software filter described above spends $\sim$15 ms rejecting obvious junk events and doing crude event classification. Using the software filter, a physicist can trivially set up conditions suitable for various test runs (e.g. endcap cosmic-ray runs) or change trigger requirements with only minimal electronics reconfiguration.

For a typical event of ~1500 bytes the inhibit remains asserted for 16–20 ms. A typical data run trigger rate is ~4 Hz and results in ~10% deadtime. CONTROL also generates random triggers, synchronized with beam crossings at a rate that is user-selected (normally once every 30 seconds).

If the data are acceptable and satisfy the online filter, they are passed to the LOGGER process for storage on disk. LOGGER, running at an elevated priority slightly lower than CONTROL, handles other miscellaneous logging and data acquisition chores as well: sampling and logging the luminosity monitor system; logging hardware monitor records (every 8 minutes); reading and logging trigger scalers (every 30 seconds); logging flags for conditions such as "begin run" and "end run;" logging various data from the calibration runs at the start of a data run; etc. Finally, LOGGER is responsible for updating the "history" files. These files contain all the information deemed historically relevant for the data run, and are essentially an automated logbook.

Running at normal user priority, the MAC process is used by the physicist on shift to begin, end, and otherwise control the data run. As time permits, MAC samples and histograms the data according to the physicist's interests. Various error messages about data errors, hardware out of tolerance, insufficient disk space, etc., also appear at the MAC console for the shift person to handle. New routines and modifications are continually being incorporated into MAC, but the isolation from CONTROL and LOGGER is such that should a problem cause MAC to abort, data taking continues unaffected.

Other users may run other MAC processes at the same time, although only one can control the data run. The others "replay" data previously recorded, and are typically used to debug new software or check the operation of various parts of the detector. Some segments (such as the graphics display routines) are the same as in the offline analysis program, and every attempt is made to prevent divergence of the online and offline versions.

Other miscellaneous independent processes exist to control various aspects

of the experiment such as: provide software control of the trigger counter high voltages through a LeCroy CAMAC interface; receive information about PEP's performance, broadcast by the PEP Control VAX at about 40 second intervals; read in and monitor various hardware at three minute intervals; sample the data on disk, looking for long term changes in the data integrity; schedule miscellaneous VAX housecleaning chores; and monitor the LLA hardware for requests for data transfers. A separate utility program guides the physicist on shift through a disk cleanup, indicating old data files that can be erased to make room for new data.

The data still must be sent to the central IBM system for analysis. This data flow is controlled on the IBM by a "disconnected service machine." This process has a list of tasks to perform, after which it hibernates for one hour and then goes through the list again. When it first wakes up, it sends a query to the VAX via the LLA requesting the list of recent runs logged on disk. After this list is received, it interrogates its database to see which of the recent runs have not yet been stored on the IBM. Requests are again sent down the LLA to the VAX for those runs, and the process waits until those runs have been brought to disk on the IBM. As each run arrives, fast-filter jobs are submitted; these are described below. Only when enough data to fill a 6250 BPI tape have been accumulated is a tape written, using the professionally-run tape environment of the SLAC computer center. When no new runs remain to be transmitted from the VAX, the process checks for fast-filter output to be stored on disk, updates databases on both the IBM and the VAX (using the LLA), erases raw data no longer required on disk, performs some other housecleaning, and then hibernates. While this system is dependent on the LLA link and the IBM, sufficient disk space exists on the VAX for the link to be down for about 24 hours with no major effect. Beyond 24 hours, the VAX tape drives are used to store the data temporarily at the experimental region until the link is again functioning. This is seldom necessary.

9.2 Offline data handling

Production analysis consists of sequential steps called PASS0, PASS1 and PASS2[71].

In PASS0, the run data are scanned quickly for Bhabha scattering events which have clean back-to-back showers in the electromagnetic calorimeters. Tracks in the CD are reconstructed for these events, and if there are precisely two collinear tracks they are constrained to originate from the same point. The fit is repeated with the electron drift velocity as an additional parameter. If there are more than 50 such events in the run, an average velocity and beam crossing position is inferred. The results are written into a run-by-run constants file.

Events of possible physics interest are selected in PASS1. Background is rejected, events are tagged as described below, and data-summary records are created from the results of event reconstruction. Approximately 10% of online-selected events are saved at this stage.

Event selection is implemented by assigning a set of "attributes" which could indicate that the event is of interest. Some are trivially obtained, such as the number of scintillator trigger counters fired or total hits in the CD; some are calculated very quickly, such as rough energy sums in the calorimetry, and some require hundreds of milliseconds, such as full CD and OD track reconstruction. A set of attributes and the cuts that are to be applied to them are collectively referred to as a "mask," and the event must satisfy all the cuts in a mask for that mask to be passed. The selection is made logically complete by defining other masks representing other possible processes. For retention in the PASS1 file at least one such mask must be passed.

To minimize computer usage, the masks are organized into levels such that the attributes used in the lowest level require minimal computation time. Only if at least one mask of a lower level is passed are the attributes required for the higher level calculated. Furthermore, within a mask the tests are made in

sequence and stop if any cut is not satisfied. Further optimization is realized by at least roughly ordering the attributes by computation time required for each.

The number codes of the masks passed in the filtering process are saved, and these can later be used to select event samples for further analysis. The masks are used only for rough selection of data samples, again to save computation time, in part because the selection of events representing a specific physics process can rarely be defined *a priori*.

Once an event has been selected, all track reconstruction has been completed. A summary record is filled with the CD track reconstruction data and thrust quantities calculated both from CD tracking information and from calorimetric energy flow, and written as output. Finally the raw data record is written, indicating the end of the event in the PASS1 data file.

Detailed analysis of events is left for PASS2, which simulates reconstruction by filling data banks from the summary records of PASS1, and redoing reconstructions which require minimal times. However, it is possible to specify that reconstruction should be redone, if necessary, by flagging this requirement with a "runcard." A runcard is a command line in an input file to the program which can specify input and output options, logical branching within the program, and values of constants. Runcards also function as instructions to the job submitting procedure, defining I/O units and graphics devices. One especially useful feature derives from the naming convention for files: three letters and a five digit run number. If a range of run files is specified for processing, one runcard causes all available files with the same prefix and with numbers in the given range to be read sequentially.

Computing time and data storage space is saved by the use of "LIST" files, which are files containing the run and event numbers of selected events. Optionally up to 100 words of data can be attached to the list entry. When both the data and list files are provided to the program, only events specified in the list are processed, and the additional data in the list can be used. In many cases

analysis can proceed using the extended list only.

PASS2 analysis is done via a large offline program which normally calls user-written analysis routines. The program contains the mechanism for obtaining and unpacking events, event display graphics, etc. Part of the offline graphics display for an event is shown in Fig. 3.

9.3 Monte Carlo event simulation

The purpose of the Monte Carlo program is to generate hypothetical e^+e^- interaction events and produce output event records, identical in format to real data records, that simulate the response of the MAC detector. These pseudoevents can then be subjected to the same physics analysis as real events, in order to study the effects of the apparatus and analysis procedures. The Monte Carlo simulation proceeds in three steps: event generation, detector simulation, and hardware trigger simulation. In the event generation step, e^+e^- reactions are simulated based on physics theory such as QED and the standard electroweak model [72]. For each generated event, the final state particle information is saved, including particle types, four momenta, and vertex positions. In the detector simulation step, all the stable particles are tracked through the detector, taking into account magnetic fields, multiple scattering, and electromagnetic and nuclear interactions in the detector material. Each time a particle crosses into a detector element its response is simulated, including time digitization in the drift chamber, energy deposition in the calorimeter PWCs and triggering scintillation counters. In the trigger simulation step, the hardware trigger and online software trigger conditions are simulated based on the detector response generated in the previous step.

The challenge is to reproduce faithfully the characteristics of electromagnetic and hadronic cascade showers in the calorimeter, particularly for complex events such as multihadron final states. The core of the detector Monte Carlo consists of two application-oriented computer programs: EGS (Electron-Gamma-Shower code) [73] and HETC (High Energy Transport Code) [74]. EGS simulates the interaction of electrons and photons with matter, and HETC does the same for

hadrons and muons. Since these two program have a similar structure, they are integrated into one detector Monte Carlo program. The program specifying the MAC detector geometry and the program simulating detector response are written independently from these shower simulation programs. Therefore, both EGS and HETC are able to call these MAC related programs directly, and HETC can call EGS internally to simulate γ showers from π^0's created in nuclear interactions in the detector material.

Most of the important physical characteristics of the MAC detector have been included in the detector simulation: the beam pipe, the aluminum walls and stainless steel end plates of the central drift chamber, the solenoid coil, the aluminum extrusions of the PWC system and the lead-alloy radiator plates of the shower chamber, the scintillation counters, the iron plates of the hadron calorimeters, the chamber frames of the endcap chambers, and the gas mixtures inside the PWCs. It has been found that inclusion of the aluminum extrusions of the shower chamber is essential for reproducing both the energy resolution and the longitudinal and transverse development of electromagnetic showers. The aluminum wall absorbs low energy (few MeV) shower particles which otherwise traverse long distances in the PWC and create large fluctuations.

As an illustration of the simulation, the decay γ-rays from a a wide-angle π^0 are shown striking part of the detector in Fig. 4. One of the γ-rays converts in the solenoid coil, while the other penetrates fairly deeply into a CSC sextant before the cascade starts.

An important modification to EGS and HETC has been implemented in the treatment of energy loss by charged particles in the PWC gas. In place of a fixed average energy loss per track crossing the PWC, the actual energy loss in the gas is allowed to fluctuate according to a modified Landau distribution. In principle, the energy-loss fluctuations can be simulated by tracking the shower particles down to the keV energy range. However, the computation time becomes too long to be practical. The shower particles are tracked down to about 1 MeV, and the energy

loss is sampled from the distribution using the shape of the measured single-gap minimum-ionizing spectrum [75] with the scale set by the most probable energy loss computed according to the prescription of Talman [76].

For the purpose of a complete description of the energy deposition in the calorimeter, a few hadrons unknown to HETC must be replaced by familiar particles of the same momenta in the central drift chamber and same kinetic energy in the calorimeter; $K^{\pm} \rightarrow \pi^{\pm}$, $K^0_{\text{long}} \rightarrow n$, $\bar{p} \rightarrow \pi^-$, and $\bar{n} \rightarrow n$. The K^+ lifetime is retained, however, for its weak decay.

The shower simulations using EGS and HETC can reproduce fluctuations and correlations of energy deposition realistically, but run very slowly. The average hadron event takes about six seconds of IBM 3081K CPU time.

10. Luminosity monitor

Online monitoring of the PEP luminosity during MAC data collection is provided by a set of four scintillation counter telescopes located symmetrically near the beam pipe, two at each end of the IR hall. This system is designed to trigger on small-angle Bhabha scattering events with high efficiency, low background, and accurately defined acceptance.

Each of the four identical detector packages consists of three trigger scintillators followed by a lead-scintillator sandwich electromagnetic shower counter. These modules are placed symmetrically on both sides of the beam line, each centered at a polar angle of 1.72° from the beam at both ends of the experimental hall. The trigger counters consist of square pieces of 0.64 cm thick plastic scintillator connected to photomultiplier tubes by acrylic light guides, and range from 3.16 cm to 5.70 cm on a side. The smallest of these defines the aperture and is located 4.72 m from the interaction point. All are accurately machined, measured, and aligned. Each shower counter consists of 15 layers of alternating lead (0.64 cm thick) and acrylic scintillator (1.27 cm thick). Acrylic waveshifter

sheets and light guides transmit the emitted light to a photomultiplier tube. The energy resolution for electrons is found to be approximately $\sigma_E/E \sim 20\%/\sqrt{E}$ based on both test beam measurements from 4 to 16 GeV and on actual Bhabha scattering events at $E = 14.5$ GeV.

Two fast coincidences are constructed for each of the four detector telescopes. These require a hit in the shower counter and (a) the largest trigger counter only ("loose") or (b) all three trigger counters ("tight"). Four luminosity triggers are formed by requiring a tight coincidence in one telescope with a loose coincidence in the opposite one. The tight coincidence defines the acceptance, while the aperture of the opposite loose coincidence is sufficient to allow for effects of finite beam size, magnetic fields, and multiple scattering. The tight coincidence includes a third, redundant trigger counter to reduce false coincidences caused by photons emitted backwards from the shower counter. The luminosity measurement is based on the sum of the four individual tight-loose combinations. This sum is independent of deviations in beam position and direction as well as detector positioning, to first order in the deviations. Asymmetries in the four rates can be used to calculate the approximate sizes of the offsets and hence a second order correction.

The lowest-order cross section σ_0 was evaluated using two independent integrations, one analytic and the other using standard Monte Carlo techniques. Both gave

$$\sigma_0 = 15.71 \text{ nb} \times \left(\frac{15 \text{ GeV}}{E_0}\right)^2$$

to an accuracy of 0.1%. Radiative corrections to the Bhabha scattering cross section were calculated to order α^3 using a Monte Carlo event generator by Berends and Kleiss [77]. A systematic error of $\pm 1.5\%$ was assigned to the calculation, including an estimate of the maximum effect of higher-order corrections. Corrections are also made for counter inefficiencies and small background sources. Systematic uncertainties in these quantities contributed a total error of $\pm$ 2.3%.

A further error of $\pm$ 2% was assigned for possible detector misalignment, primarily in the horizontal separation of the pairs of defining counters at each end. The total systematic uncertainty in the luminosity measurement was then $\pm 3.4\%$.

11. The MAC monitor system

Regular monitoring of voltages, currents, pressures, temperatures and other parameters of the detector subsystems is necessary to assure proper operation and safety. The MAC monitor system consists of about 1000 analog channels connected to probes distributed around the detector and the electronics. The bulk of the channels are connected to a SLAC monitor chassis system [78] which contains special electronics cards for each type of probe, providing the appropriate termination, current overload protection and power (if needed). The crate is controlled through the CAMAC system with a Kinetic Systems IGOR 3061 Output Register [79] and can be commanded to connect any analog channel, through a set of multiplexers, to a Kinetic Systems 3553 CAMAC ADC for measurement of its DC voltage output. The rest of the monitor channels are from the LeCroy HV4032 High Voltage Photomultiplier Supply, which is connected through an interface to the CAMAC system.

The channels are polled sequentially every two minutes by a task running on the online computer and stored in globally shared memory. Also in globally shared memory is a map used to convert the raw information into a conveniently accessible form. The map forms logical groups from the different channels (such as "all the central drift chamber voltages") and contains calibration constants to convert the raw DC voltages to the appropriate units. Also contained in the map are individual limits indicating the normal range for each channel's reading. If a reading is found to be outside this range, an error message is displayed on the online control terminal. The monitor system can be interrogated through a simple interactive program available from any terminal.

The raw monitor information is added to the current data file every eight minutes. This information is unpacked and mapped (as described above) automatically by the offline analysis package and is made available to the user in a FORTRAN common block. At this point the information can be used, for example, to calculate gain corrections for the calorimeter response based on voltage, pressure, temperature and gas gain readings.

Acknowledgments

We thank the very large number of designers, engineers, craftsmen, technicians, machine builders, and lonely owl shift operators whose skills and dedication brought the PEP machine and the MAC detector from concept to reality. We especially acknowledge the efforts of Norma Erickson, Don Clark, Justin Escalera, Mike Frankowski, and Jack Schroeder, who worked full-time building, maintaining, and modifying the detector. We profited from the engineering skills of Tom Pulliam, who is missed by all who knew him. Charlie Hoard's analytical ability provided a solid engineering foundation for the structure of the detector. Maureen Richards provided the administrative ability and continuity required for smooth operation of the collaboration. We are also grateful for the technical assistance of many other contributors such as Ed Askeland, Dieter Freytag, John Broeder, and staff members at the various universities.

This work was supported in part by the U. S. Department of Energy under contracts DE–AC02–86ER40253 (CU), DE–AC03–76SF00515 (SLAC), and DE–AC02–76ER00881 (UW); by the National Science Foundation under contracts NSF–PHY82–15133 (UH), NSF–PHY82–15413 and NSF–PHY82–15414 (NU), and NSF–PHY83–08135 (UU); by the Istituto Nazionale di Fisica Nucleare; and by the U.S./Japan Cooperative Program in High Energy Physics (agreement signed 12 November 1979).

References

(a) Permanent address: CERN, CH–1211 Genève 23, Switzerland.

(b) Present address: Dept. of Physics, Union College, Schenectady NY 12308.

(c) Present address: Deutsche Forschungs- und Versuchsanstalt für Luft- und Raumfahrt, PT–PM4, P.O. Box 906058, D–5000 Cologne 90, FRG.

(d) Present address: MPI, München, FRG.

(e) Present address: CERN, CH–1211 Genève 23, Switzerland.

(f) Present address: Los Alamos National Laboratory, Los Alamos NM 87545.

(g) Present address: SSC Central Design Group, LBL 90–4040, Berkeley CA 94720.

(h) Present address: Laboratori de Física d'Altes Energies, Universitat Autònoma de Barcelona, E–08193 Bellaterra, Spain.

(i) Present address: Fermi National Accelerator Center, Batavia IL 60510.

(j) Deceased.

(k) Present address: Cyclotron Laboratory, Harvard University, Cambridge MA 02138.

(l) Present address: Laboratory of Nuclear Studies, Cornell University, Ithaca NY 14853.

(m) Present address: INFN, Sezione di Genova, I–16146, Genova, Italy.

(n) Present address: Advanced Decision Systems, 1500 Plymouth Street, Mountain View CA 94043–1230.

(o) Present address: Department of Physics, Chungnam National University, Daejeon, Korea.

(p) Present address: 20 Caine Road, Hong Kong, B. C. C.

(q) Present address: Physics Department, University of Padua, Padua, Italy.

(r) Present address: #307–101 Coe Hill Drive, Toronto, Ontario, Canada M6S 3E3.

(s) Present address: Digital Equipment Corp., 305 Rockrimmon Blvd., Colorado Springs, CO 80919.

(t) Present address: Friedastrasse 1A, 8000 München, FRG.

(u) Present address: Veterans Administration Medical Center, Palo Alto CA 94304

(v) Present affiliations: Laboratori Nazionali di Frascati dell'INFN, Italy, and Dipartimento di Fisica, Universitá di Perugia, Perugia, Italy.

(w) Present address: P. O. Box 918–1, Beijing, The People's Republic of China.

(x) Present address: Institute of Physics, University of Oslo, P. O. Box 1048, Blindern, Oslo 3, Norway.

(y) Present address: QMS Inc., Santa Clara CA 95052.

(z) Present address: Enrico Fermi Institute, University of Chicago, Chicago IL 60637.

(aa) Present address: Wang Laboratories, Inc., Lowell MA 01851.

(ab) Present address: Stanford Hospital, Stanford CA 94305.

(ac) Present address: Department of Physics, Vanderbilt University, Nashville TN 37235.

(ad) Present address: Sezione INFN de Pisa, I–56010 San Piero a Grado (PI), Italy.

(ae) Present address: Integration and Test Department, McDonnell-Douglas Astronautics Co., St. Louis MO 63166–0516.

(af) Present address: Neuron Data, Palo Alto CA 94301.

1. W. T. Ford *et al.*, Phys. Rev. Lett. **49** (1982) 106–109.

2. E. Fernández *et al.*, Phys. Rev. Lett. **50** (1983) 1238–1241.

3. E. Fernández *et al.*, Phys. Rev. Lett. **50** (1983) 2054–2057.

4. W. T. Ford *et al.*, Phys. Rev. Lett. **51** (1983) 257–260.

5. E. Fernández *et al.*, Phys. Rev. Lett. **51** (1983) 1022–1025.

6. E. Fernández *et al.*, Phys. Rev. **D28** (1983) 2721–2725.

7. E. Fernández *et al.*, Phys. Rev. Lett. **52** (1984) 22–25.

8. E. Fernández *et al.*, Phys. Rev. Lett. **54** (1985) 95–98.

9. E. Fernández *et al.*, Phys. Rev. Lett. **54** (1985) 1118–1121.

10. E. Fernández *et al.*, Phys. Rev. Lett. **54** (1985) 1620–1623.

11. E. Fernández *et al.*, Phys. Rev. Lett. **54** (1985) 1624–1627.

12. W. W. Ash *et al.*, Phys. Rev. Lett. **54** (1985) 2477–2480.

13. W. W. Ash *et al.*, Phys. Rev. Lett. **55** (1985) 1831–1834.

14. W. W. Ash *et al.*, Phys. Rev. Lett. **55** (1985) 2118–2121.

15. E. Fernández *et al.*, Phys. Rev. **D31** (1985) 1537–1556.

16. E. Fernández *et al.*, Phys. Rev. **D31** (1985) 2724–2731.

17. W. T. Ford *et al.*, Phys. Rev. **D33** (1986) 3472–3475.

18. E. Fernández *et al.*, Phys. Rev. **D35** (1987) 1–9.

19. E. Fernández *et al.*, Phys. Rev. **D35** (1987) 10–18.

20. E. Fernández *et al.*, Phys. Rev. **D35** (1987) 374–377.

21. W. T. Ford *et al.*, Phys. Rev. **D35** (1987) 408–411.

22. W. W. Ash *et al.*, Phys. Rev. Lett. **58** (1987) 640–643.

23. W. W. Ash *et al.*, Phys. Rev. Lett. **58** (1987) 1080–1083.

24. W. W. Ash *et al.*, Nucl. Instr. Meth. **A261** (1987) 399–419.

25. W. T. Ford *et al.*, Phys. Rev. **D36** (1987) 1971–1982.

26. H. R. Band *et al.*, Phys. Rev. Lett. **59** (1987) 415–418.

27. H. R. Band *et al.*, Phys. Lett. **198B** (1987) 297–301.

28. H. R. Band *et al.*, Phys. Lett. **200B** (1988) 221–225.

29. H. R. Band *et al.*, Phys. Lett. **218B** (1989) 369.

30. W. T. Ford *et al.*, (submitted to Phys. Rev., 1989).

31. B. K. Heltsley, *Measurement of the Total Cross Section and Energy-Energy Correlations for Electron-Positron Annihilation into Hadrons at 29 GeV*, Ph.D. Thesis at University of Wisconsin–Madison, WISC–EX–83/233 (July 1983).

32. Hoyun Lee, *A Study of Acollinear Muon Pair Production in e^+e^- Interactions at $E_{\mathrm{c.m.}} = 29$ GeV*, Ph.D. Thesis, University of Utah, UMI83–25636–mc (Aug. 1983).

33. H. S. Kaye, *Quark Flavor Identification in Electron-Positron Annihilation*, Ph.D. Thesis, Stanford University, Stanford Linear Accelerator Center Report SLAC–Report–262 (Sept. 1983).

34. S. Clearwater, *The Measurement of the Hadronic Cross Section in Electron Positron Annihilation*, Ph.D. Thesis, Stanford University, Stanford Linear Accelerator Center Report SLAC–Report–264 (Nov. 1983).

35. G. P. Goderre, *A High Precision Measurement of Electroweak Effects in $e^+e^- \to \mu^+\mu^-$ at $\sqrt{s} =$ 29 GeV*, Ph.D. Thesis, Northeastern University, NUB 2867 (Oct. 1985).

36. L. J. Rosenberg, *A Study of Hadronization Using Energy Flow from e^+e^- Annihilation into Quarks and Gluons at $\sqrt{s}$ of 29 GeV*, Ph.D. Thesis, Stanford University, Stanford Linear Accelerator Center Report SLAC–Report–289 (Nov. 1985).

37. M. C. Delfino, *Tests of Quantum Electrodynamics and Electroweak Theory using the Reactions $e^+e^- \to \gamma\gamma(\gamma(\gamma))$ and $e^+e^- \to e^+e^-$ at $\sqrt{s} =$ 29 GeV*, Ph.D. Thesis, University of Wisconsin–Madison, WISC–EX–85/263 (Dec. 1985).

38. T. L. Lavine, *Search for Single-Photons from Radiative Production of Supersymmetric Particles or Neutrinos*, Ph.D. Thesis, University of Wisconsin–Madison, WISC–EX–86/275 (Dec. 1986).

39. A. L. Read, *Measurements of Tau Lepton Production at Decay at* $\sqrt{s} = 29$ *GeV*, Ph.D. Thesis, University of Colorado, COLO–HEP–122 (1986).

40. J. P. Venuti, *A Study of Tau Decays to Three Pions*, Ph.D. Thesis, University of Houston, UMI87–14774 (May 1987).

41. NaDing Qi, *Measurement of the Tau Lepton Lifetime*, Ph.D. Thesis, University of Colorado, COLO HEP–160 (July 1987).

42. H. N. Nelson, *Design and Construction of a Vertex Chamber and Measurement of the Average B Hadron Lifetime*, Ph.D. Thesis, Stanford University, Stanford Linear Accelerator Center Report SLAC–Report–322 (Oct. 1987).

43. R. B. Hurst, *A Measurement of Flavor Mixing of Neutral B Mesons*, Ph.D. Thesis, University of Houston, RX–1203 (Dec. 1987).

44. A preliminary description is given in W. T. Ford, *Proc. Int. Conf. on Instr. for Colliding Beam Phys.*, 17–23 Feb. 1982, Stanford Linear Accelerator Center Report SLAC–250.

45. DEC, VAX, VMS, and Unibus are trademarks of Digital Equipment Corp.

46. IBM is a trademark of International Business Machines, Inc.

47. R. Coombes, "Proportional Chamber Construction Information Sheet," MAC Internal Note MAC–NOTE–153 (March 1978).

48. R. L. Anderson *et al.*, IEEE Trans. Nucl. Sci. **NS–25** (1978) 340.

49. Bertan Associates Inc., Hicksville NY 11801.

50. D. Freytag, Stanford Linear Accelerator Center Report SLAC–PUB–2622 (1980).

51. E. L. Cisneros, H. K. Kang, J. N. Hall, and R. S. Larsen, IEEE Trans. Nucl. Sci. **NS–24** (1978) 413.

52. CAMAC is a standardized two-way computer interfacing system, electrically and mechanically conforming to the standards described by IEEE Standards 583 and 596 (original versions in ESONE Reports EUR–4100 and EUR–4160 or U.S. AEC Report TID–26614).

53. M. Breidenbach, E. Frank, J. Hall, and D. Nelson, IEEE Trans. Nucl. Sci. **NS-25** (1978) 706.

54. DEOXO Purifier, Engelhard Industries, Union NJ 07083.

55. Model 315 Trace Oxygen Analyzer, Teledyne Analytical Instruments, City of Industry, CA 91749–1580.

56. Type 3A Molecular Sieve, Union Carbide Corp., Linde Div., South Plainfield, NJ 07080.

57. T. L. Lavine, MAC Internal Note MAC–NOTE–632 (Oct. 1982).

58. A. L. Read, MAC Internal Note MAC–NOTE–745 (Feb. 1986).

59. LABEN, Via Bassini 15, 20133 Milano, Italy.

60. E. Fernández *et al.*, , Stanford Linear Accelerator Center Report SLAC–PUB–3390 (August 1984).

61. G. Blanar, H. Dietl, E. Lorenz, F. Pauss, and H. Vogel, "Bismuth Germanate, a Novel Material for Electromagnetic Shower Detectors," Max-Plank-Institut, München, Report MPI–PAE/Exp. El.94 (1981).

62. G. Blanar *et al.*, Nucl. Instr. Meth. **203** (1982) 213–221.

63. D. E. Groom, Nucl. Instr. Meth. **219** (1984) 141–148.

64. Nihon Kessho Koogaku Co., Ltd., 318–19 Kondo, Tatebayashi-City, Gunma-pref., Japan.

65. Solid State Division, Hamamatsu Photonics KK, 1126–1 Ichino-cho, Hamamatsu City 435, Japan.

66. K. Yamamoto, J. Fujii, Y. Kotooka, and T. Katayama, Nucl. Instr. Meth. A**253** (1987) 542–547.

67. Nuclear Enterprises, Inc., San Carlos, CA 94070.

68. LeCroy Corp., 700 Chestnut Ridge Road, Chestnut Ridge NY 10977–6499.

69. B. Gottschalk, Nucl. Instr. Meth. **190** (1981) 67.

70. Jorway Corp., Westbury NY 11590.

71. M. Delfino, Comp. Phys. Commun. **45** 467–471 (1987).

72. F. A. Berends and R. Kleiss, Nucl. Phys. **B228** (1983) 537; F. A. Berends, R. Kleiss, and S. Jadach, Nucl. Phys. **B202** (1982) 63, for QED and electroweak. T. Sjostrand, Comp. Phys. Commun., **28** (1983) 229; T. Sjostrand and M. Bengtsson, Comp. Phys. Commun., **43** (1987) 43, for QCD. These papers contain representative descriptions of the Monte Carlo programs.

73. W. R. Nelson, H. Hirayama and D. W. O. Rogers, "The EGS4 Code System," Stanford Linear Accelerator Center Report SLAC–265 (Dec. 1985).

74. R. G. Alsmiller, Jr. *et al.*, "Modifications of the High Energy Transport Code (HETC) and Comparisons with Experimental Results," presented at the ANS Topical Conference on Theory and Practices in Radiation Protection and Shielding, 22–24 April 1987, Knoxville, Tennessee; K. C. Chandler and T. W. Armstrong, "Operating Instructions for the High-Energy Nucleon-Meson Transport Code HETC," Oak Ridge National Laboratory Report ORNL–4744 (1972).

75. R. Ehrlich *et al.*, Cornell University Laboratory of Nuclear Studies Report LNS–82/521 (1982).

76. R. Talman, Nucl. Instr. Meth. **159** (1979) 189.

77. F. A. Berends and R. Kleiss, Nucl. Phys. **B177** (1981) 237.

78. J. Kieffer, IEEE Trans. Nucl. Sci. **NS-28** (1981) 646.

79. Kinetic Systems Corp., 11 Maryknoll Dr., Lockport IL 60441.

Table 6–1

Numbers of identified muons found at increasingly restrictive stages of muon identification used in Ref. 28.

Muon Identification	Data	Monte Carlo Prediction
OD track	16313	15528 ± 125
OD–HC match	12845	12275 ± 111
Punch cuts	9544	9595 ± 98
OD–HC and CD match	5450	5496 ± 74
All cuts	2866	2837 ± 53

Figure Captions

1. Isometric view of the MAC detector. Endcaps are in the open position, and the outer muon drift system is cut away for clarity.

2. Plan view of the MAC detector. The labeled components are the vertex detector (VC), central drift chamber (CD), central shower chamber (CSC), trigger/timing scintillators (TOF), central and endcap calorimeters (CHC, EC), the outer muon drift chambers (OD), and the small angle veto system (SAV). The toroid and solenoid coils are also indicated.

3. A 29 GeV multihadron event as reconstructed by the offline software. (a) A south-looking overall view of the central section, showing information from the central calorimeters, central drift chamber, and central scintillators. Bar lengths of hits in the calorimeters indicate energy found in each cell. Thin lines joining layers are reconstructed associations. The reconstructed energy in the shower chamber is 20.3 GeV, while in the hadron calorimeter it is 10.9 GeV. (b) An overall view of the detector with a cut parallel to the beam line through the sextants in which most activity occurs. The high-momentum muon reconstructed in the outer drift system tags the event as a $B\overline{B}$ candidate. (c) The central drift chamber hits and reconstruction, with the vertex chamber hits also indicated. (d) Further enlargement of the vertex chamber, where the radii of the hit circles are calculated from the timing. (f) Extreme enlargement of the vertex region, with the 1 σ beam profile indicated by the ellipse.

4. Cross section of one sextant of the central electromagnetic calorimeter, showing an EGS4 simulation of π^0 decay γ-ray cascades. Solid lines indicated electrons and dotted lines indicate photons. The first γ-ray converts in the solenoid coil.

5. Segmentation of the calorimeter. (a) Side view of one quadrant of the calorimeter, showing the segmentation in depth of the central section and

endcaps as well as the polar angle segmentation in the endcaps. The shaded region comprises the "shower layers," where photons and electrons deposit most of their energy. The unshaded region comprises the "hadron layers." (b) Azimuthal segmentation of the central section calorimeter, where each layer in depth has 16 separate ϕ segments in each 30° twelfth. (c) Segmentation of an endcap twelfth.

6. Typical pulse height distributions from the CSC for Bhabha scattering events (a) before and (b) after gain corrections.

7. Construction details of a 30° endcap PWC module.

8. Distribution of differences between thrust directions determined from the generated quarks (plus gluons and photons, if any) and from the corresponding final-state particles for Monte-Carlo generated events at $\sqrt{s}$ = 29 GeV. Solid line: thrust axes calculated from exact energies and directions of final state hadrons after quark fragmentation. Dashed line: energy-flow thrust directions determined from the simulated MAC detector response to the same hadrons.

9. The distribution of total MAC calorimeter response for a sample of 29 GeV $e^+e^- \rightarrow$ *hadrons* events at PEP (solid histogram). The multihadronic events were selected to have final states with thrust values larger than 0.9 and thrust directions at more than 60° from the beam. The dashed histogram shows the simulated detector response for a comparable sample of Monte Carlo events.

10. Decoupling electronics for the proportional chambers in (a) the central electromagnetic calorimeter and first two layers of the central hadron calorimeter, and (b) the endcap calorimeter and third layer of the central hadron calorimeter.

11. Block diagram of the MAC gas system.

12. Results of a week-long gas gain calibration run. In this case the same gas

flowed through the "unknown" and reference chambers.

13. Central drift chamber. The length between inside faces of the main end-plates is 189 cm. The outer radius is 48 cm.

14. Structure and electron drift lines of the CD drift cell for (a) layers 1–3, and (b) layers 4–10. Cathode and field shaping wires are indicated by open circles. Sense wires are at the foci of the electron drift trajectories shown by the solid contours. Dashed contours indicate surfaces of constant drift time. Full width is 1.56 cm (2.34 cm) for the small (large) cells; height is 1.1 cm for both.

15. The inverse momentum distribution measured in the central drift chamber for collinear muon pairs. The solid curve is the sum of two gaussian distributions, centered at ± 0.069 $(\mathrm{GeV/c})^{-1}$. The average over all polar angles of the fractional momentum resolution is $\Delta p/p = 0.64$ at 14.5 GeV/c.

16. Beam pipe subassembly on which are mounted the vertex chamber, BGO arrays, local masks, and tungsten shielding.

17. "Miss" distance for Bhabha scattering events. The distributions shown are for the distances between the two tracks at the origin in the plane normal to the beam line. In (a) the electron momenta are free variables in the joint VC–CD fit, while in (b) they are constrained to the beam energy. The smooth curves show gaussian fits.

18. The inverse OD momentum distribution for dimuon events having an acollinearity $\leq 15°$. The solid line is the sum of two gaussians centered at $\pm$ 0.070 $(\mathrm{GeV/c})^{-1}$, with a width of 0.025 $(\mathrm{GeV/c})^{-1}$, giving an OD momentum resolution of 36%. The same dimuon sample as in Fig. 15 is used.

19. The average inverse momentum measured by the OD versus inverse momentum of the CD after corrections. The lines show separate linear fits for the positive and negative tracks.

20. Detection efficiency for muon pairs, as calculated using the detector Monte Carlo program. The effects of all selection and cuts used in Ref. 13 are included, except that scintillation counter efficiency is treated separately.

21. A cross section containing the beam line which shows the positioning of the small-angle-veto proportional wire chambers (SAV) and the small angle scintillation counters (SAT).

22. Construction details of the small-angle-veto proportional wire chambers.

23. One of the four BGO half-cones. One circuit card and the two crystals underneath it have been removed and displayed, with one of the crystals unwrapped. A 15-cm ruler provides the scale.

24. Relative light collection along BGO crystals for various compensation schemes: ◇ – all surfaces finely ground; □ – all surfaces polished; ○ – outer surface ground, others polished.

25. Pulse heights observed from tagged 14.5 GeV Bhabha scattered electrons (a) before and (b) after pulse height correction.

26. Arrangement of the 144 scintillator counters in the MAC trigger system. The size of the endcap planes is chosen so that they are shadowed by the central counters for a source at the interaction point.

27. The distribution of time difference vs. average time for 9876 $\mu^+\mu^-$ candidate events, with loose vertex requirements. A combination of timing cuts and tighter vertex cuts reduces the cosmic ray contamination of the μ-pair sample to $\sim$0.06%.

28. MAC data flow from data acquisition electronics to archive tapes and summary files.

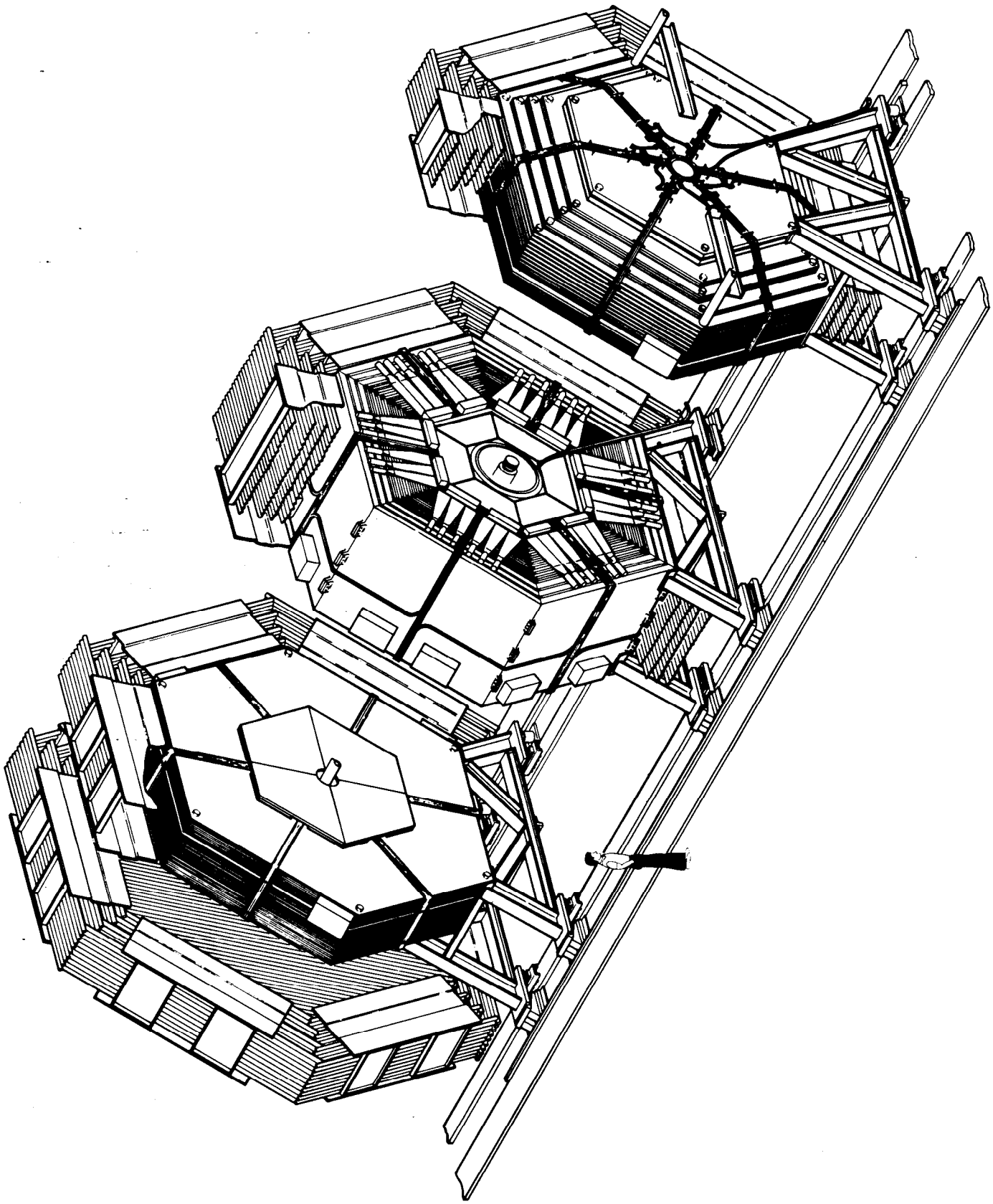

Fig. 1

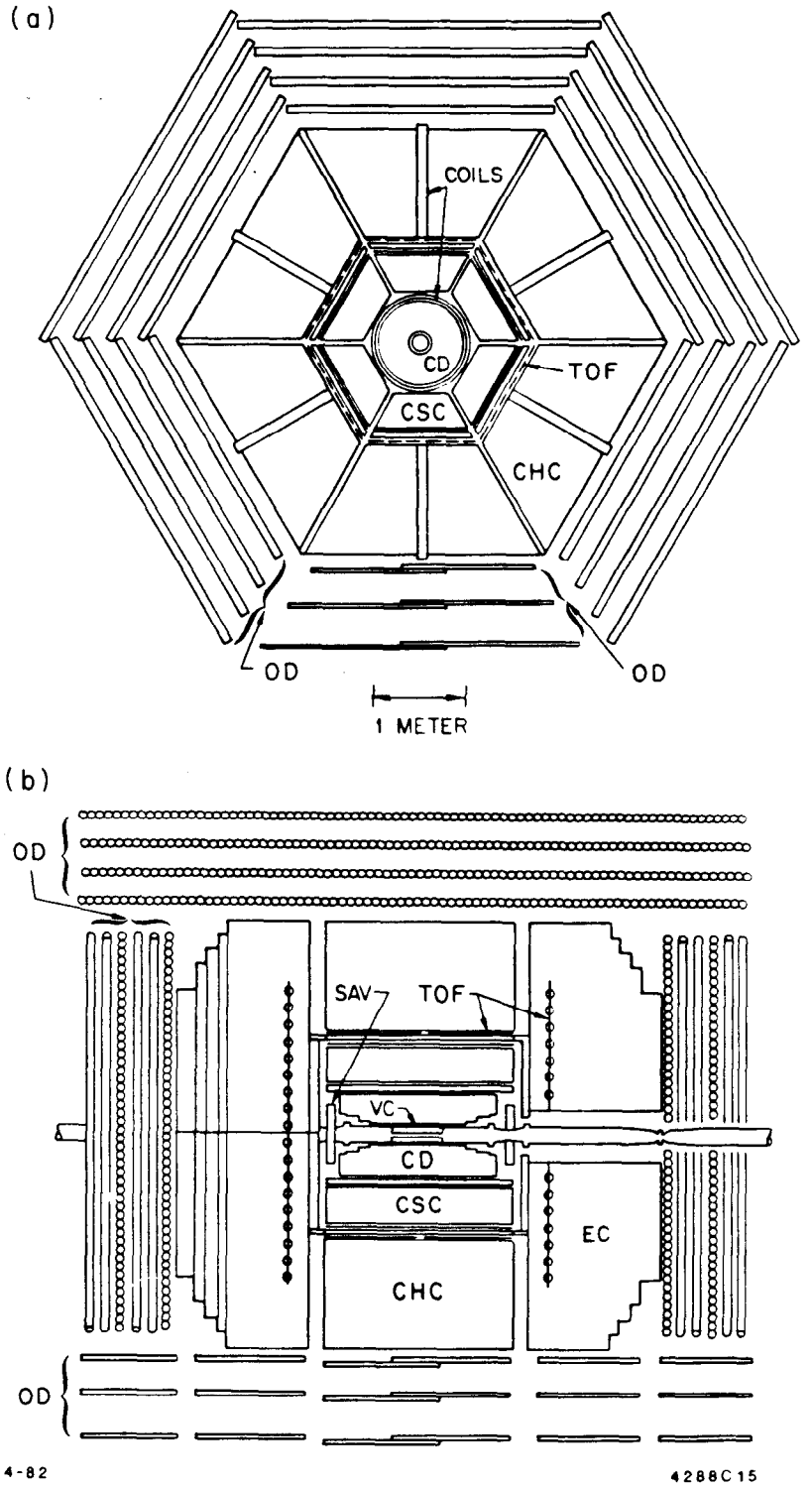
(a)
COILS
CD
TOF
CSC
CHC
OD
OD
1 METER
(b)
OD
SAV
TOF
VC
CD
CSC
EC
CHC
OD
4-82
4288C15

Fig. 2

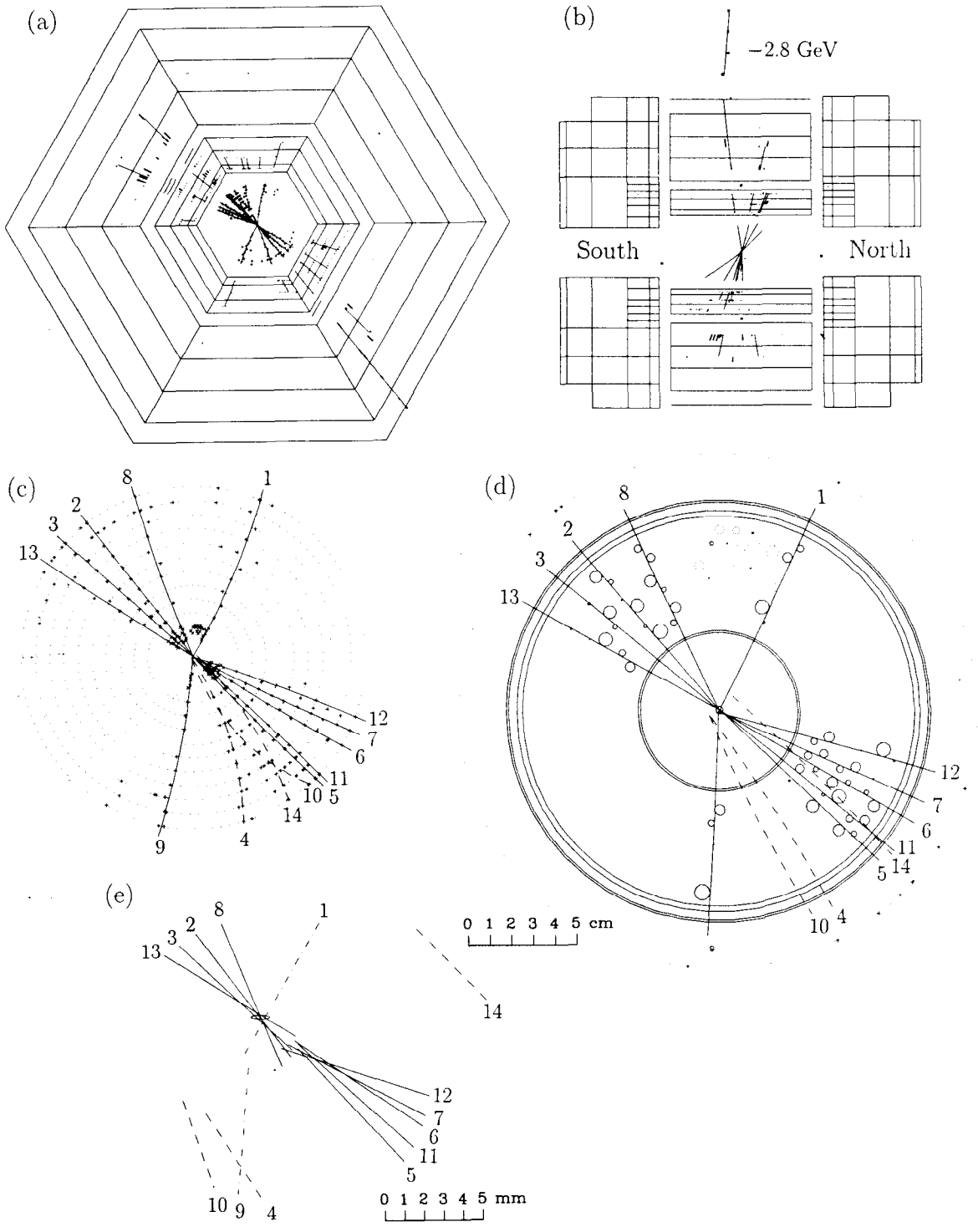

Fig. 3

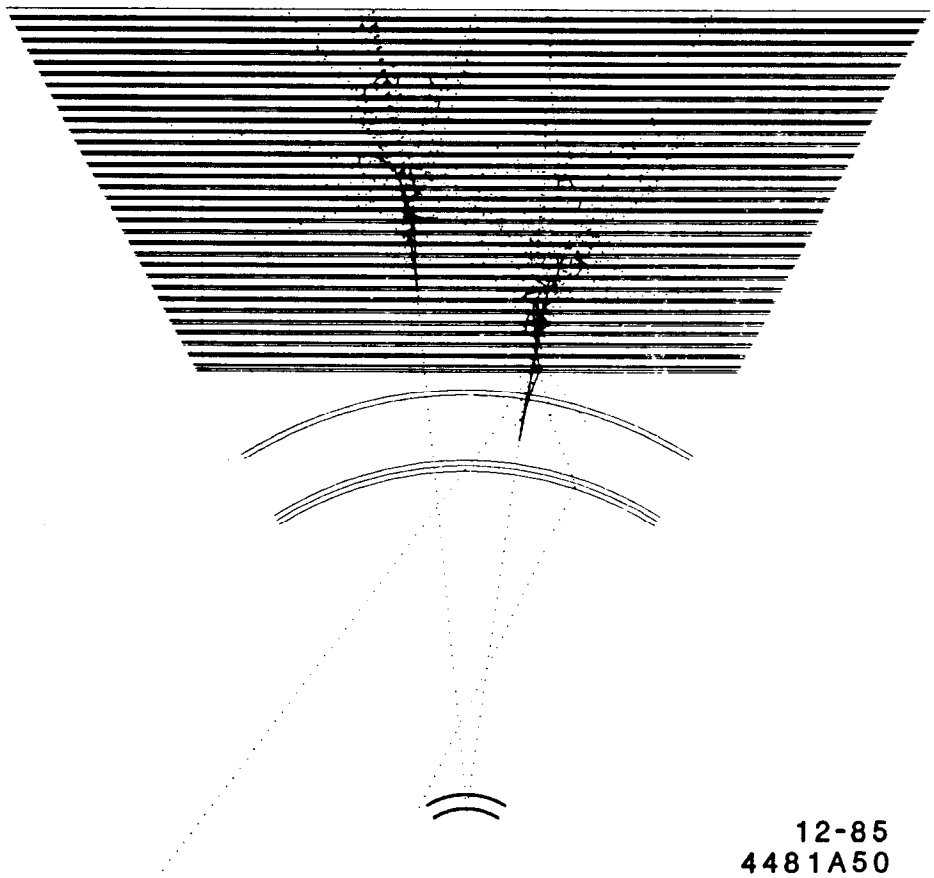

Fig. 4

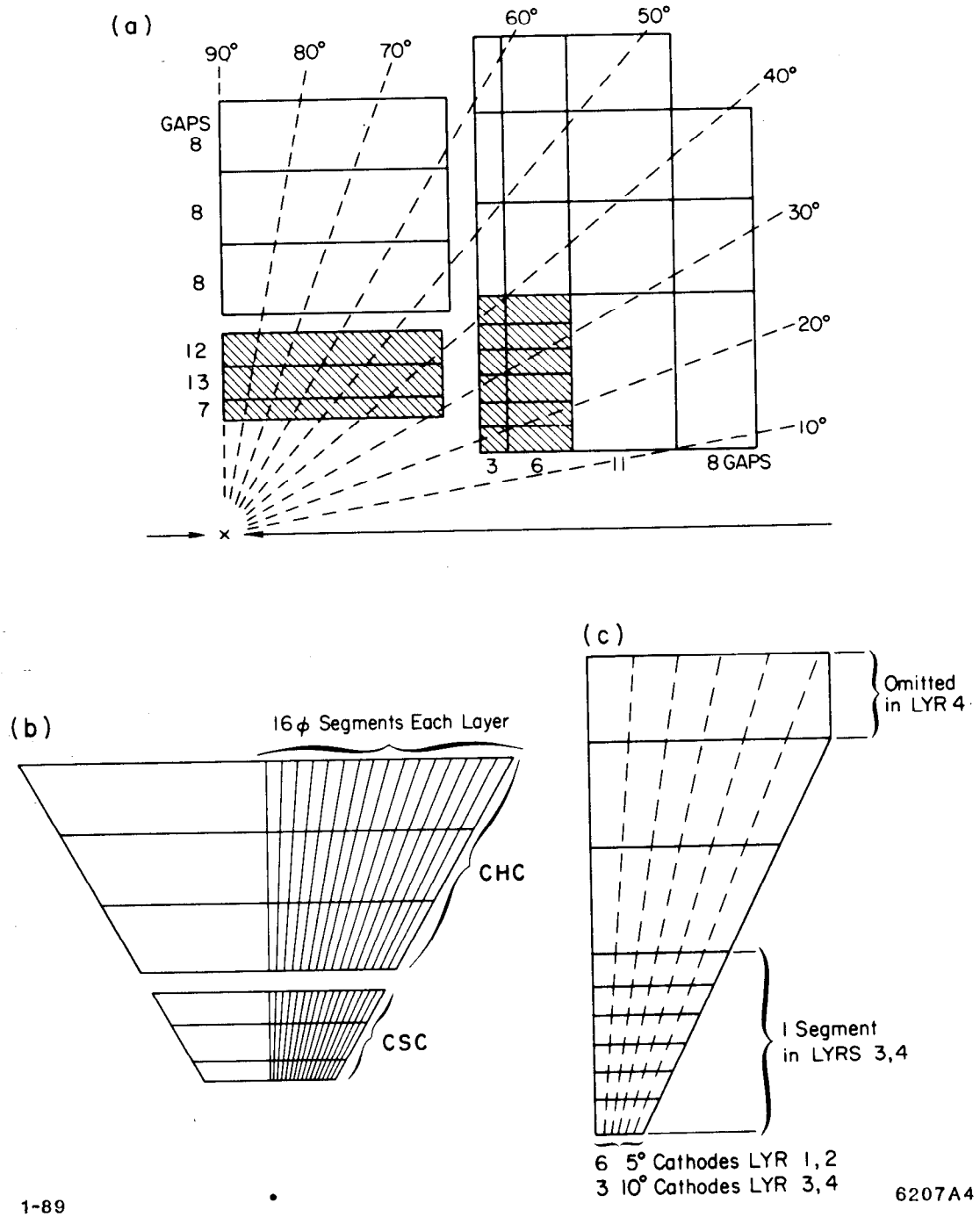
(a)
90°
80°
70°
60°
50°
40°
30°
20°
10°
GAPS
8
8
8
12
13
7
3
6
11
8 GAPS
x
(b)
16 ϕ Segments Each Layer
CHC
CSC
(c)
Omitted
in LYR 4
1 Segment
in LYRS 3,4
6 5° Cathodes LYR 1,2
3 10° Cathodes LYR 3,4
1-89
6207A4

Fig. 5

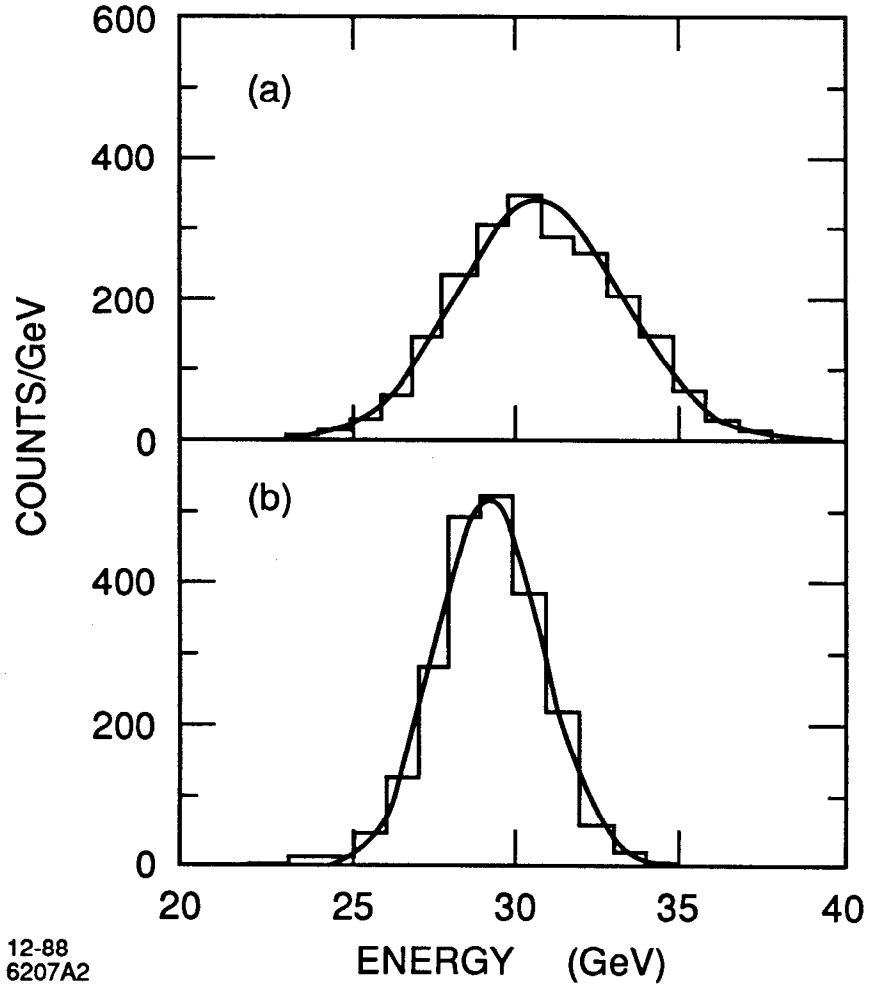
600
400
200
0
(a)
400
200
0
(b)
COUNTS/GeV
20
25
30
35
40
ENERGY (GeV)
12-88
6207A2

Fig. 6

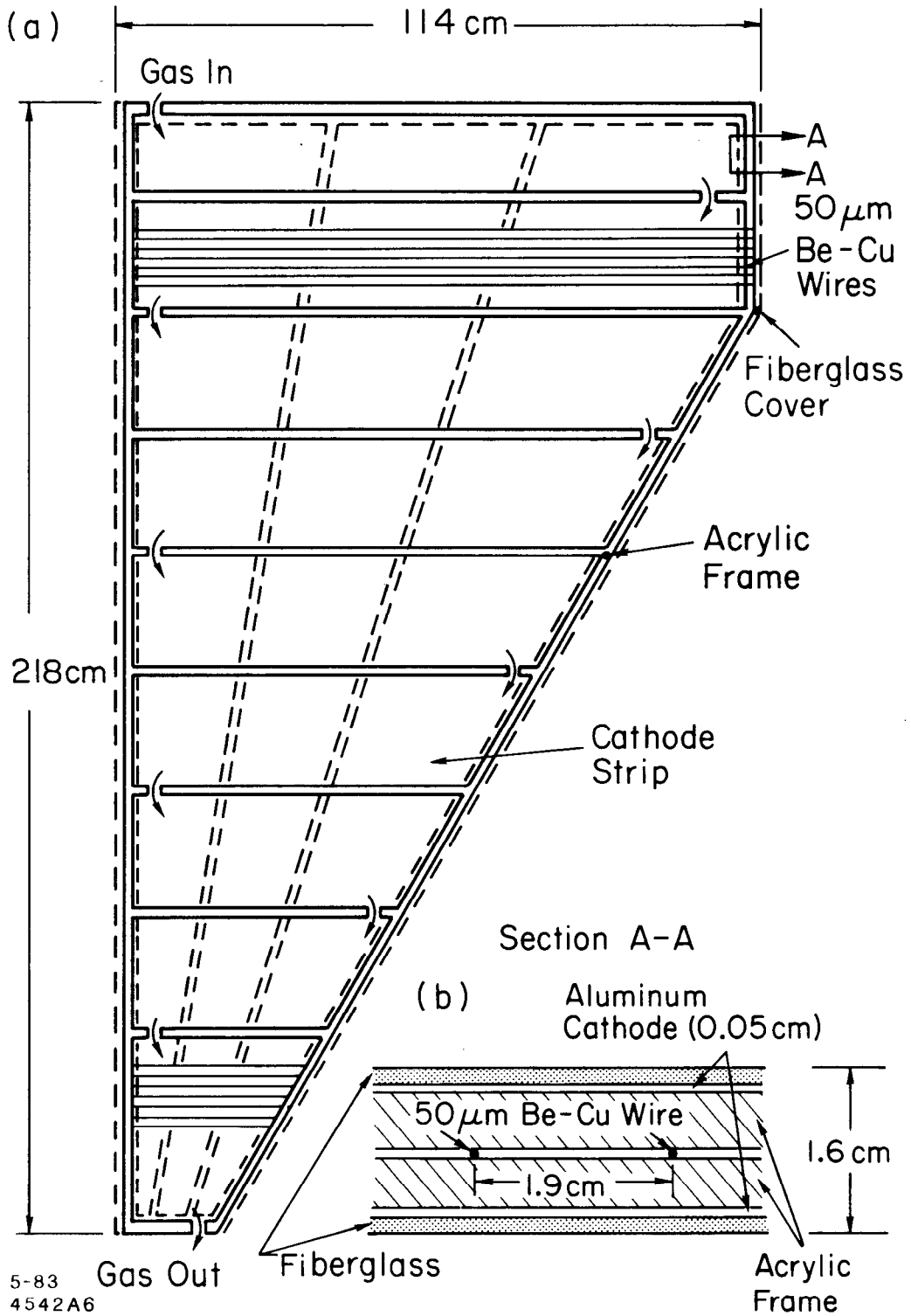
(a)
114 cm
Gas In
A
A
50 μm
Be-Cu
Wires
Fiberglass
Cover
Acrylic
Frame
218cm
Cathode
Strip
Section A-A
(b)
Aluminum
Cathode (0.05cm)
50 μm Be-Cu Wire
1.9cm
1.6 cm
Gas Out
Fiberglass
Acrylic
Frame
5-83
4542A6

Fig. 7

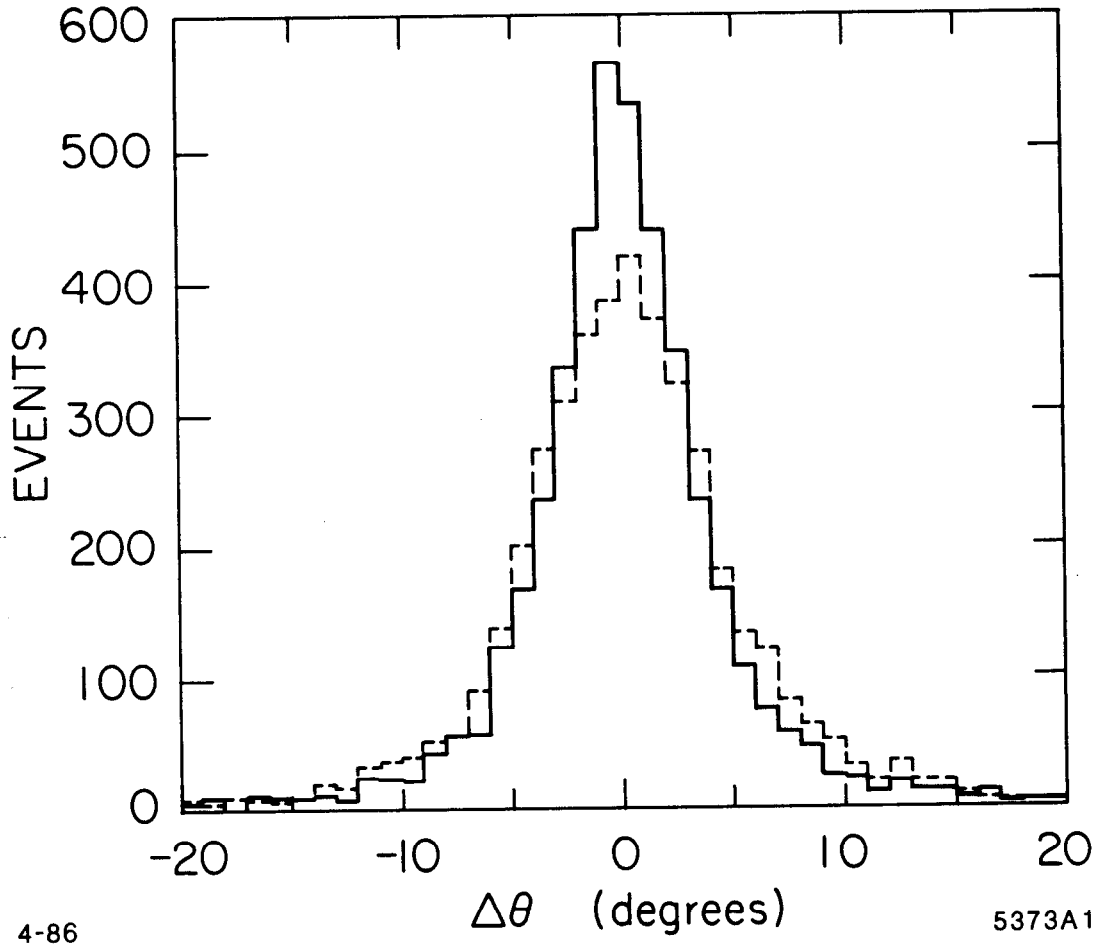
600
500
400
300
200
100
0
EVENTS
-20
-10
0
10
20
Δθ (degrees)
4-86
5373A1

Fig. 8

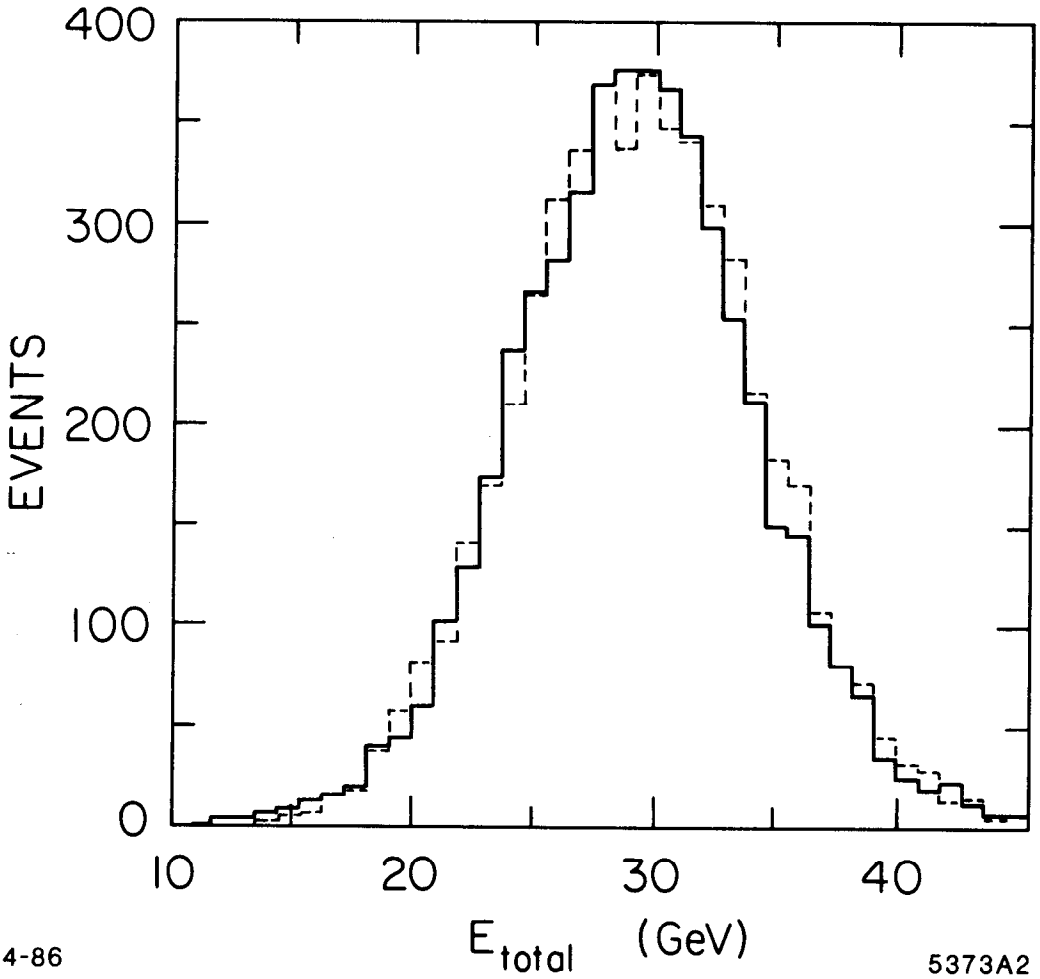

Fig. 9

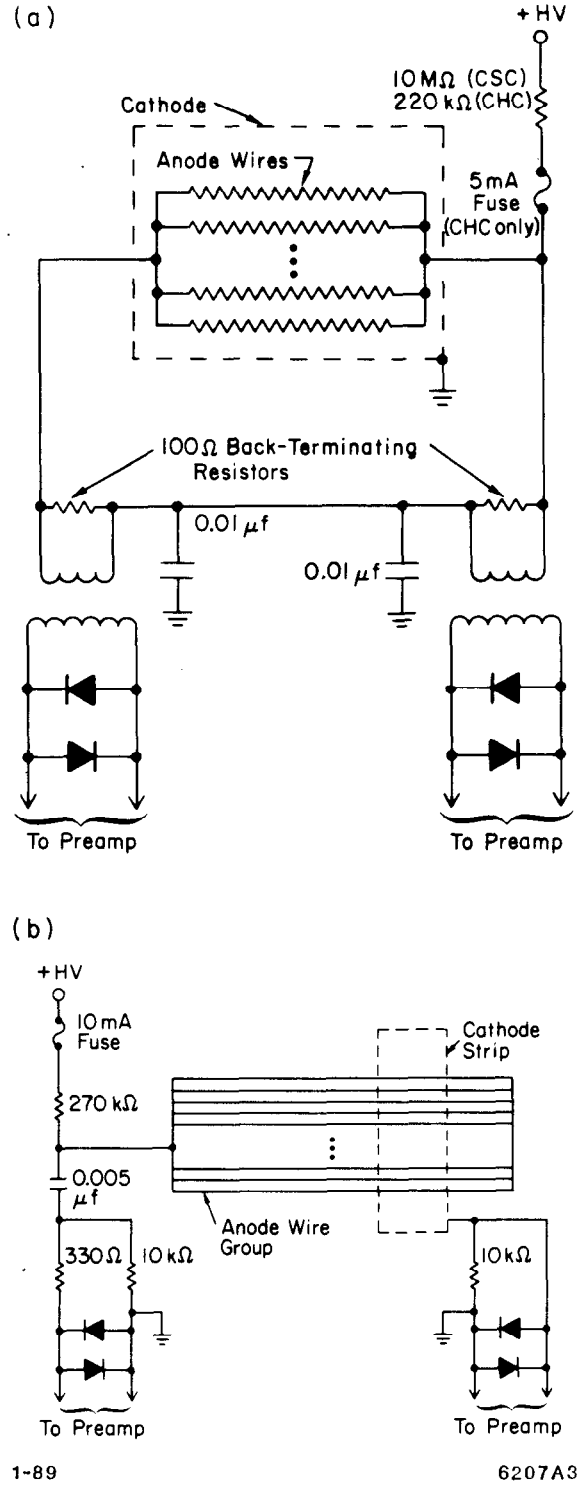
(a)
+HV
10MΩ (CSC)
220 kΩ (CHC)
Cathode
Anode Wires
5mA
Fuse
(CHC only)
100Ω Back-Terminating
Resistors
0.01 μf
0.01 μf
To Preamp
To Preamp
(b)
+HV
10mA
Fuse
270 kΩ
0.005
μf
330Ω
10kΩ
Cathode
Strip
Anode Wire
Group
10kΩ
To Preamp
To Preamp
1-89
6207A3

Fig. 10

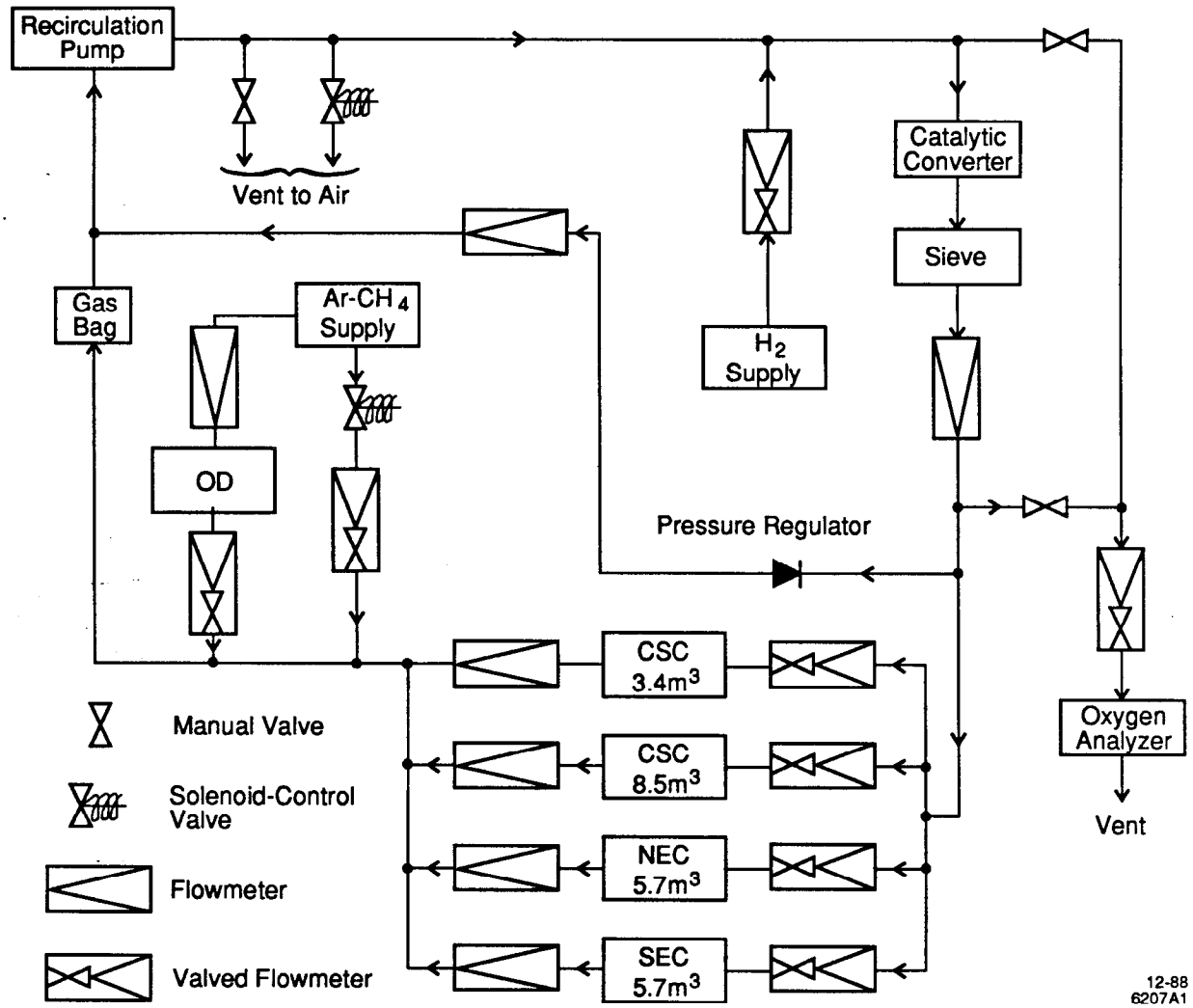
Recirculation Pump
Vent to Air
Catalytic Converter
Sieve
Gas Bag
Ar-CH 4 Supply
H2 Supply
OD
Pressure Regulator
CSC 3.4m3
CSC 8.5m3
NEC 5.7m3
SEC 5.7m3
Oxygen Analyzer
Vent
Manual Valve
Solenoid-Control Valve
Flowmeter
Valved Flowmeter
12-88
6207A1

Fig. 11

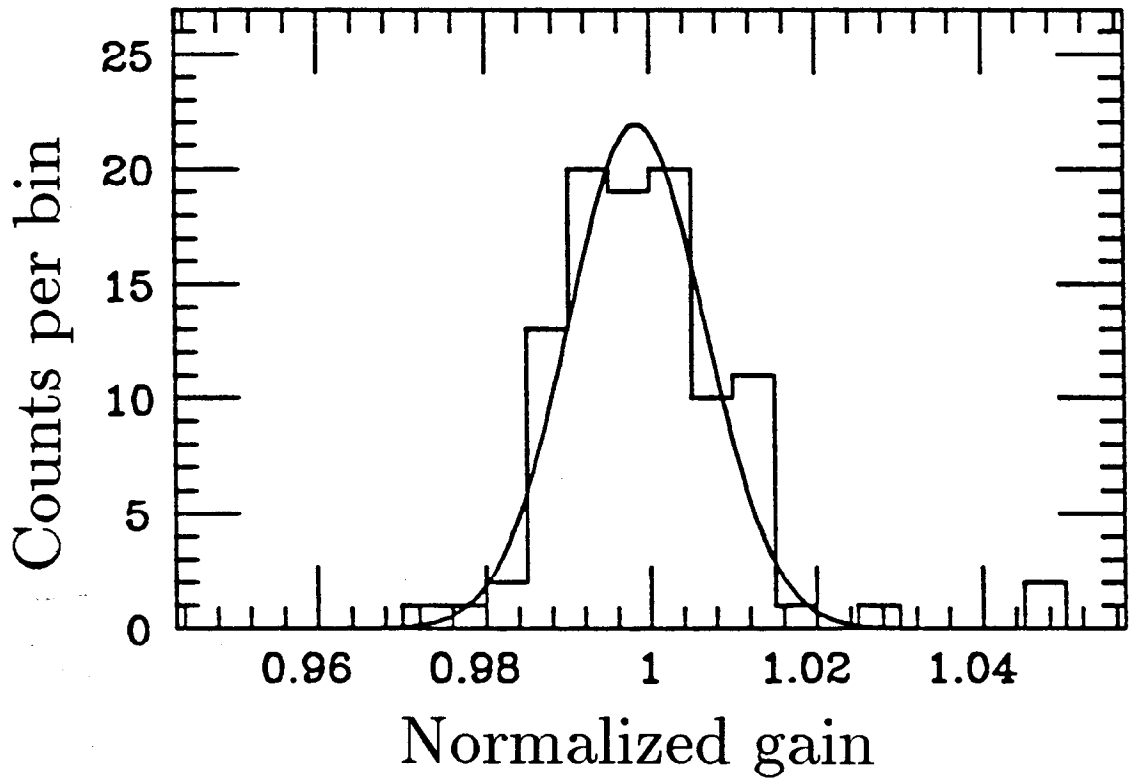

Fig. 12

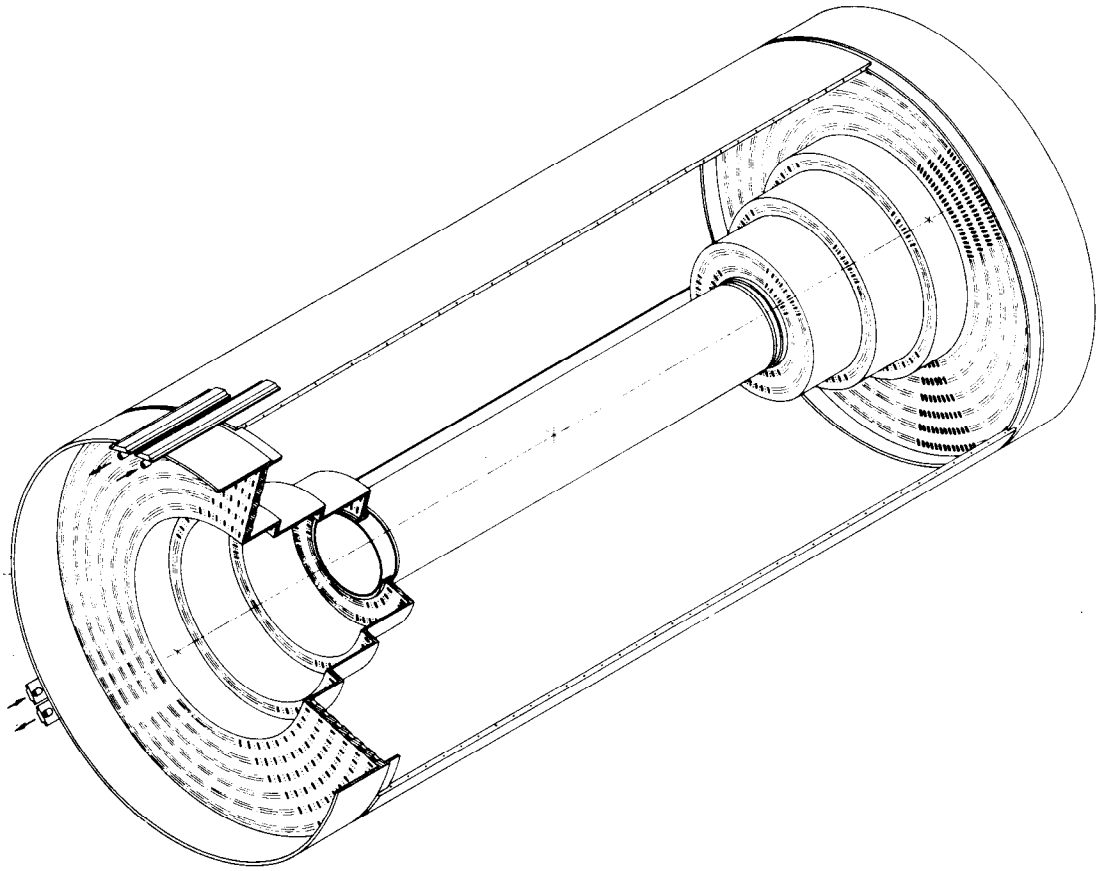

Fig. 13

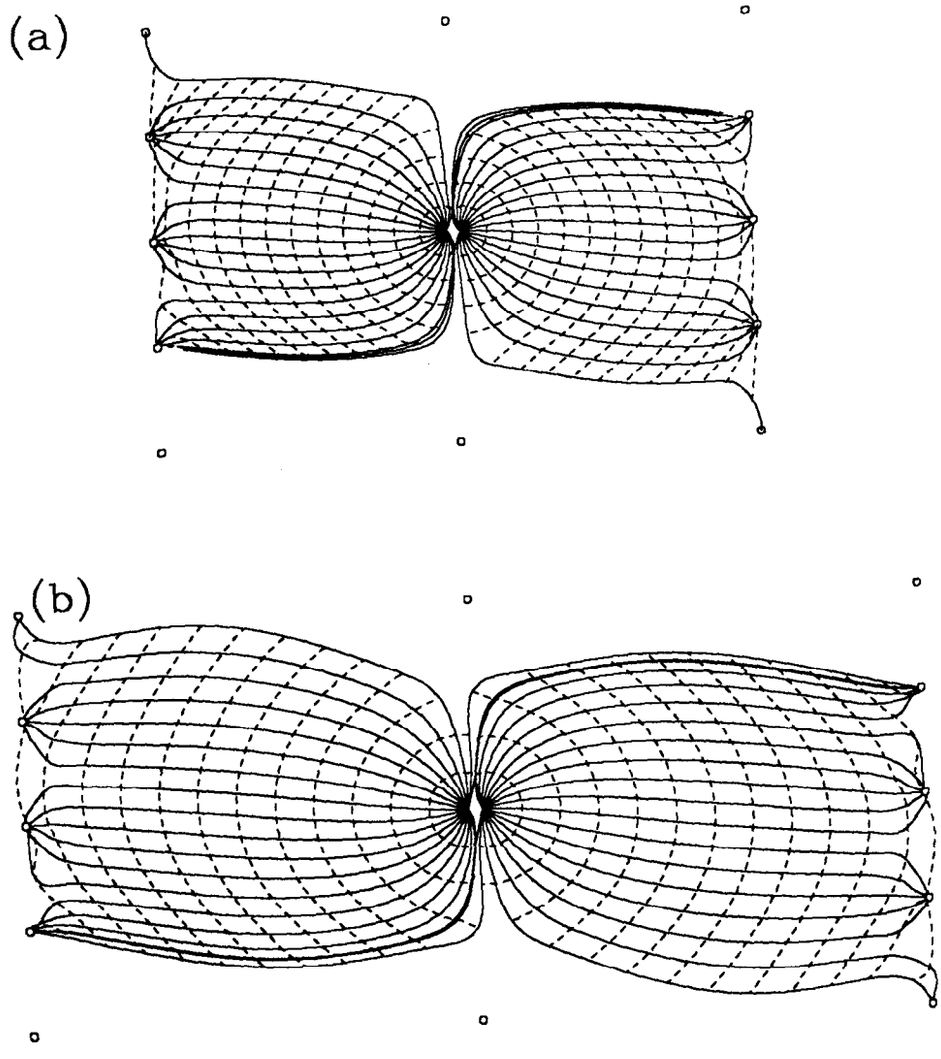

Fig. 14

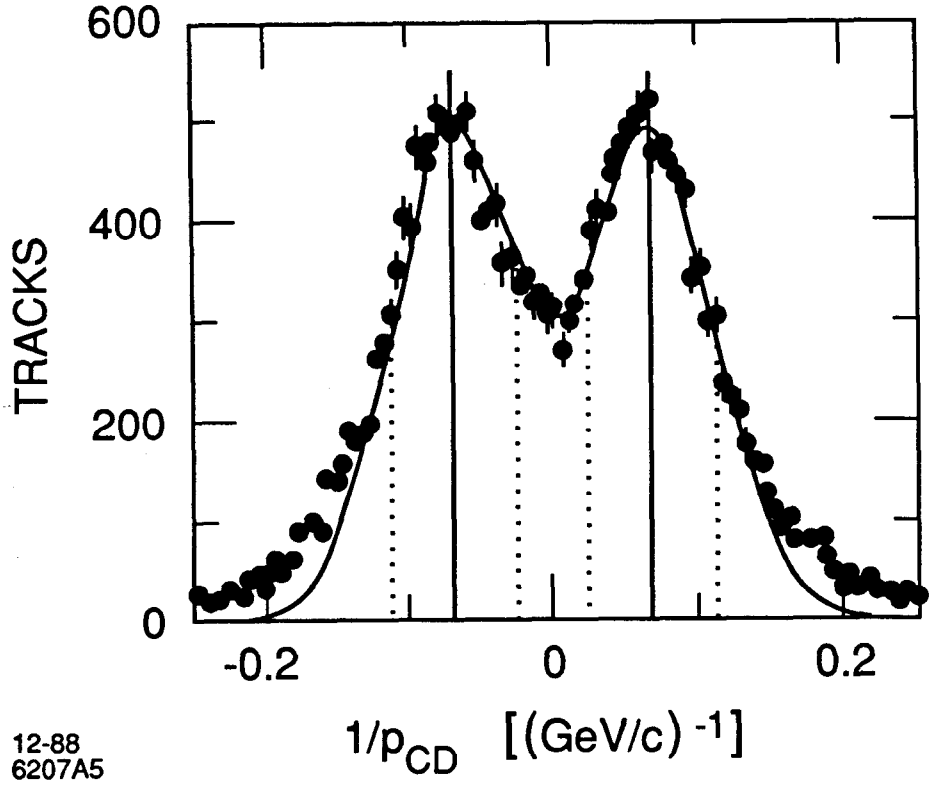

Fig. 15

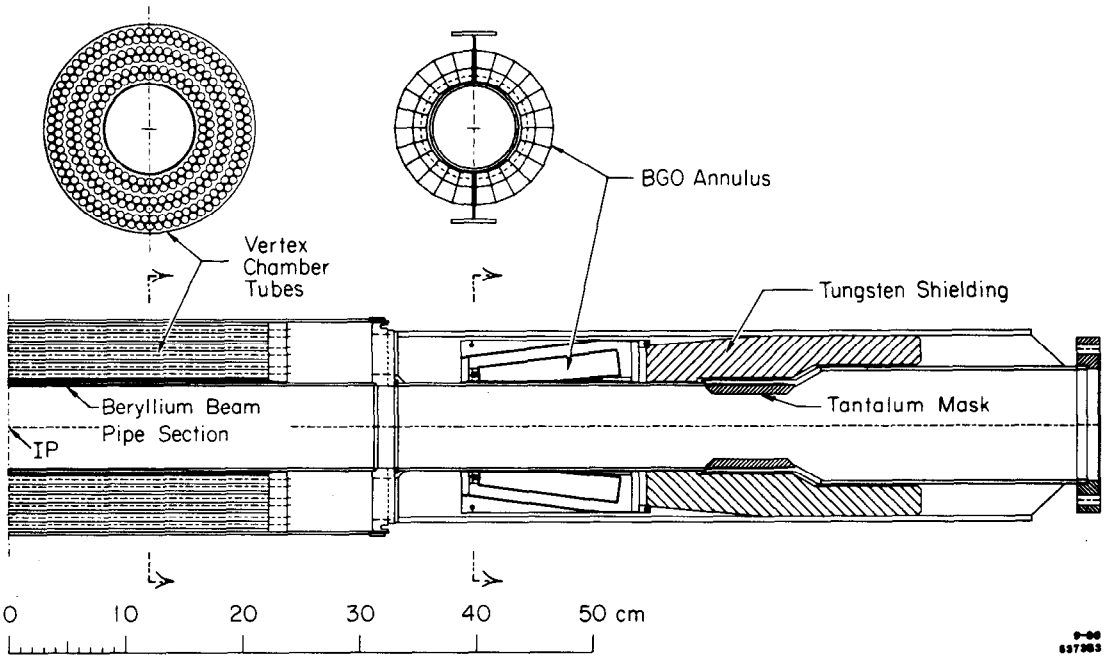
BGO Annulus
Vertex
Chamber
Tubes
Tungsten Shielding
Beryllium Beam
Pipe Section
IP
Tantalum Mask
0
10
20
30
40
50 cm

Fig. 16

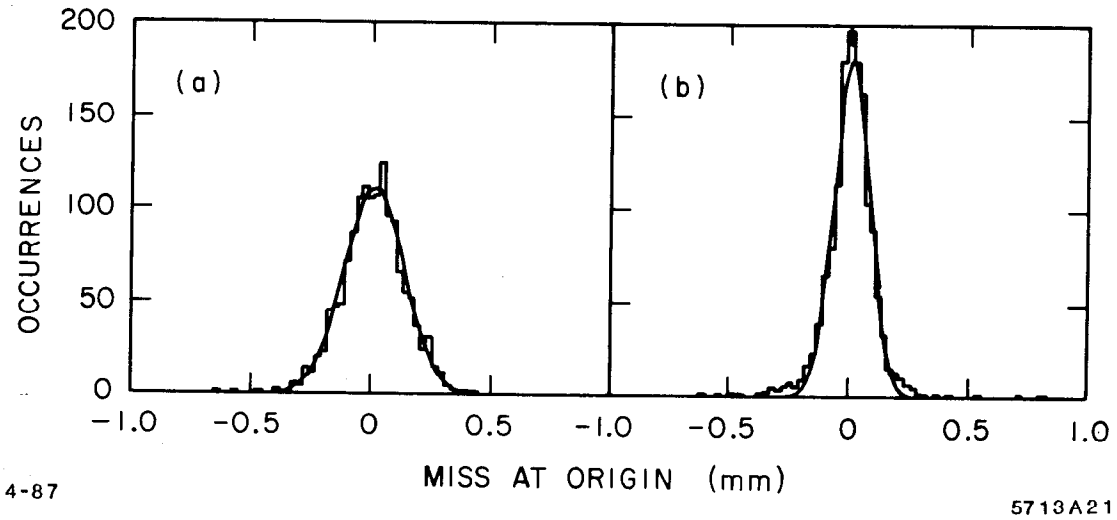
200
150
100
50
0
OCCURRENCES
(a)
(b)
−1.0
−0.5
0
0.5
−1.0
−0.5
0
0.5
1.0
MISS AT ORIGIN (mm)
4-87
5713A21

Fig. 17

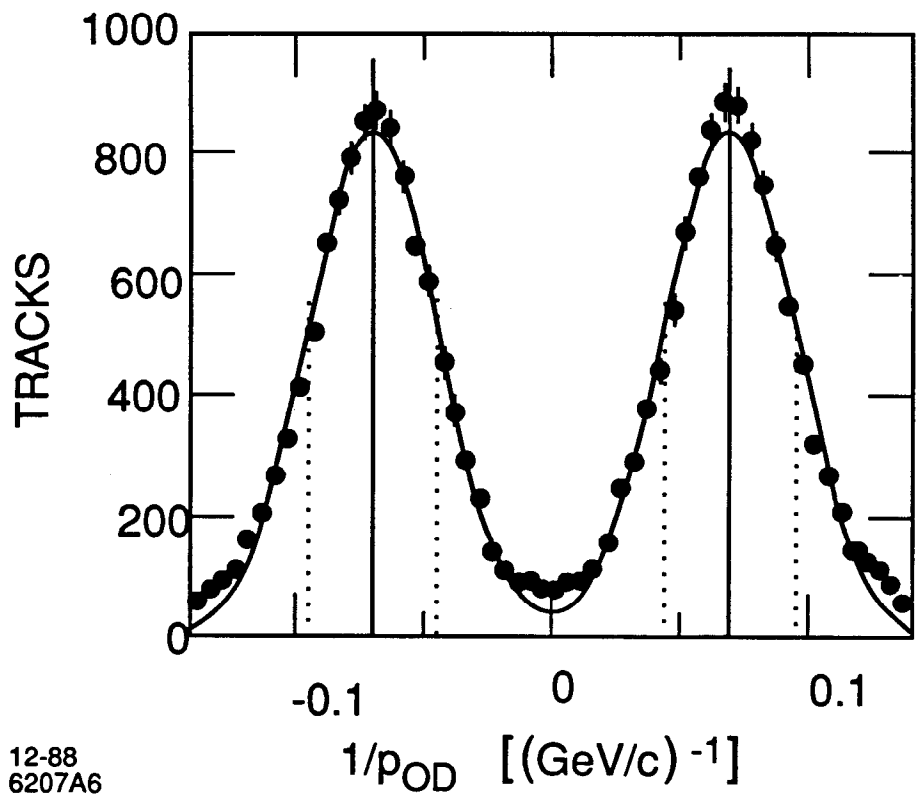

Fig. 18

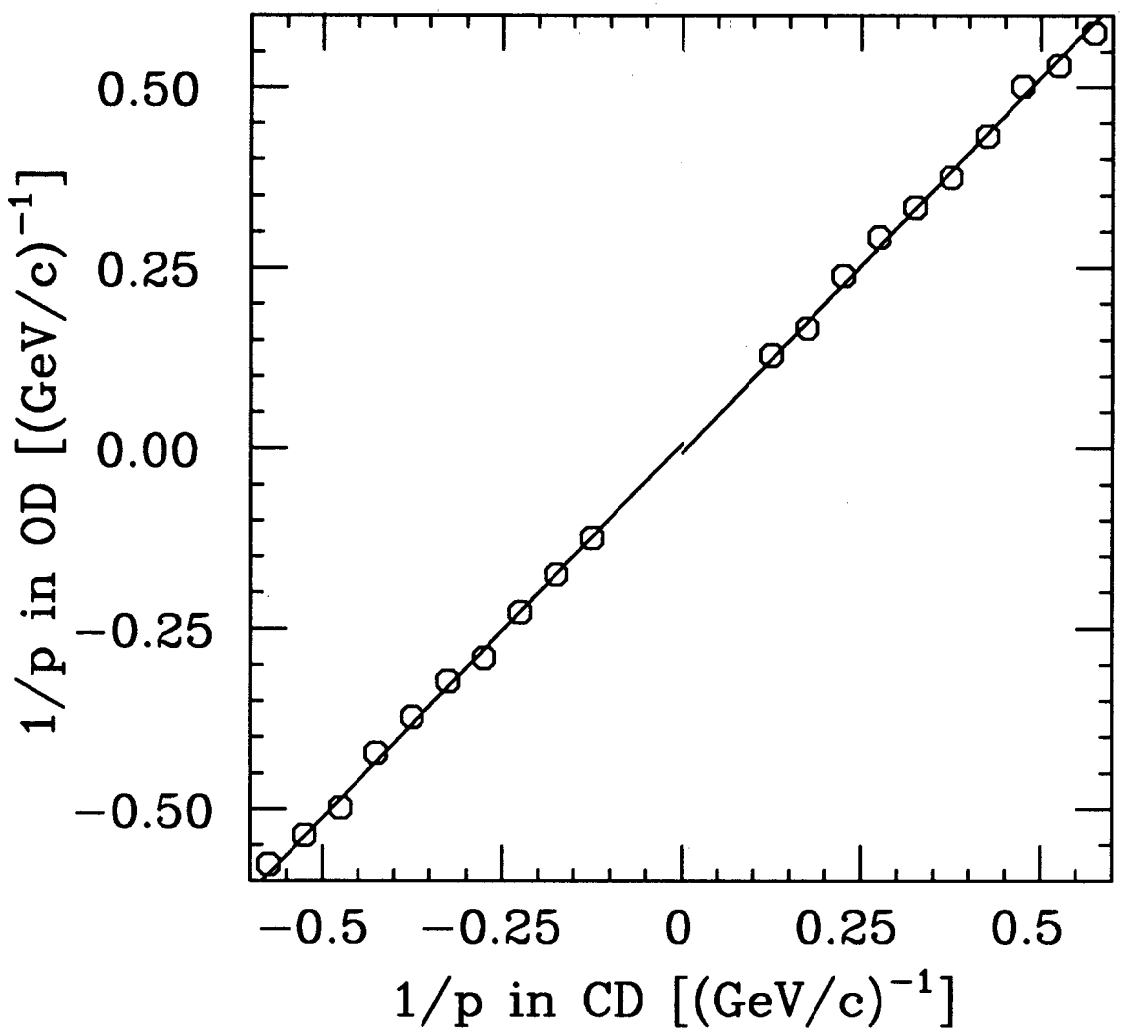

Fig. 19

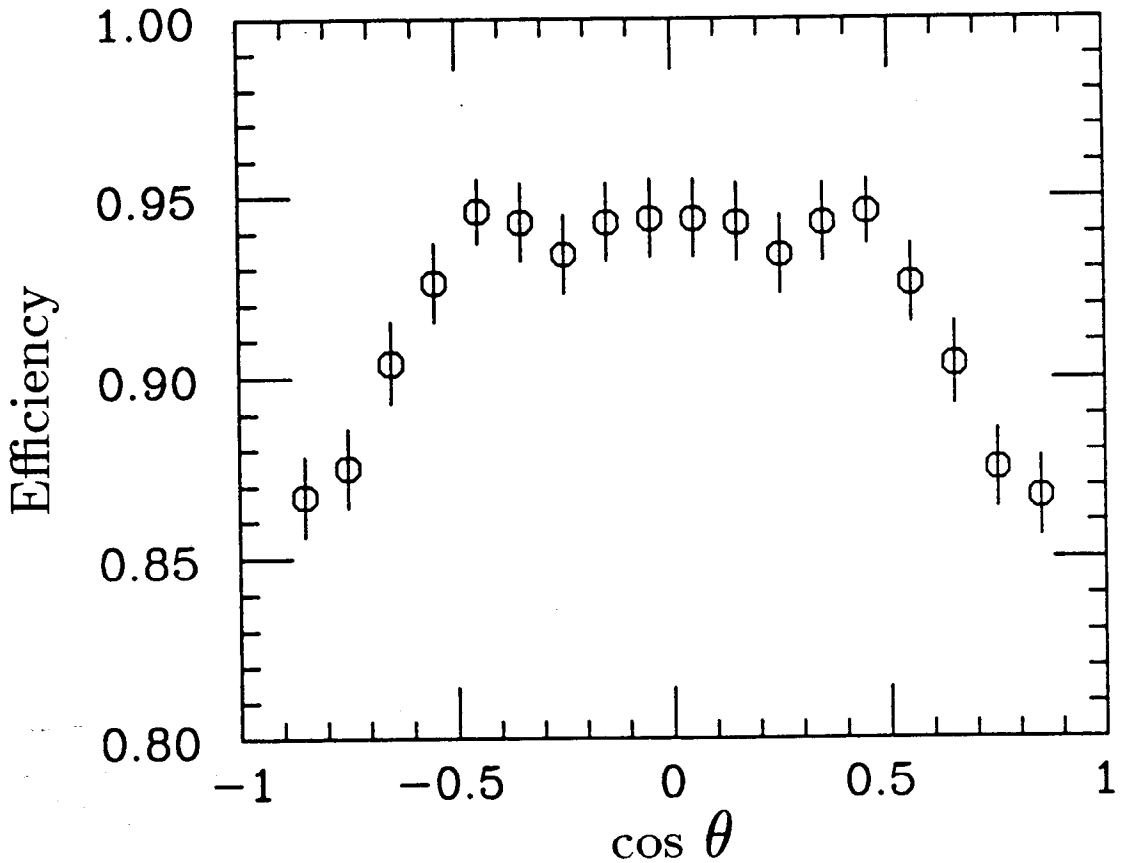

Fig. 20

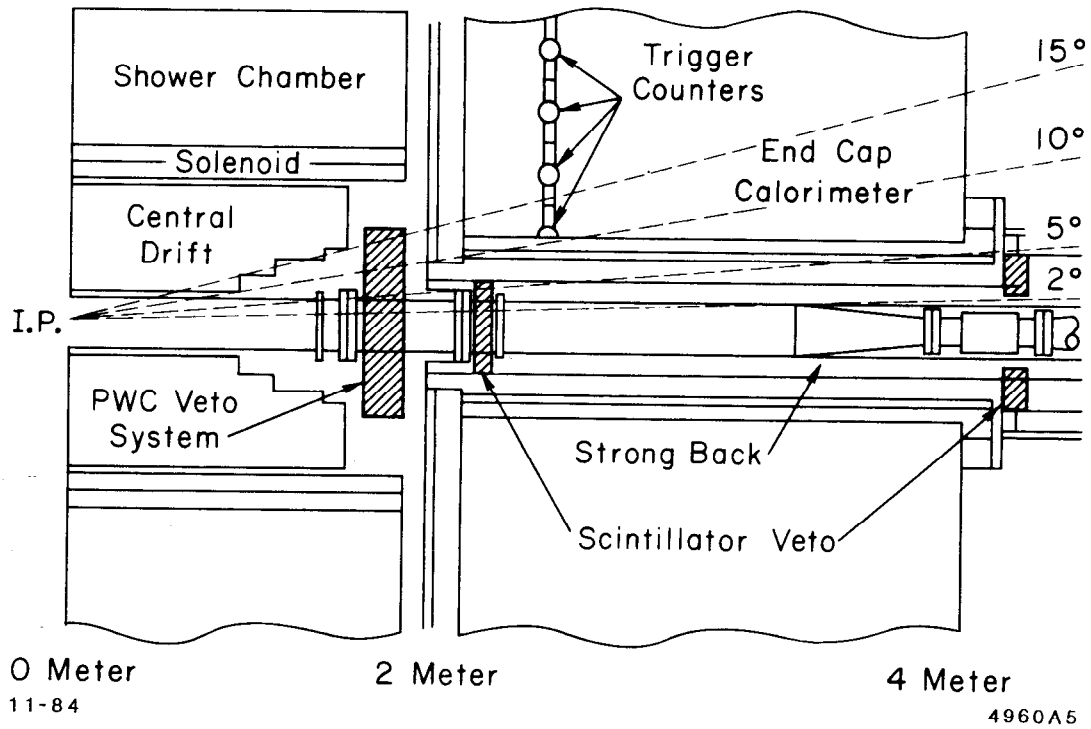
Shower Chamber
Solenoid
Central
Drift
I.P.
PWC Veto
System
Trigger
Counters
End Cap
Calorimeter
15°
10°
5°
2°
Strong Back
Scintillator Veto
0 Meter
2 Meter
4 Meter
11-84
4960A5

Fig. 21

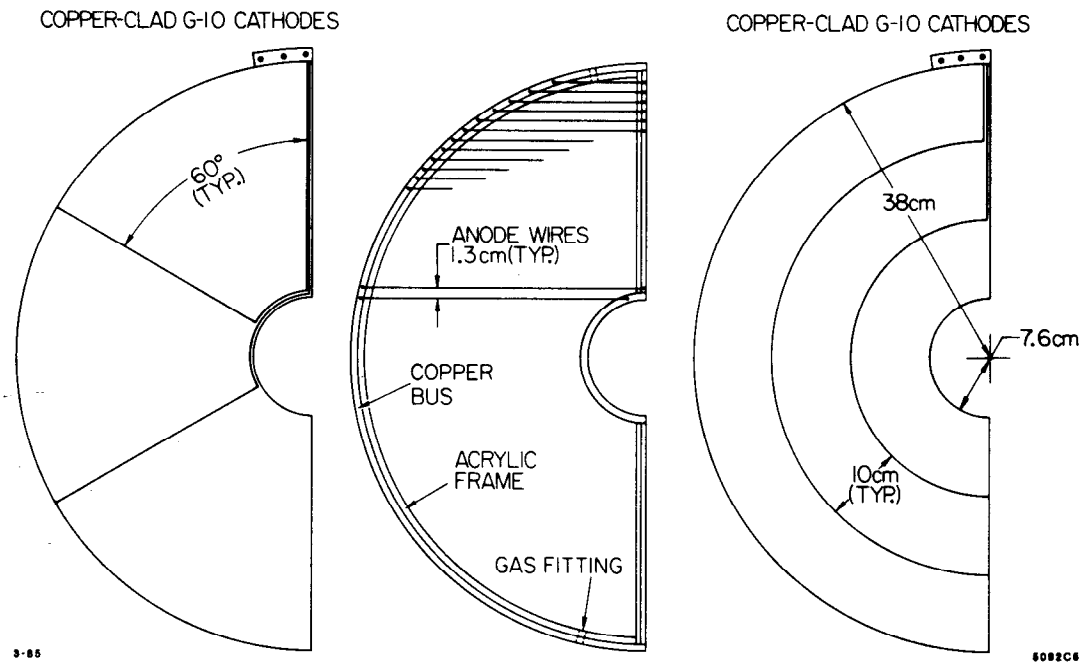
COPPER-CLAD G-10 CATHODES
60°
(TYP.)
ANODE WIRES
1.3cm(TYP.)
COPPER
BUS
ACRYLIC
FRAME
GAS FITTING
COPPER-CLAD G-10 CATHODES
38cm
7.6cm
10cm
(TYP.)
3-85
5092C6

Fig. 22

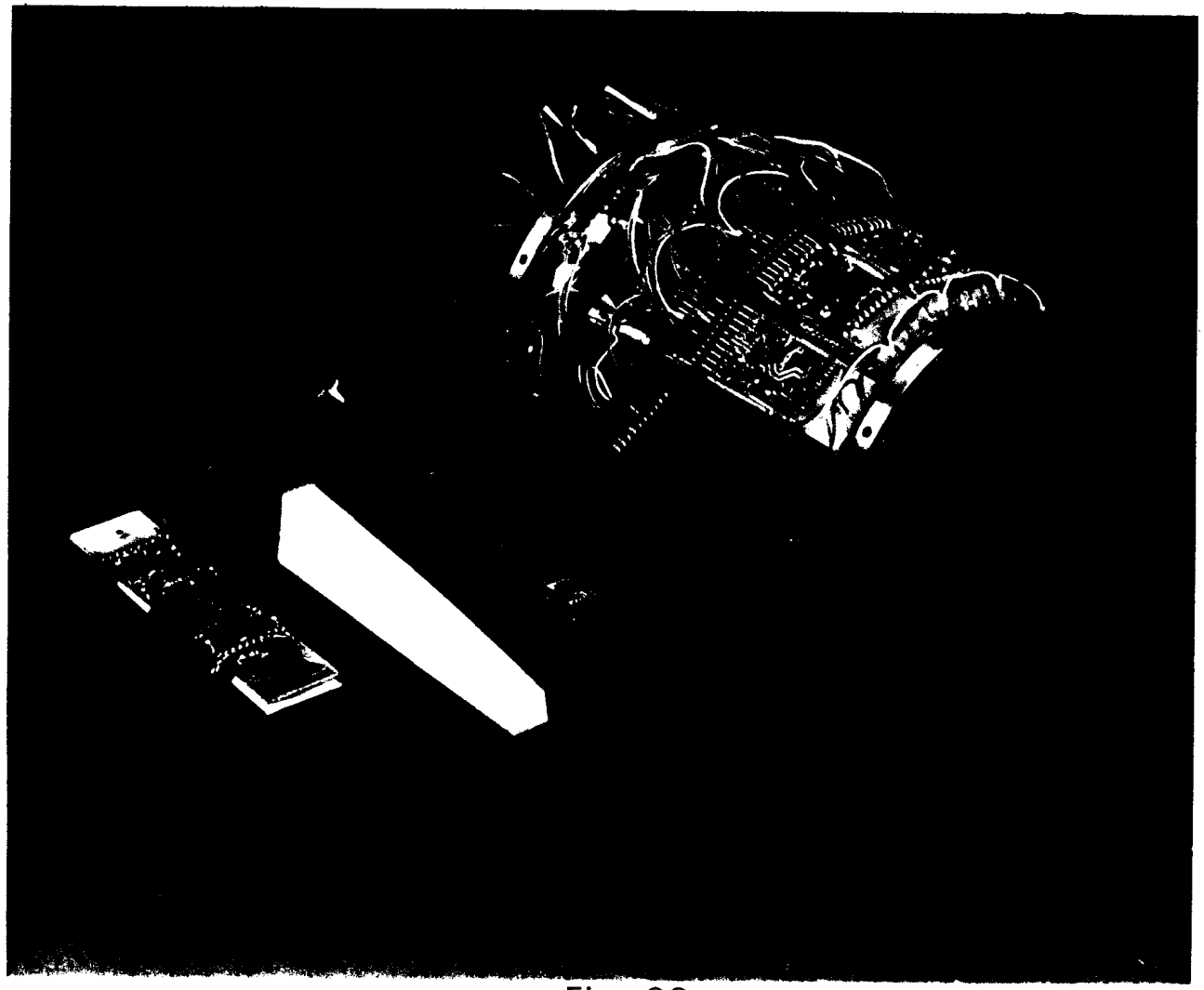

Fig. 23

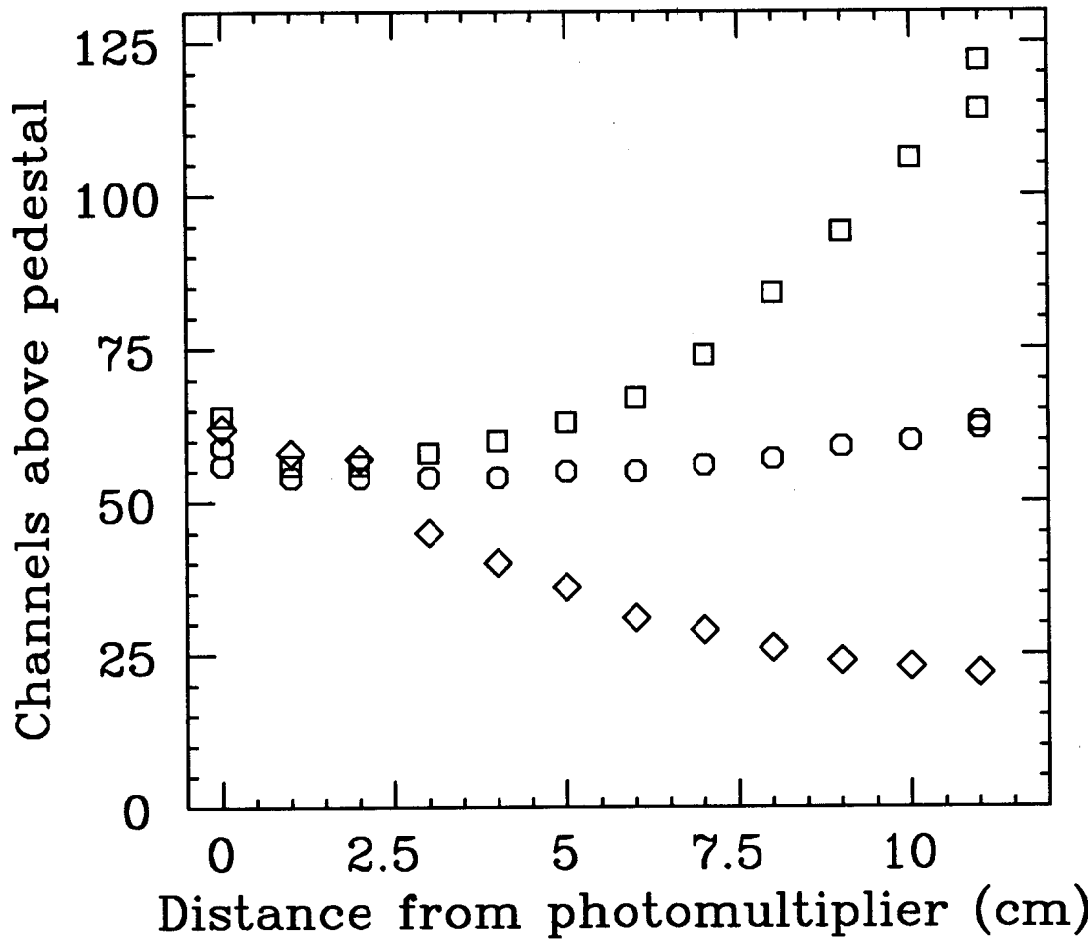
125
100
75
50
25
0
Channels above pedestal
0
2.5
5
7.5
10
Distance from photomultiplier (cm)

Fig. 24

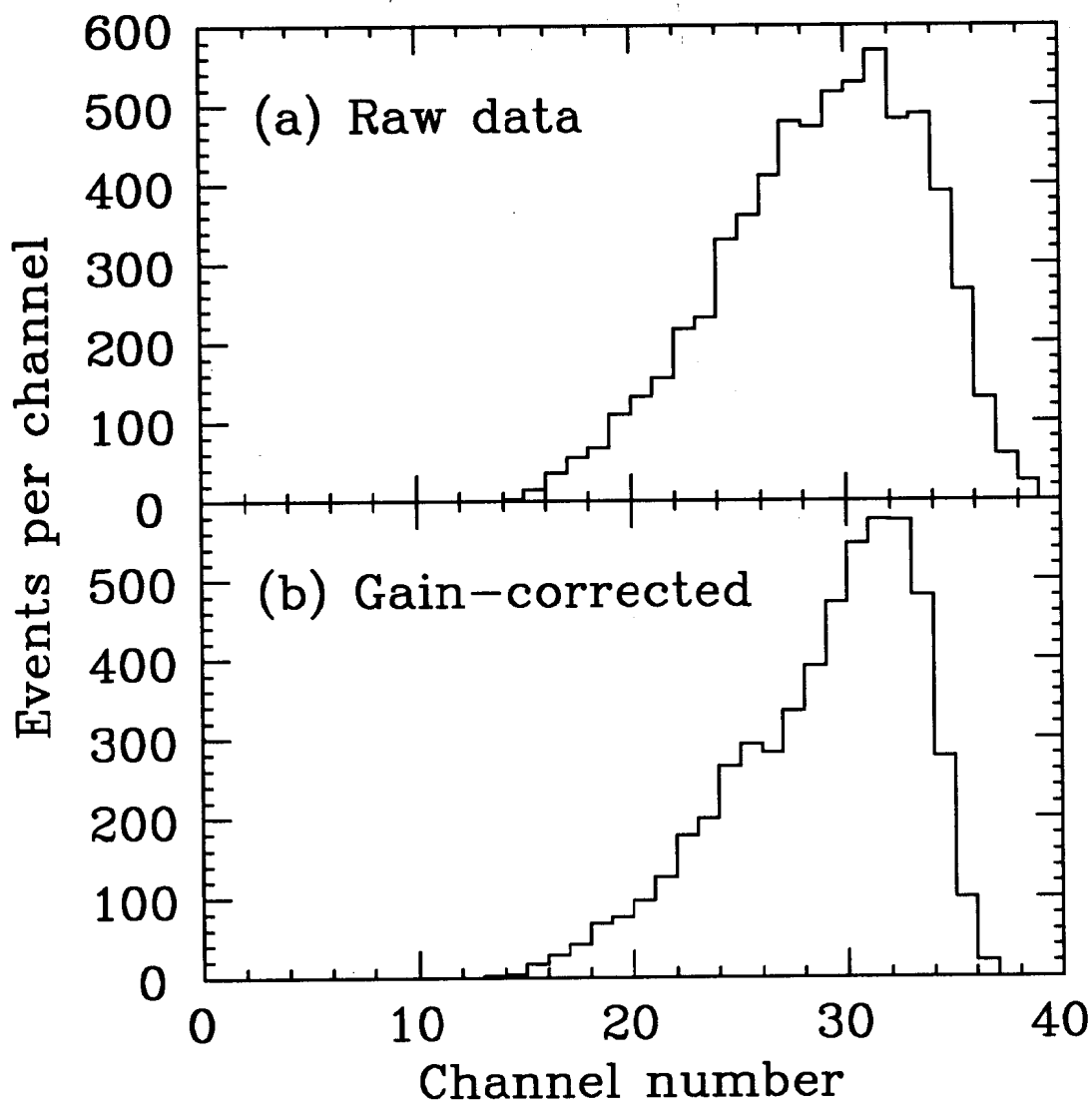
(a) Raw data
(b) Gain−corrected
Events per channel
Channel number
600
500
400
300
200
100
0
500
400
300
200
100
0
0
10
20
30
40

Fig. 25

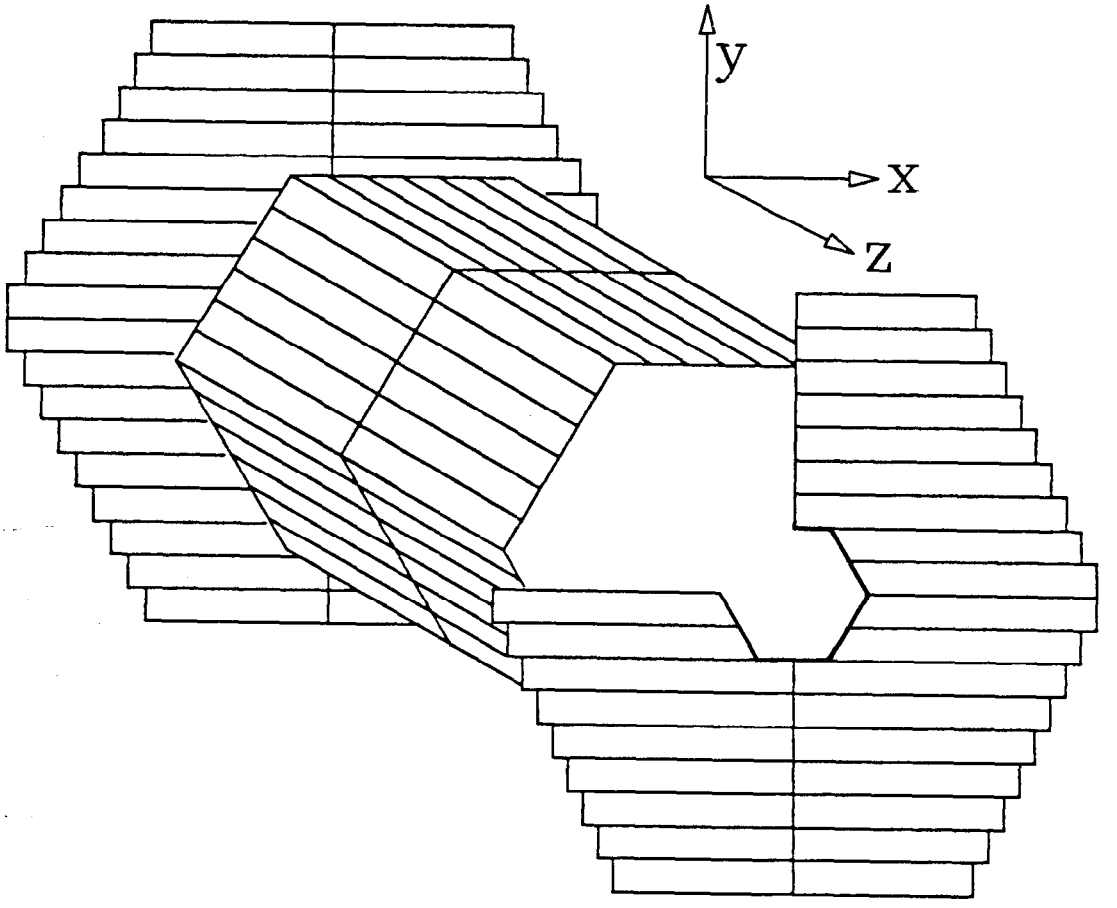

XBL 891-251

Fig. 26

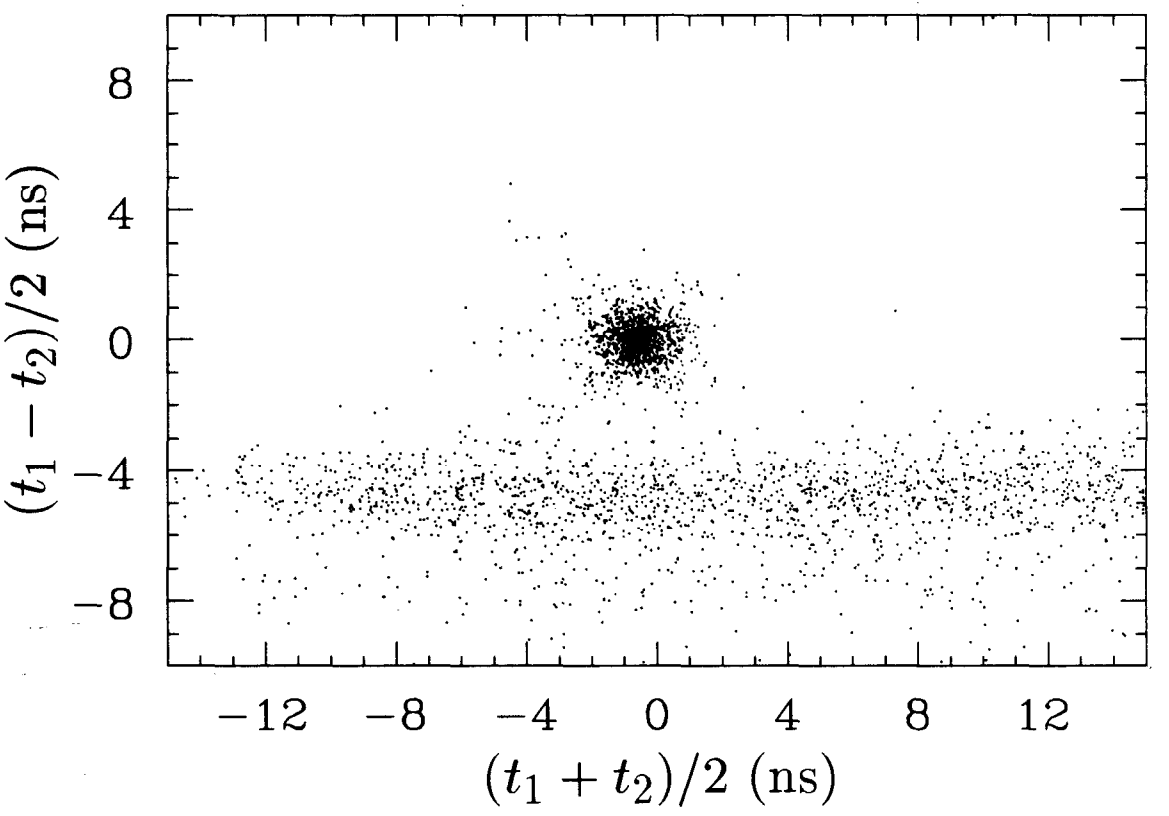

Fig. 27

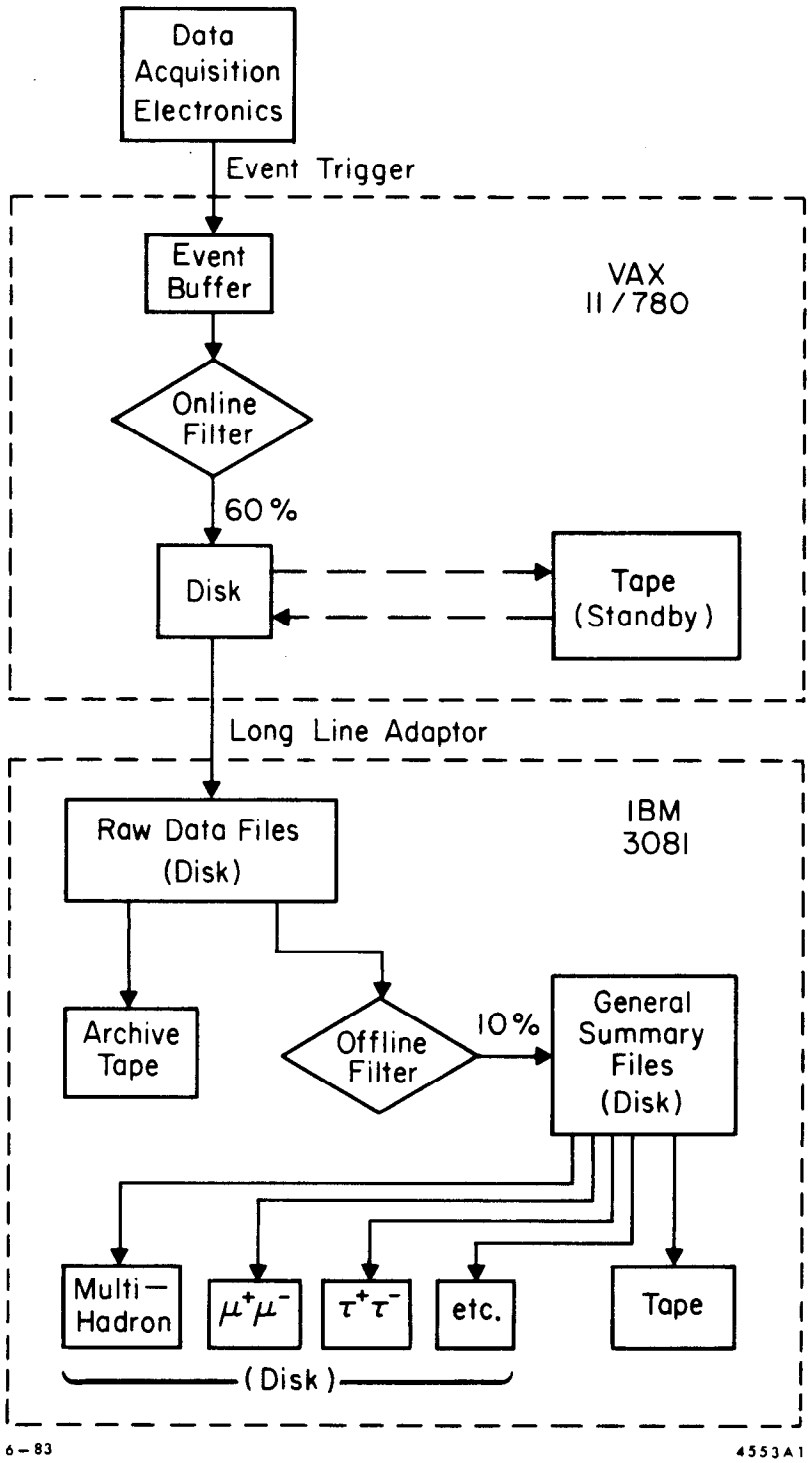
Data Acquisition Electronics
Event Trigger
Event Buffer
VAX 11/780
Online Filter
60 %
Disk
Tape (Standby)
Long Line Adaptor
Raw Data Files (Disk)
IBM 3081
Archive Tape
Offline Filter
10 %
General Summary Files (Disk)
Multi-Hadron
$\mu^+\mu^-$
$\tau^+\tau^-$
etc.
Tape
(Disk)
6-83
4553A1

Fig. 28